PL-TR-96-2016
Environmental Research Papers, No. 1186

WAVEGUIDE EFFECTS OF LARGE-SCALE STRUCTURAL VARIATION, ANELASTIC ATTENUATION, AND RANDOM HETEROGENEITY ON SV Lg PROPAGATION: A FINITE-DIFFERENCE MODELING STUDY

Rong-Song Jih

21 DECEMBER 1995

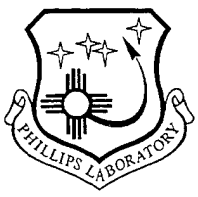

PHILLIPS LABORATORY
Directorate of Geophysics
AIR FORCE MATERIEL COMMAND
HANSCOM AFB, MA 01731-3010

DISCLAIMER NOTICE

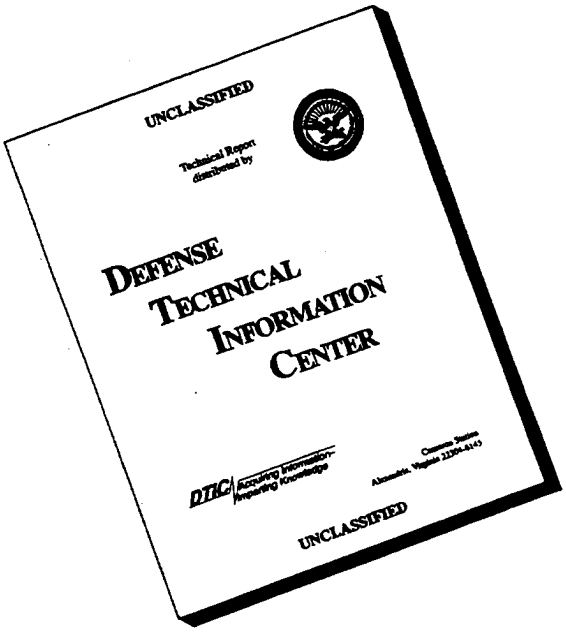

THIS DOCUMENT IS BEST QUALITY AVAILABLE. THE COPY FURNISHED TO DTIC CONTAINED A SIGNIFICANT NUMBER OF PAGES WHICH DO NOT REPRODUCE LEGIBLY.

"This technical report has been reviewed and is approved for publication."

JAMES F. LEWKOWICZ, Director
Earth Sciences Division

This report has been reviewed by the ESC Public Affairs Office (PA) and is releasable to the National Technical Information Service (NTIS).

Qualified requestors may obtain additional copies from the Defense Technical Information Center (DTIC). All others should apply to the National Technical Information Service (NTIS).

If your address has changed, or if you wish to be removed from the mailing list, or if the addressee is no longer employed by your organization, please notify PL/IM, 29 Randolph Road, Hanscom AFB, MA 01731-3010. This will assist us in maintaining current mailing list.

Do not return copies of this report unless contractual obligations or notices on a specific document requires that it be returned.

REPORT DOCUMENTATION PAGE

Form Approved
OMB No. 0704-0188

1. AGENCY USE ONLY (Leave blank)	2. REPORT DATE	3. REPORT TYPE AND DATES COVERED
	21 December 1995	Scientific, Interim, 25 Apr - 24 Oct 1995

4. TITLE AND SUBTITLE
Waveguide Effects of Large-Scale Structural Variation, Anelastic Attenuation, and Random Heterogeneity on SV Lg Propagation: A Finite-Difference Modeling Study

5. FUNDING NUMBERS

PE 35999F	PE 621010
PR TERM	PR 7600
TA GM	TA 09
WU 88	WU 08

6. AUTHOR(S)
Rong-Song Jih*

7. PERFORMING ORGANIZATION NAME(S) AND ADDRESS(ES)
Earth Science Division (GPE)
Phillips Laboratory
29 Randolph Road
Hanscom AFB, MA 01731-3010

8. PERFORMING ORGANIZATION REPORT NUMBER
PL-TR-96-2016
ERP, No. 1186

9. SPONSORING / MONITORING AGENCY NAME(S) AND ADDRESS(ES)
HQ AFTAC/TTR
1030 South Highway 1A1
Patrick AFB, FL 32925-6001

10. SPONSORING / MONITORING AGENCY REPORT NUMBER

11. SUPPLEMENTARY NOTES
* Supported under AFTAC Project Authorization T/0121

12a. DISTRIBUTION / AVAILABILITY STATEMENT
Approved for Public Release; Distribution Unlimited

12b. DISTRIBUTION CODE

13. ABSTRACT *(Maximum 200 words)*

L_g is often the most prominent phase on regional seismograms and hence it has been extensively used in various seismic operations: (a) detection and location, (b) source size (earthquake magnitude and explosive yield) estimation, and (c) source type identification (that is, discrimination). However, there have also been many outstanding fundamental questions regarding the excitation and propagation of the L_g phase. This report documents a comprehensive modeling study aimed at quantification of the individual effect of several major factors that affect L_g propagation. Two techniques are specifically designed for this project: [1] a pure L_g wave packet suitable for triggering the linear finite-difference [LFD] calculations, and [2] a simple, causal method to incorporate spatially-varying anelastic attenuation into LFD simulations. A variety of mechanisms responsible for L_g blockage / weakening are carefully evaluated. These mechanisms include [a] large-scale structural variations and discontinuities, [b] anelastic attenuation, and [c] small-scale random heterogeneities. A L_g path-correction procedure is proposed to correct for these effects as well as the geometrical spreading. This procedure has an immediate (that is, operational) application to routine processing of seismic records and it could improve the performance of seismic discriminants based on P/L_g ratios.

14. SUBJECT TERMS
Lg, Seismic wave propagation, Linear finite-difference method, Blockage, Anelastic attenuation, Q, Random heterogeneity, Path calibration

15. NUMBER OF PAGES
116

16. PRICE CODE

17. SECURITY CLASSIFICATION OF REPORT	18. SECURITY CLASSIFICATION OF THIS PAGE	19. SECURITY CLASSIFICATION OF ABSTRACT	20. LIMITATION OF ABSTRACT
Unclassified	Unclassified	Unclassified	SAR

CONTENTS

ILLUSTRATIONS

TABLES

ACKNOWLEDGEMENTS

This project benefited from discussion with Bob Blandford (AFTAC), Dave Harkrider (BC), Anton Dainty (PL), Dave Russell (AFTAC), Keith McLaughlin (S-Cubed), and Howard Patton (LLNL). The L_g eigenfunctions needed to synthesize the pure L_g wave packet are generated with Bob Herrmann's (1987) software. The PSLIB *PostScript* library released by Paul Wessel (HIG) and Walter Smith (Scripps) has been used in generating most of the figures. This study was supported by Air Force Technical Applications Center. The views and conclusions contained in this report are those of the author and should not be interpreted as representing the official polices, either expressed or implied, of the U.S. Air Force or the U.S. Government.

SUMMARY

Many empirical studies have found evidence that abrupt thinning of the crust can weaken the L_g phase, and that contained sedimentary basins or mountain ranges on the path can completely or partially block the phase. Theoretical (modeling) studies can provide insights for better understanding and interpretations of the physical mechanisms involved (Blandford *et al.*, 1992). This study attempts to quantitatively predict the waveguide effects using extensive two-dimensional linear elastic (P–SV) finite-difference [LFD] calculations. Miscellaneous waveguide effects are analyzed and compared, both qualitatively and quantitatively, through visualization and spectral analysis. A pure L_g wave packet is injected into a stratified portion of the grid as the reference initial condition to trigger all LFD calculations for a suite of heterogeneous crustal structures. An obvious advantage of this approach is that the effects due to different types of heterogeneity on L_g phase can be isolated and evaluated easily. Each model contains a laterally heterogeneous crust superimposed on the homogeneous mantle. The heterogeneities examined include large-scale lateral structural variations in the crustal waveguide (such as Moho uplift, crustal thickening, rugged free-surface topography, embedded thick sedimentary layers, *etc.*), anelasticity, and small-scale random heterogeneity.

The LFD results demonstrate that indeed both abrupt changes in the Moho topography and a thick contained sedimentary layer can cause L_g blockage primarily through strong L_g-to-S_n conversions (with actually different physical mechanisms). Alluvial basin structures cause strong reverberations as well as very strong L_g-to-R_g conversions. If the principle of seismic reciprocity is invoked, R_g-to-L_g conversion could be an important mechanism of L_g excitation for certain structures. Unlike the case of R_g waves, a moderate free-surface topography alone does not seem to affect L_g propagation as much as do other types of heterogeneity. Anelasticity and small-scale random heterogeneity can also explain the L_g blockage. An RMS velocity variation of 8 percent in the whole crust is equivalent to a $Q_0(L_g)$ of about 270, which would be sufficient to reduce the peak amplitude of 1Hz L_g waves by 30 percent for every 100 km it traverses. However, LFD calculations also indicate that these mechanisms exhibit some systematic differences in the couplings of L_g into other phases. Thus, identifying the actual mechanism responsible for the blockage along a specific path is possible.

Received for publication 21 December 1995.

WAVEGUIDE EFFECTS OF LARGE-SCALE STRUCTURAL VARIATION, ANELASTIC ATTENUATION, AND RANDOM HETEROGENEITY ON SV Lg PROPAGATION: A FINITE-DIFFERENCE MODELING STUDY

1. INTRODUCTION

The most prominent regional phase generated by shallow events is the L_g phase identified by Press and Ewing (1952). The L_g phase receives considerable attention in recent years because of its potential use in yield estimation (*e.g.*, Nuttli, 1986) and discriminating between earthquakes and explosions at regional distances (*e.g.*, Blandford, 1981; Pomeroy *et al.*, 1982). Based on empirical observations, RMS L_g has been recognized as a stable relative-yield indicator (Patton, 1988; Hansen *et al.*, 1990). However, it is also recognized that L_g, like R_g, is sensitive to changes in structure along its path, which can have deleterious effects on any role as a discriminant (see Lynnes and Baumstark, 1991) or magnitude measure (see Jih and Lynnes, 1993), unless the propagation effects are accurately accounted for. Numerous studies have used the sensitivity of L_g to structural effects to map regions of anomalous propagation and to try to associate them with crustal structure. Bias in L_g-based magnitude measurements were reported by Gregersen (1984) in Greenland. Very low L_g/S_n amplitude ratios have been observed after crossing the Tibetan plateau (Ruzaikin *et al.*, 1977), the North Sea grabens (Gregersen, 1984; Kennett *et al.*, 1985), the Caspian Sea, or the Black Sea (Levshin and Berteussen, 1979; Kadinsky-Cade *et al.*, 1981). Chinn *et al.* (1980) (and Lynnes and Baumstark, 1991) observed that the efficiency of the L_g propagation is better for paths parallel to the structural trend than for paths in the perpendicular direction. Earlier studies (Press and Ewing, 1952; Oliver and Ewing, 1957; Savarensky and Valdner, 1960) have established that L_g does not propagate through crust overlain by water deeper than 2 km. On the other hand, propagation across a marginal sea of continental shelf does not completely quench L_g, but can reduce its amplitude. Baumgardt (1991) compared the crustal cross-sections for L_g propagation, and he found that the L_g blockage correlates with thick sediment very well. Basically, his observation is that paths that do not cross basins or for which sediments do not vary by greater than 3 km exhibit little or no L_g blockage and scattering. Baumgardt (1991) also identified paths for which the surface elevations and crustal thickness change substantially, and yet L_g propagates efficiently. Thus his observations suggest that the near-surface sediment-thickness variations seem to correlate more strongly with L_g blockage than do the crustal-thickness variations. Zhang and Lay (1994) used surface topography as a manifestation of the varying crustal structures. They found a strong correlation between S_n/L_g ratios for Eurasian explosions and roughness or mean altitude of the topography along the path, based on a meager data set.

Despite the long-time interest, there remain many fundamental questions about the excitation and propagation of L_g waves phases to be answered. Numerical modeling of the L_g waves (and other regional phases) would complement the empirical studies by providing more accurate interpretations and better insight of the underlying physics. Theoretical studies of L_g propagation across continental margins have been conducted by Kennett (1986a), Maupin (1989), Regan and Harkrider (1989), Cao and Muirhead (1993), and Gibson and Campillo (1994), using different techniques. A simple geometrical ray theory can be used to predict the kinematic property in a qualitative manner, as Kennett (1986a) has illustrated, but would fail to explain the dynamic properties for complex media. Kennett (1986b, 1989ab) used a modal summation to investigate L_g propagation in stratified and weakly heterogeneous media. Mitchell and Hwang (1987) computed multi-mode synthetics for 1-D models with various thickness of low-Q sediments. Regan and Harkrider (1989) used a hybrid of propagator matrix and the finite-element [FE] methods to model the *SH*-L_g -wave propagation. Cao and Muirhead (1993) applied a 2-dimensional P-SV finite-difference method to explore L_g blockage and argue that a water column over the crust is an important factor in blocking L_g propagation. Gibson and Campillo (1994) applied both the dynamic ray tracing and the boundary-integral equation methods to model L_g blockage in the west Pyrenees Range, near the French-Spanish border. They suggest that the unmodeled scattering by small-scale features within the lower crust is the reason for the observed blockage.

In this study the two-dimensional linear elastic (*P–SV*) finite-difference [LFD] method is utilized to model the propagation and scattering of L_g waves in a suite of crustal models. Each model contains a laterally heterogeneous crust superimposed on the homogeneous mantle. The heterogeneities examined include anelasticity, random velocity variation, rugged interfaces, rugged free-surface topography, as well as embedded thick sedimentary layers. The pure L_g wave packet is injected into a stratified portion of the LFD grid as the reference initial condition to trigger all LFD calculations. An obvious advantage of this approach is that the effect due to different types of heterogeneity on the L_g phase can be easily isolated and evaluated. A number of different output formats are available from the LFD simulation. In fact, one of the advantages of the LFD method (and the finite-element method) is the ability to save particle displacements for any number of receivers in the grid and for all times. A particularly informative way to view wave propagation through the models is by using numerical Schlieren digrams, or "snapshots". Wavefield snapshots are extensively used as a visualization aid throughout the study.

The procedure of implementing a pure L_g wave packet is described in Section 2 and validated with a reference crustal model. LFD experiments are then conducted with a suite of canonical models representing a variety of crustal structures. The geometrical effects of various structures on L_g propagation are analyzed, both qualitatively and quantitatively. In Sections 4 and 5, similar analyses are conducted for anelastic and random models, respectively. All three major categories of structures are compared and equated, regarding their roles in causing L_g blockage and the coupling of L_g into other

phases. A brief review on the reported observations of L_g blockage is given in Section 6. Finally, a quantitative way of describing L_g blockage is explored, and an improved amplitude/magnitude correcting procedure is presented, which includes a correction to account for the geometrical blockage.

2. LFD IMPLEMENTATION OF L_g WAVE PACKET

The LFD method has the advantage that the solution contains all conversions and all orders of multiple scattering. It permits examinations of fairly general models with arbitrary complex variations in material properties and free-surface geometry. Furthermore, it does not require many assumptions commonly invoked in other theoretical approaches. The basic limitations to the LFD method are the computational cost and memory requirements. These constrain the size of the grid and the number of time steps that can be calculated in a reasonable time frame. Several non-standard features have been incorporated into the LFD code used in this study:

[1] Explicit boundary conditions for the polygonal free-surface topography.

[2] The marching-grid technique for stretching the propagation distance in the lateral direction.

[3] A pure L_g wave packet suitable for LFD simulations.

[4] A simple way to incorporate a causal, spatially-varying attenuation operator into LFD simulations.

Detailed descriptions of the explicit boundary conditions and the marching grid technique can be found in Jih *et al.* (1988) and Jih (1993a). Incorporation of the causal, spatially-varying attenuation operator will be described in Section 4 of this report. The algorithm generating the incident L_g wave packet is analogous to the one Boore (1970) developed for the fundamental-mode Love wave packet. Given a stratified crustal model, the Thomson-Haskell method is used to compute the L_g dispersion and eigenfunctions associated with this structure. The L_g eigenfunctions are modulated by a Ricker (1977) wavelet in the wavenumber domain and then converted to the displacement field by the inverse Fourier transform. The resulting wavefield is well localized in both spatial and wavenumber domains, and can be easily embedded in complicated 2-dimensional models (for which other forward-modeling methods may fail) as the initial condition to trigger the LFD simulation. Ever since Boore (1970) outlined the original algorithm in his SH LFD calculations, the same procedure has been adopted frequently in elastic (P-SV) LFD simulations of R_g propagation/scattering problems. Just a few studies along this line include: Munasinghe and Farnell (1973), Martel *et al.* (1977), Fuyuki and Matsumoto (1980), Fuyuki and Nakano (1984), Levander (1985), Toksoz et al. (1986), McLaughlin and Jih (1986, 1987), and Jih (1993b, 1995). The study described herein is an extension to L_g of the R_g analysis as presented in McLaughlin and Jih (1986, 1987) and Jih (1993b, 1995). In an earlier study, Jih and McLaughlin (1988) applied the principle of reciprocity to model the excitation of L_g in various source media. The goal of this study is to investigate various path effects on L_g, not the excitation.

On real seismograms, the L_g phase often lacks a clear onset, but it does have a well-defined amplitude maximum with a group velocity around 3.5 km/sec. The L_g waves are basically the interference of multiply reflected S waves bouncing back and forth between the free surface and the Moho. We can envision that a system of planar S waves is set off at the Moho at equal delay with the same post-critical inclination, while another system of planar S waves is set off at the free surface in a symmetric manner, which corresponds to the bundle of reflected waves. If these two systems of waves (or rays) are properly confined in the same stratified region of the crust, they will establish repetitive reflections (at both the free surface and the Moho) with constructive interferences. By adjusting the time delay between the consecutive S wavefronts, we can obtain a denser (or coarser) interference pattern. The L_g waves can also be described as the superposition of many higher-mode surface waves which interfere to give the complex observed waveforms. For typical continental paths, the important contributions come from the stationary portions of the group velocity curves for about the first 10 modes up to 1 Hz (Knopoff *et al.*, 1973). These modes correspond to waves trapped in the crustal wave guide.

The L_g wave packet generated by the procedure described earlier exhibits all these expected features. Figure 1 gives the vertical-component snapshots of L_g wave propagation in a single-layer crustal model taken at a temporal spacing of 10 seconds. The homogeneous crust is 30 km thick with P– and S–wave velocities of 6.2 and 3.58 km/sec, respectively (see Figure 5). The L_g wave packet travels at a group velocity of approximately 3.33 km/sec (see Figures 3 and 4), which is appropriate for areas like the western U.S. as suggested by Mitchell and Hwang (1987). Since no scattering mechanism is present, the checkerboard-like pattern due to the constructive interference of repeatedly reflected S waves trapped in the crust is retained at all times (Figure 1). This checkerboard-like pattern undoubtedly indicates that both interpretations of L_g waves, either as multiply reflected S waves or as higher-mode surface waves, are indeed adequate.

Like the fundamental mode Rayleigh waves (R_g), planar body waves incident upon the free surface at an oblique angle also exhibit a retrograde rolling. Since L_g waves are repetitive reflections (at both the free surface and the Moho) of planar S waves, it shares the same characteristics. At greater depths, however, the particle motion of L_g is very different from that of R_g. Figure 2 shows particle motion plots of L_g synthetics recorded at five depths starting at the free surface and 2 km apart. At the anti-nodes (for example, at 4 km), the particle motion is highly linear.

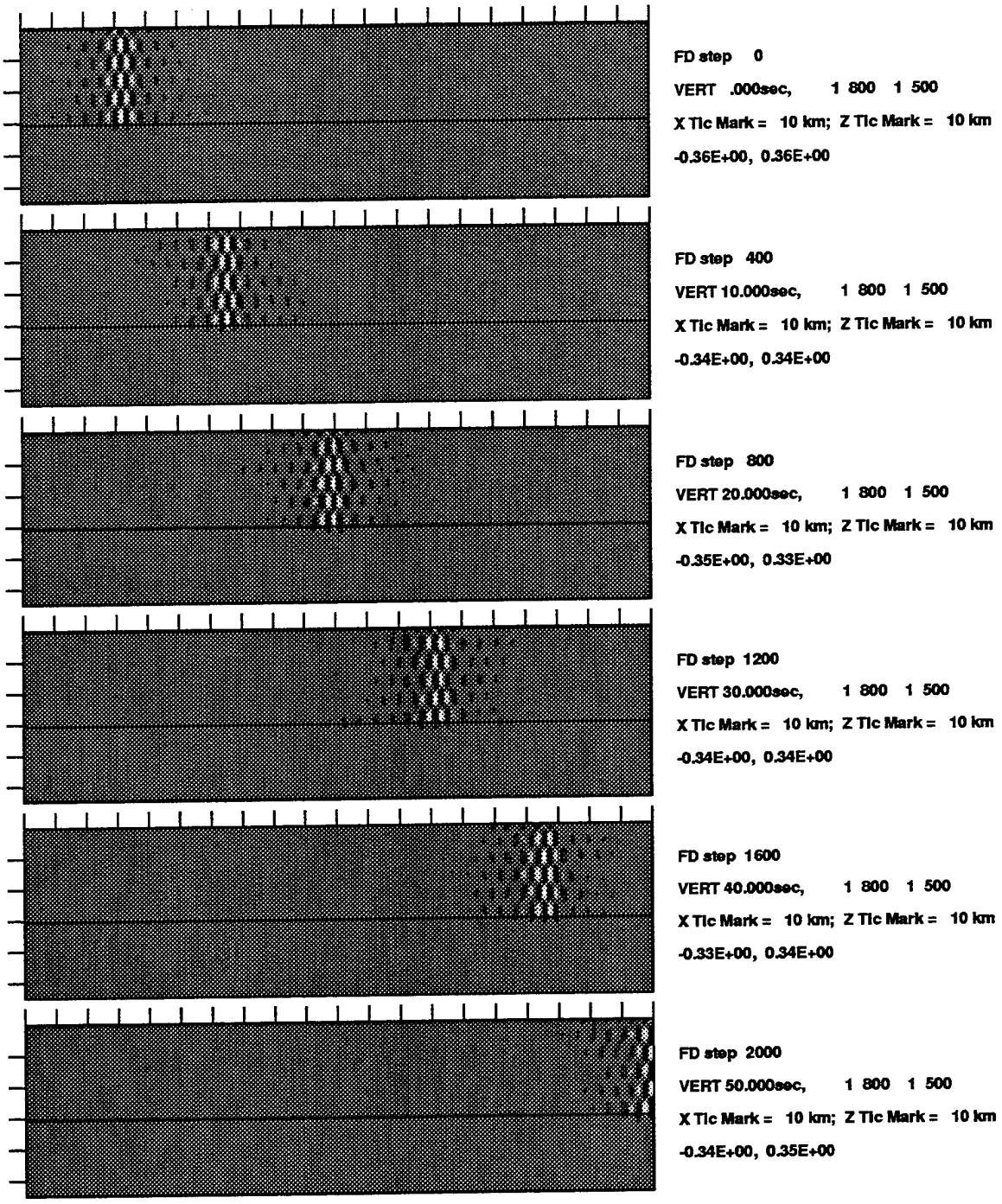

LFD Simulation of Lg Propagation: Model 00

Figure 1. The vertical-component snapshots of L_g wave propagation in a single-layer crustal model taken at a temporal spacing of 10 seconds. The homogeneous crust is 30 km thick with $P-$ and $S-$wave velocities of 6.2 and 3.58 km/s, respectively (see Figure 5). The L_g wave packet travels at a group velocity of approximately 3.33 km/s. Since no scattering mechanism is present, the checkerboard-like pattern due to the constructive interference of repeatedly reflected S waves trapped in the crust is retained at all times.

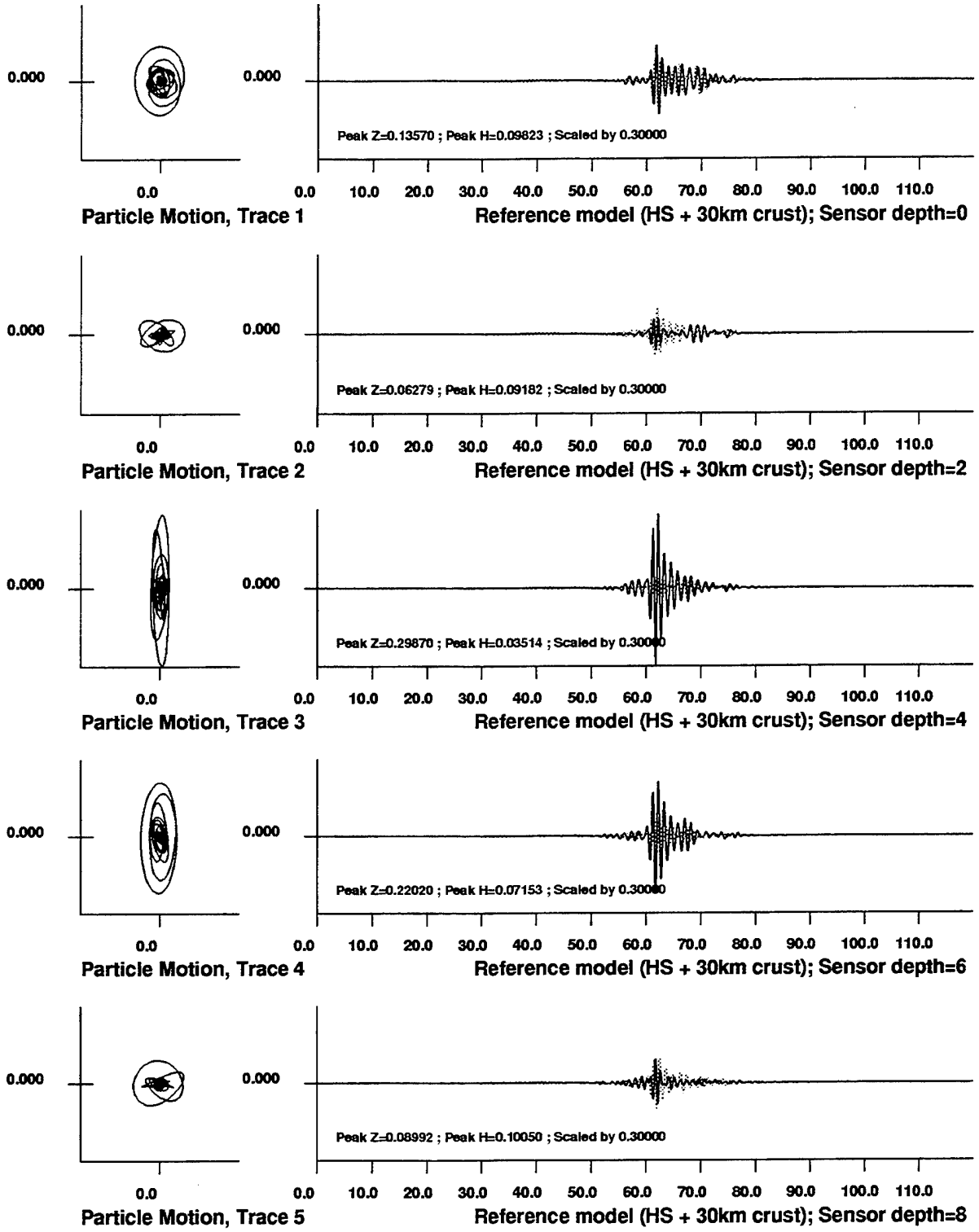

Figure 2. Synthetic seismogram (right) and corresponding particle motion (left) at five depths for the reference 1-layer model 00 (see Figure 1). Vertical and horizontal components are shown in solid and dashed lines, respectively. The sensors are 2 km apart. Note the retrograde rolling at the free surface (top) and the highly polarized shear motion at antinodes (for example, at 4-km depth).

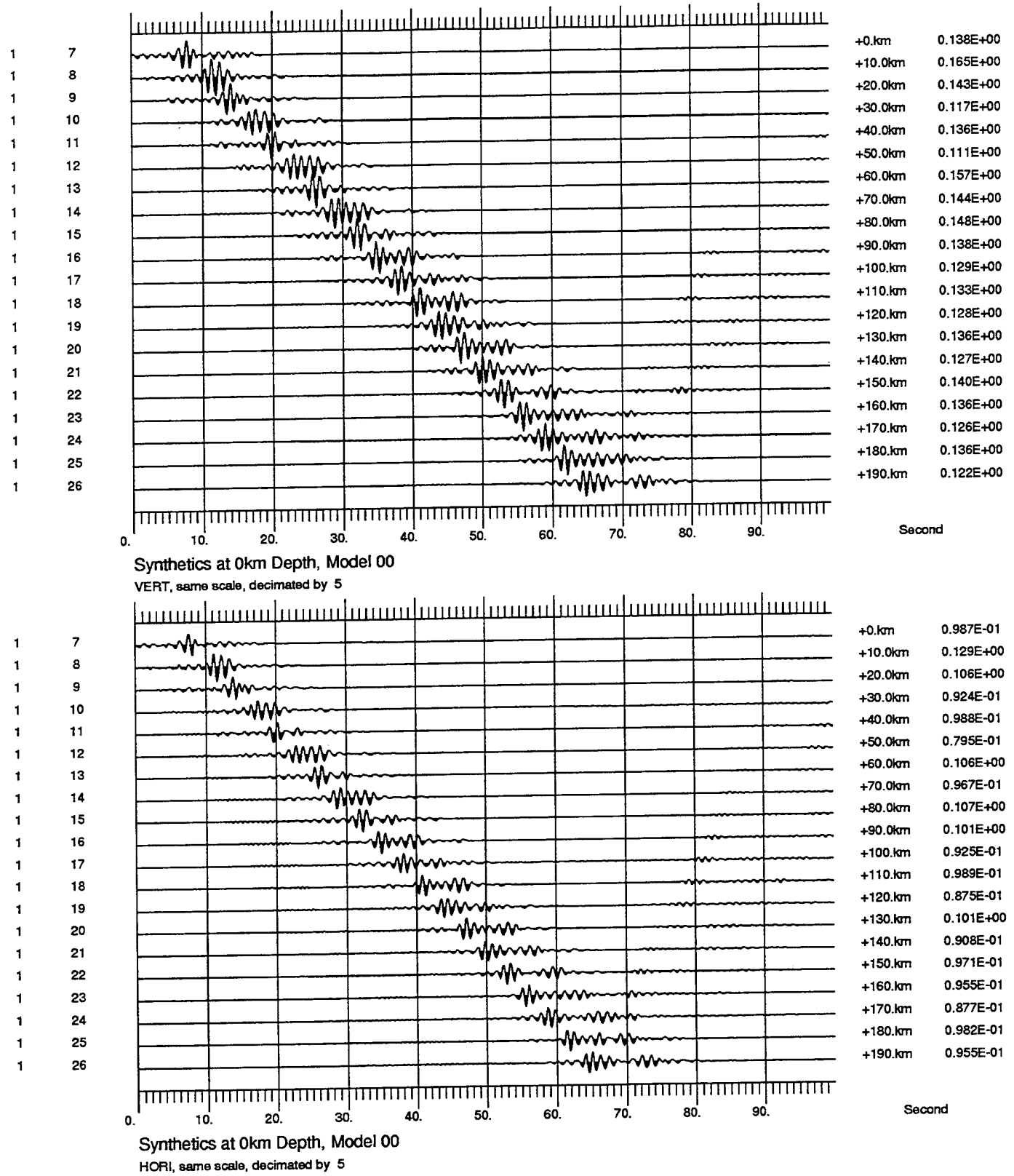

Figure 3. Vertical (top) and horizontal (bottom) seismic sections of L_g displacement synthetics for the reference 1-layer model 00. The L_g group velocity is about 3.33 (= 190/[65-8]) km/sec.

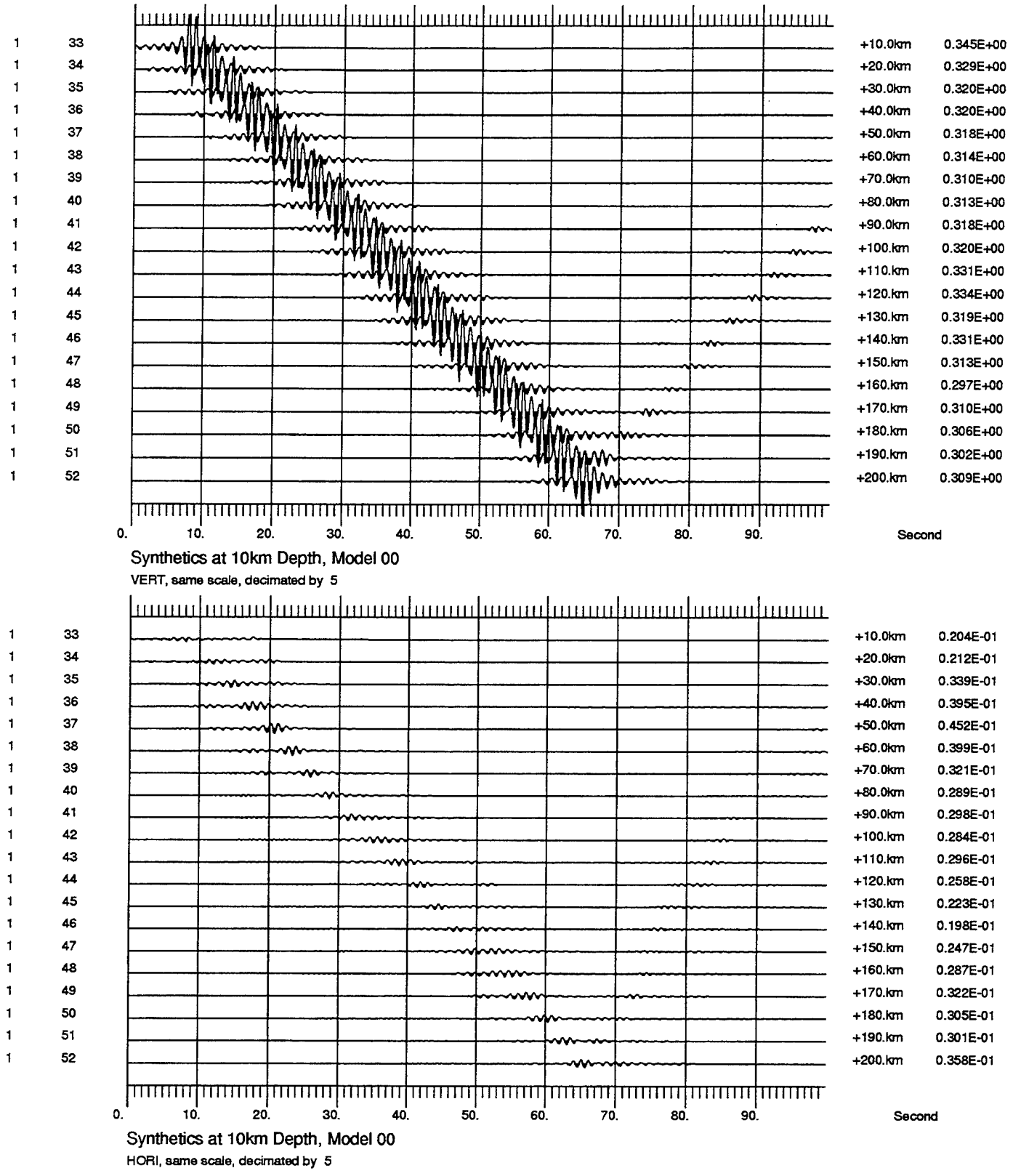

Figure 4. Vertical (top) and horizontal (bottom) seismic sections of L_g displacement synthetics recorded at a depth of 10 km for the reference 1-layer model 00. For the 6th overtone, this depth is very close to an antinode and hence the motion is highly polarized. In later sections of this study, the efficiency of L_g transmission is measured using a deep receiver to avoid the contamination from the R_g phase.

3. L_g PROPAGATION IN MODELS WITH IRREGULAR WAVEGUIDE GEOMETRY

Numerical experiments are first conducted to evaluate the effects of variable crustal thickness, mountainous relief, and sediment thickness on L_g propagation. In order to isolate these effects, all the crustal models used in the first set of LFD calculations are simple variations of the single-layer crustal model (*viz.* Model 00). Table 1 below gives a brief description of these canonical models. The upper portions of twenty five representative models are shown in Figures 5 through 9.

Table 1. Major Structural Feature(s) of Each Model

00	single-layer (homogeneous) crust of 30 km thick
0A	abrupt Moho uplift (30→6→30)
0Aa	gentle Moho uplift (30→6→30)
0B	a thinning crust (extended Moho uplift) (30→6)
0Ba	similar to 0B, with a gentle transition (30→6)
0C	extended thick sediment
0Ca	similar to 0C, with a gentle, linear transition
0Ca	similar to 0C, with a smooth transition
0D	a contained sedimentary basin
0Da	similar to 0D, with a smooth boundary
0Db	0D + a sedimentary layer
0E	crustal thickening (30→45→30, polygonal Moho)
0Ea	crustal thickening (30→45→30, smooth Moho)
0Eb	crustal thickening (30→40→30, smooth Moho)
0Ec	crustal thickening (30→50→30, smooth Moho)
0Ed	crustal thickening (30→50→30, polygonal Moho)
0F	Moho uplift + a sedimentary basin
0Fa	similar to 0F, with a smooth boundary
0Fb	Moho uplift + a sedimentary basin of slow velocity
0Fc	similar to 0Fb, with a smooth boundary
2	a moderate topography
2a	same topography as 2 with isostatic compensation
3	a moderate topography
3a	same topography as 3 with isostatic compensation
4	thickened crust with a trapezoidal Moho and free surface

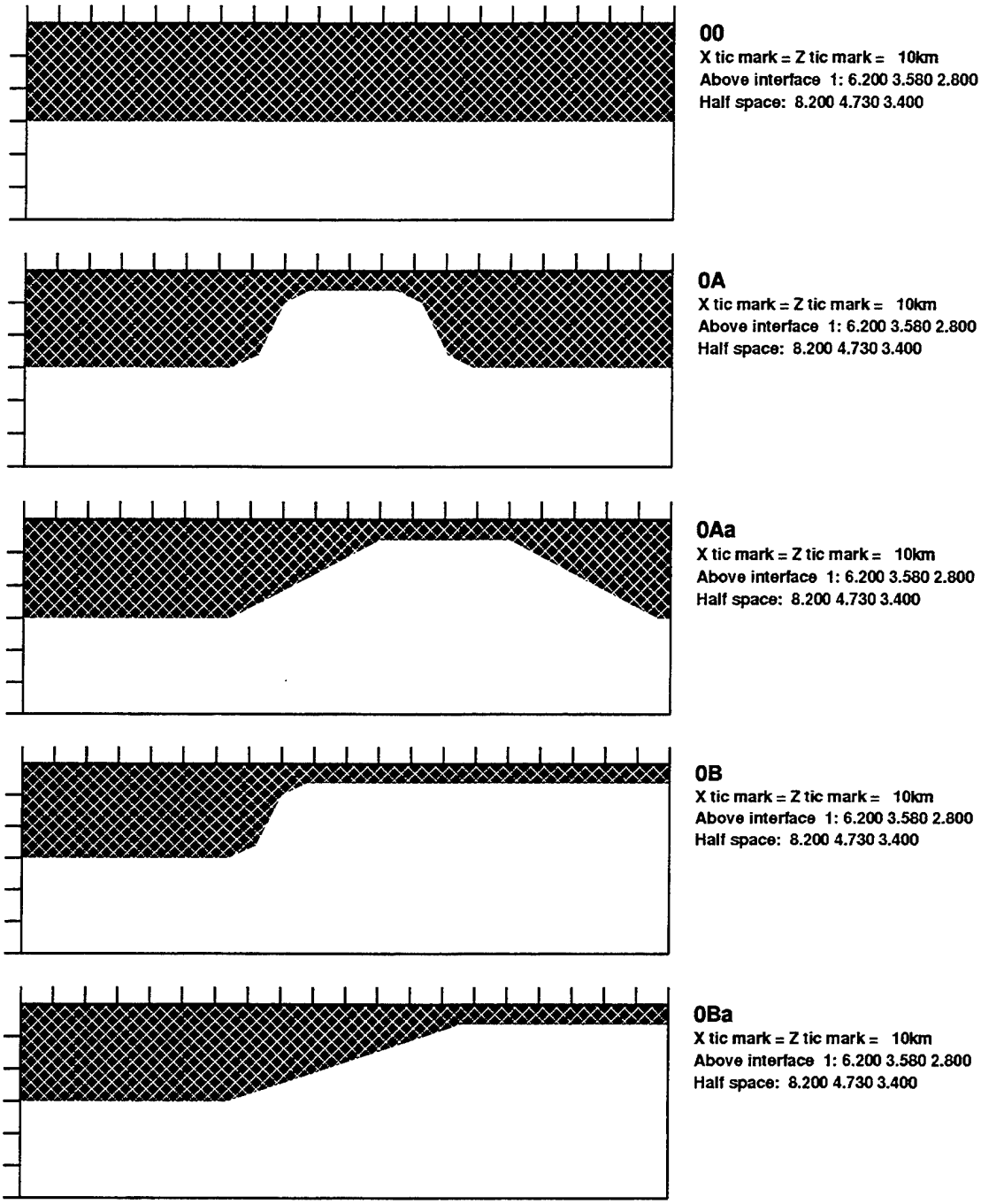

Figure 5. Five of the canonical crustal models tested in this study. Only the uppermost portion of each model is shown. The actual grid size used in LFD calculation is 1000 by 500, corresponding to 250 km by 125 km. The material parameters of each model are shown on the right. In each LFD experiment, the pure L_g wave packet is initialized in the stratified portion of the model, near the left edge of the grid. Model 00 is the laterally-invariant reference model.

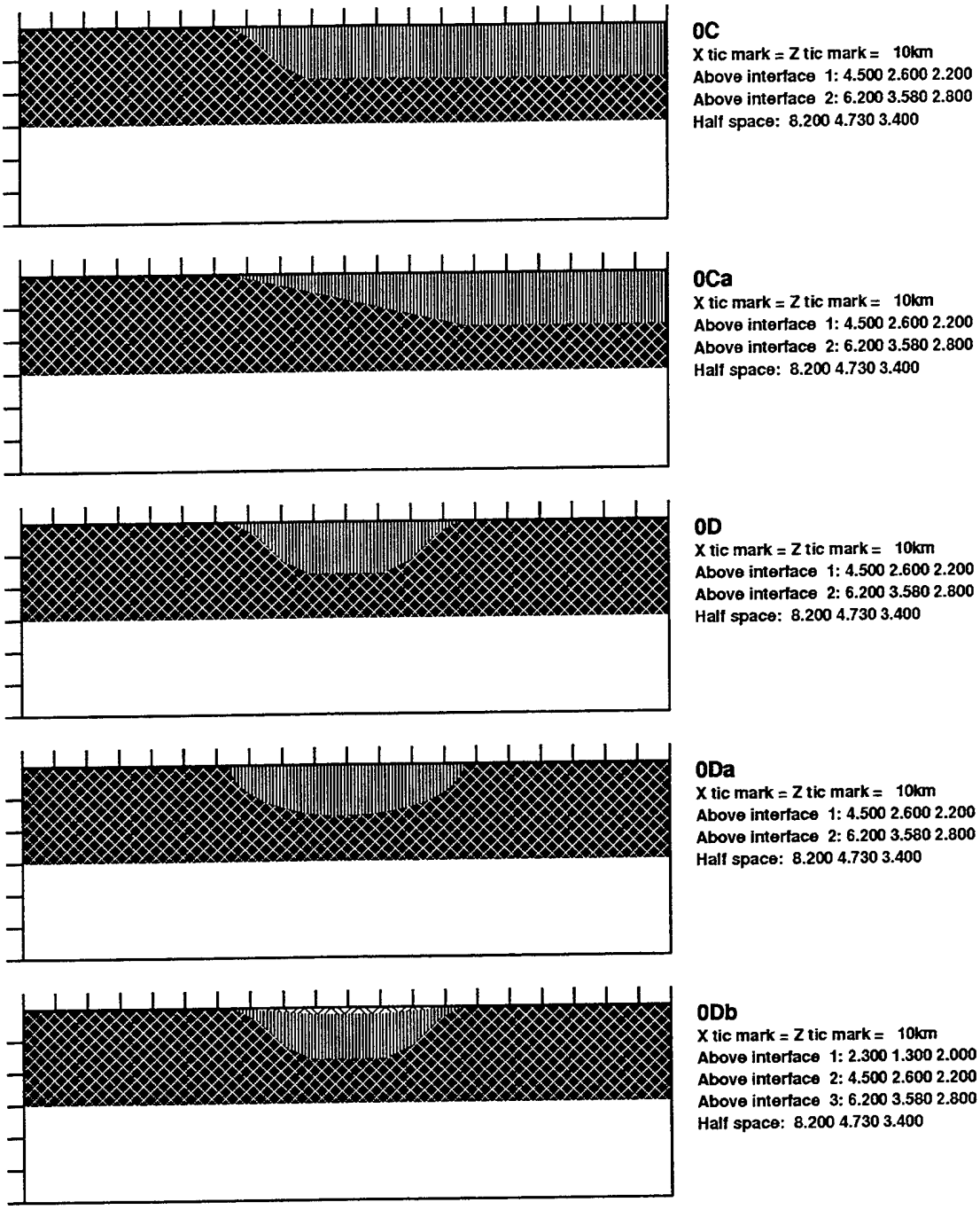

Figure 6. Same as Figure 5 except for models 0C, 0Ca, 0D, 0Da, and 0Db. Both "C" and "D" series of models have a thick sedimentary layer in the structure. The sediment is contained in models of the "D" series.

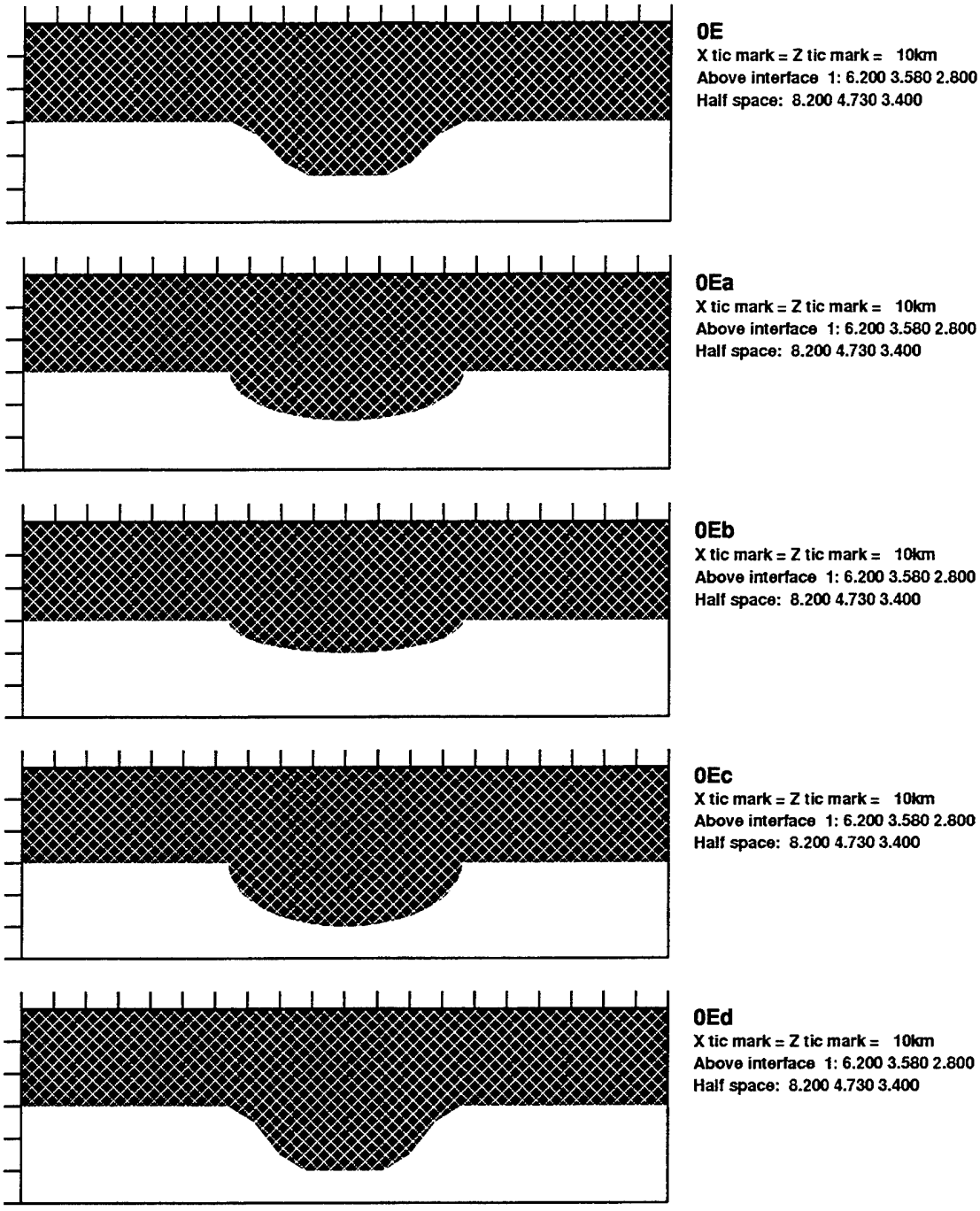

Figure 7. Same as Figure 5 except for models 0E, 0Ea, 0Eb, 0Ec, and 0Ed. All "E" series models have thickened crust.

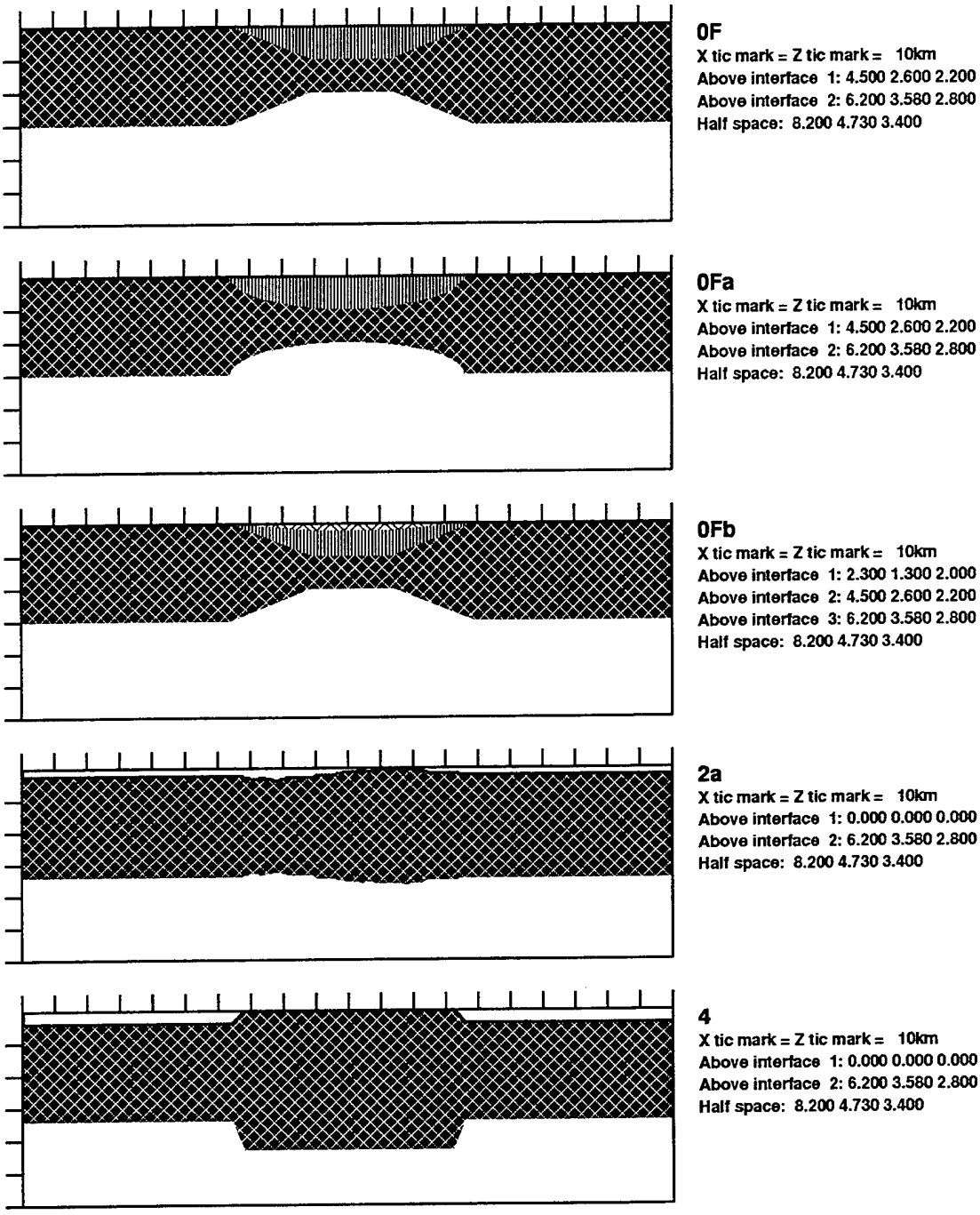

Figure 8. Same as Figure 5 except for models 0F, 0Fa, 0Fb, 2a, and 4. "F" series models are very similar to those of "D" series except that a Moho uplift is added. Model 2a has a moderate topography with a full isostatic compensation. Model 2 (not shown) has an identical free-surface topography with a flat Moho.

Figure 9 shows the vertical-component snapshots of L_g wave propagation in the model 0A, which has an abrupt Moho uplift. The bulk of the L_g energy is converted to S_n at the ascending crust-mantle interface, as shown in Figure 9 at 20 seconds. As a result, the L_g eigenfunction is broken up and only a fraction of the L_g energy would enter the oceanic crust. The amplitude of the direct L_g phase is further reduced, due to the geometric spreading, when it passes the shallow crust to enter the suddenly thickened continental crust (see, at 40 seconds). Record sections of surface synthetics for the model 0A are shown in Figure 10. While R_g remains intact, the L_g is effectively blocked, although the oceanic crust is only 50 km long. The majority of L_g energy is converted to S_n of which some crosses the descending Moho and re-enters the crust. Due to the post-critical direction, this phase will stay in the crust and become L_g at a larger distance. This phase is most prominent at 43 seconds on trace 20, and is outside the expected "on-time L_g" window.

Model 0Aa is similar to 0A except that a gentle, piecewise-linear Moho is used instead (Figure 11). The L_g-to-S_n conversion is quite clear at 20 and 30 seconds. The energy which crosses the oceanic crust as the 3rd overtone (see, at 30 seconds) does not touch the free surface as the crust thickens. Instead, it propagates along the descending Moho (see, at 40 and 50 seconds) before it reaches the flat Moho and starts to bounce back to the ground (see, at 60 seconds). The "L_g blockage" occurs because only S_n and R_g could reach ground sensors in the oceanic-to-continental transition zone. Figure 12 shows that the dominating phase of this model is the "early L_g" with a group velocity about 4.0 km/sec, followed by R_g waves with a group velocity of 3.0 km/sec. There is no prominent phase arriving at the expected "on-time" L_g window of 3.3 km/sec.

Model 0B, shown in Figure 13, has a crust that thins abruptly from a thickness of 30 km to 6 km. As it does in the "A"-series of models, a significant fraction of L_g energy enters the deeper mantle and detaches from the Moho (see, 30, 40, and 50 seconds of Figure 13). This energy never reaches the surface sensors, and as a result, the most prominent phase is the stabilized 3rd overtone, which stays in the thin crust. Record sections of this model (Figure 14) indicate that no "L_g blockage" would be observed here since the 3rd overtone has a peak amplitude and a group velocity very similar to those of the "on-time L_g" in the reference model. Changing the Moho shape does not affect these observations (see Figures 15 and 16).

All "C"-series models have a sedimentary layer 16 km thick. The sediment slows down the L_g waves, as expected (Figures 17 and 19). However, this structure does not generate a S_n conversion as strong as in other models with an irregular Moho or contained basin (Figures 18 and 20).

For models of the "D" series, because of the contained structure of the basin, the L_g wave that tunnels underneath the basin eventually recovers characteristics like a multiply bouncing SmS (Figure 21). This phase has the same group velocity of the "on-time L_g" on those surface sensors co-located

at the bounce points. The amplitude is smaller, however. A more prominent phase comes from the energy that first enters the basin and then leaks out from the ascending edge of the basin. The corner where the pinched basin ends also radiates some body waves. Figure 22 illustrates that the contained basin structure removes some energy of the "on-time L_g" and converts it to the so-called "late L_g" which has the same phase velocity as the reference L_g but is significantly delayed. Depending on the location of surface sensors, some seismographs will observe either complete or partial blockage of the "on-time L_g". Figures 23-26 show results for similar structures (models 0Da and 0Db).

Model 0E has a thickened crust and a very strong L_g-to-S_n conversion occurs along the ascending interface (see, 30, 40, and 50 seconds of Figure 27). Horizontal-component snapshots (not shown) indicate that some focusing of energy occurs at the corner where the Moho turns flat. This corner becomes a secondary point source radiating upgoing body waves. Sensors right above this corner would detect a prominent arrival due to a nearly vertical incidence of shear waves (see traces 16 and 17 of Figure 28). Figures 29-36 show variations of thickened sections of crust (models 0Ea through 0Ed).

"F"-series models have both a sedimentary basin and a Moho uplift. Figure 37 shows the basic geometry. The Moho uplift causes a strong S_n conversion (see, at 20 seconds of Figure 38). The pinched end of the basin radiates body waves outward, and some of those rays leak into deeper mantle. Figure 39 shows the horizontal-component snapshots of L_g wave propagation in the model 0Fa which is similar to 0F except for a smooth interfaces. Observations similar to those with the model 0F can be made. The pinched end of the basin radiates body waves outward, and some of those rays leak into deeper mantle (see, at 50 seconds). Some direct P waves are also present (see, at 40 seconds). Direct P waves radiated from the basin's terminating edge can be seen on the horizontal components of Figure 40. Figure 41-44 show the geometry and results for some other variations (models 0Fb and 0Fc).

Model 2 has a flat Moho and a moderate free-surface topography (Figure 45). The L_g–to–S_n conversion is relatively weak (see Figure 46). This is very different from the case of R_g where scattering by rough topography would cause very strong apparent attenuation. Model 2a has a fully compensated Moho added to the model (Figure 47). The fully compensated Moho gives results similar to those from the flat Moho of model 2. Figures 47 through 54 give results from models 2a, 3, 3a, 3a, and 4, which are all similar to model 2.

Figures 55 and 56 display the vertical-component synthetic seismograms recorded at 3 depths (0km, 10km, and 40km) and started at 20 seconds for models 00, 0A, 0Aa, 0B, 0Ba, 0C, 0Ca, 0D, 0Da, and 0Db. Figures 57 and 58 show the same for models 0E, 0F, 0Fa, 0Fc, and 2a starting at time zero. Note that although the "on-time L_g" on surface synthetics of models 0B and 0Ba (bottom left) have a peak amplitude in the same order as that of the reference model, they are not the same overtone of the Rayleigh mode. The moderate surface and Moho topography in the model 2a only affect L_g waveform

characteristics mildly. Note that model 0Fc excites very strong R_g phase, very similar to the model 0Db. Among all structures tested, "E" series of models (with a thickened crust) excites the strongest S_n conversion (see Figure 27).

It is interesting to note that all models of the "F" series exhibit significant L_g-to-P_g conversion. The peak horizontal amplitude on trace No.25 ranges from 10% to 15% of that of the original L_g wave train. To a lesser extent, models of "C" and "D" series as well as models 0A and 0Ba also generate the same conversion.

For each model, the synthetic seismograms are recorded at three linear arrays at three different depths: 0 km, 10 km, and 40 km. Several parameters are measured to infer the relationship between the major geological/geophysical/geometrical features and possible blockage and S_n coupling. The amplitude spectrum of a surface synthetic seismogram far away from the heterogeneous structure is computed using a window of 12.8 seconds (512 data points) around the group velocity of 3.33 km/sec. Using the spectrum of model 00 as a reference, the amplitude ratio at 1 Hz is denoted as "BK" in Table 2 to quantify the L_g blockage. This ratio is also used to compute the equivalent apparent attenuation of the "on-time L_g". Both the quality factor Q_0 and the attenuation coefficient γ are printed in Table 2. To measure the total transmitted L_g energy, a sensor at 10 km depth is used. The spectral amplitude ratio at 1 Hz computed with this sensor is denoted as "T" in Table 2. The converted S_n energy is measured with a sensor at a depth of 40 km, below the flat Moho. Another sensor, which is near the bottom of the model and under the major heterogeneous feature, records the waveform representing the converted teleseismic energy. Except for the quantity BK, all other ratios are normalized to the 10km-deep synthetic of the model 00 as the reference. The results in Table 2 are sorted by the the major structural features of the models. There appear to be some systematic patterns that are very interesting.

Table 2. L_g Propagation Statistics of Deterministic Models

Model	BK	T	S_n/L_g	far-P/L_g	far-S/L_g	Q_0	γ (1 Hz)
0A	0.349	0.346	0.164	0.110	0.105	91	0.0105
0Aa	0.416	0.689	0.216	0.083	0.087	109	0.0088
0Ab	0.384	0.624	0.233	0.080	0.079	100	0.0096
0B	1.035	—	0.546	0.109	0.103	—	—
0Ba	0.848	—	0.482	0.041	0.044	581	0.0016
0C	0.354	0.790	0.084	0.061	0.048	92	0.0104
0Ca	0.237	0.521	0.076	0.026	0.010	66	0.0144
0Cb	0.307	0.496	0.065	0.051	0.034	81	0.0118
0D	0.595	0.565	0.161	0.075	0.084	185	0.0052
0Da	0.317	0.577	0.185	0.073	0.096	84	0.0115
0Db	0.508	0.409	0.102	0.083	0.086	142	0.0068
0E	0.977	0.779	0.468	0.046	0.051	4136	0.0002
0Ea	0.963	0.723	0.459	0.038	0.082	2534	0.0004
0Eb	0.967	0.649	0.201	0.032	0.050	2821	0.0003
0Ec	0.983	0.719	0.478	0.052	0.070	5558	0.0002
0Ed	0.923	0.741	0.318	0.058	0.039	1191	0.0008
0F	0.228	0.580	0.177	0.058	0.062	65	0.0148
0Fa	0.789	0.595	0.225	0.076	0.084	405	0.0024
0Fb	0.318	0.533	0.157	0.070	0.087	84	0.0115
0Fc	0.473	0.560	0.194	0.078	0.098	128	0.0075
2	1.023	0.574	0.087	0.058	0.127	—	—
2a	1.020	0.717	0.152	0.059	0.138	—	—
3	0.875	0.829	0.091	0.061	0.145	721	0.0013
3a	1.111	0.715	0.133	0.070	0.150	—	—
4	1.738	0.408	0.319	0.050	0.072	—	—

BK: spectral amplitude ratio at 1 Hz of "on-time L_g" (3.33 km/sec) to that of the reference model.

T: spectral amplitude ratio at 1 Hz of transmitted L_g (recorded at a depth of 10 km) to that of the reference model.

Sn/Lg: spectral amplitude ratio at 1 Hz of converted S_n to the reference L_g.

far-P/Lg: spectral amplitude ratio at 1 Hz of converted teleseismic P to the reference L_g.

far-S/Lg: spectral amplitude ratio at 1 Hz of converted teleseismic S to the reference L_g.

For seismic stations in northern Scandinavia, the 1 Hz L_g waves from Novaya Zemlya are severely blocked. Based on the coda Q method, Nuttli (1988) deduced a Q_0 value of 252 for the path from Novaya Zemlya to WWSSN station KEV (Kevo, 69.755°N, 27.007°E). Using a joint inversion method with L_g amplitude measurements, Jih *et al.* (1995) point out that this Q_0 value appears to be appropriate. Assuming that the coda Q method really provides an independent and consistent measure

of L_g Q, then there should be a L_g –mb bias of 0.26 magnitude unit [m.u.] between the Eastern U.S. and Novaya Zemlya. The Q_0 value of 252 for station KEV actually includes the gross reduction effects on L_g amplitude due to both the intrinsic attenuation and the geometrical blockage, of which the latter was not fully studied or documented at the time Nuttli estimated the yield for Novaya Zemlya explosions. The continental path crossing Barents Shelf is a classical example of "L_g blockage" (Baumgardt, 1991). For blockage of the "on-time L_g" to be noticeable at similar distance, it is reasonable to expect to have a Q_0 value no more than 270, or equivalently, a BK no greater than approximately 0.7.

Using a BK of 0.7 as the threshold, we see that all models of the "A", "C", and "D" series as well as most of the "F" series would block L_g, while none of the "B" and "E" models or any model with a mild topography would block L_g. All "E"-type of models, which have a thickened crust, exhibit very little attenuation. Most of the topographic models (that is, models 2, 2a, 3a, and 4) actually exhibit an amplification, instead of reduction, in L_g amplitude. The thinning of the crust is an important mechanism to block L_g (Figures 8 and 10), as reported in many observational studies. However, the thinning itself has to be of finite span in the lateral direction. The two "B" series of models either show an amplification or have a BK larger than 0.85 (see Figures 12 and 14).

The comparison of L_g coupling to teleseismic phases is also described in Table 2. In terms of L_g-to-S_n conversion, models 0B and 0Ba are the most efficient ones, followed by four models with thickened crust, 0E, 0Ea. 0Ec, and 0Ed. Another "E"-type model, 0Eb, with an elliptical Moho shape as in model 0Ea but only 40 km thick, gives a much weaker S_n excitation. On the other hand, all these "E" series models have very comparable efficiency in L_g transmission - either measured at the free surface or at a depth of 10 km. Model 4 has a trapezoidal mountain (5 km high) on the top and a trapezoidal intrusion of 10 km in the bottom of the crust. Thus its overall increase in thickness is identical to that of models 0E and 0Ea. While the level of S_n conversion is in the same range as other "E" models, the L_g transmission is actually amplified. If the models are sorted by the corresponding levels of S_n conversion, we have {0B,0Ba} > {0E,0Ea,0Ec,0Ed} >> 4 > 0A,0Eb > 0F* > 0D*,2a,3a > 2,3 > 0C*.

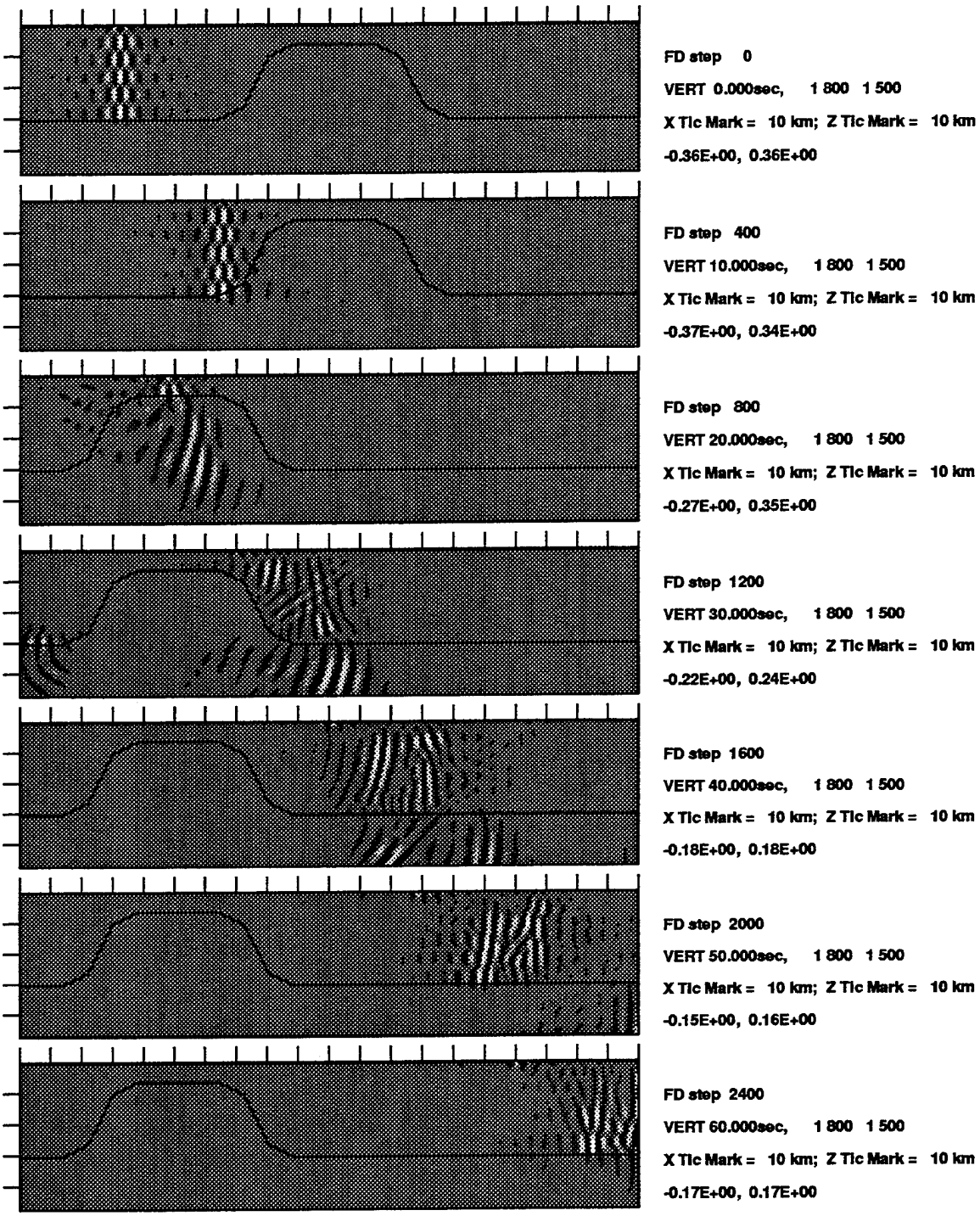

LFD Simulation of Lg Propagation: Model 0A

Figure 9. The vertical-component snapshots of L_g wave propagation in the model 0A, which has an abrupt Moho uplift. The bulk of L_g energy is converted to S_n at the ascending crust-mantle interface (see, at 20 seconds). As a result, the L_g eigenfunction is broken up and only a fraction of the L_g energy would enter the oceanic crust. The amplitude of the direct L_g phase is further reduced (due to the geometric spreading) when it passes the shallow crust to enter the suddenly thickened continental crust (at 40 seconds). Although the oceanic crust is only 50 km long, it effectively blocks the L_g.

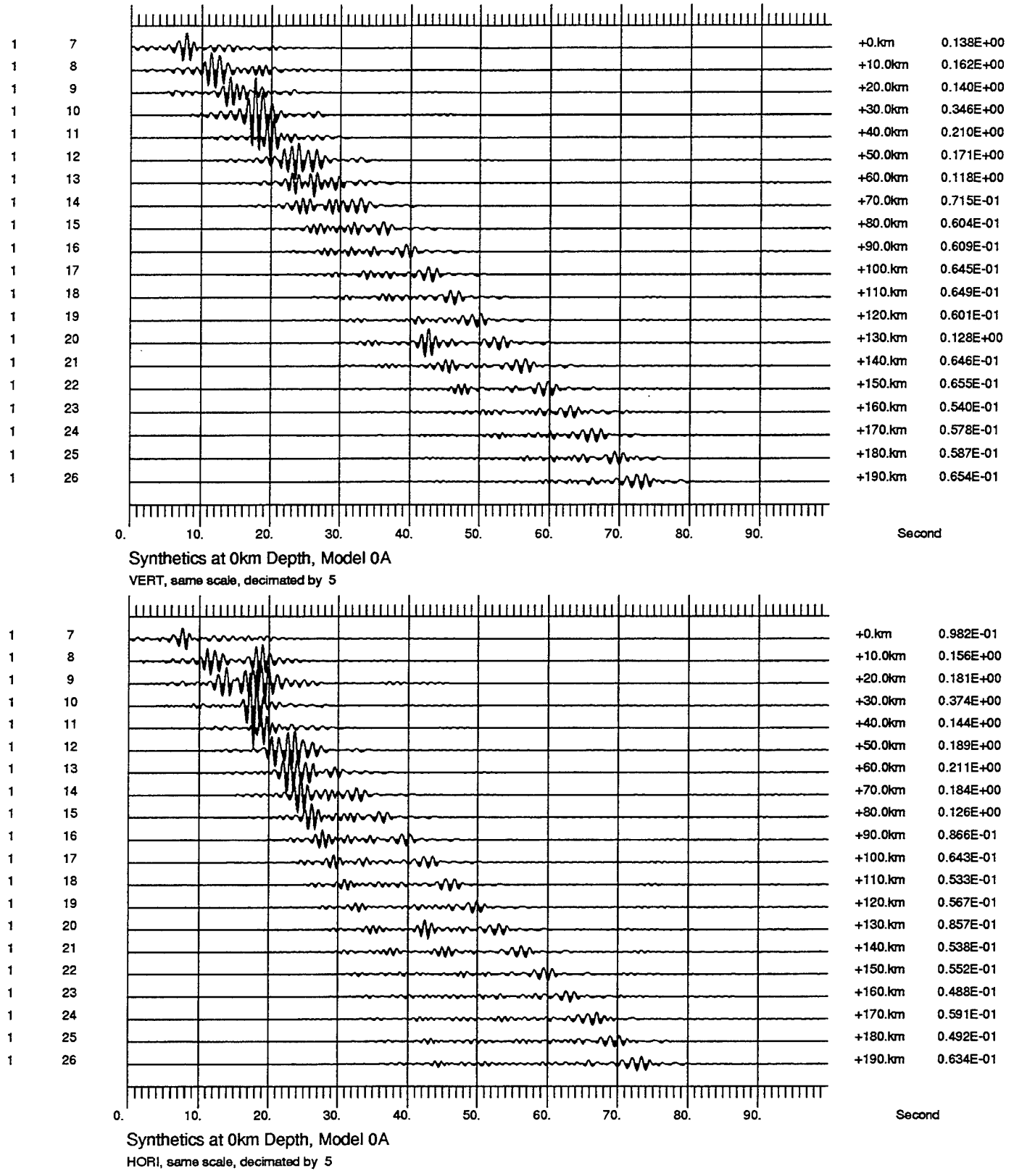

Figure 10. Record sections of surface synthetics for the model 0A. While R_g is intact, the L_g is effectively blocked. The majority of L_g energy is converted to S_n of which some crosses the descending Moho and re-enters the crust. Due to the post-critical direction, this phase will stay in the crust and become L_g at a larger distance. This phase is most prominent at 43 seconds on trace 20, and is outside the expected "on-time L_g" window.

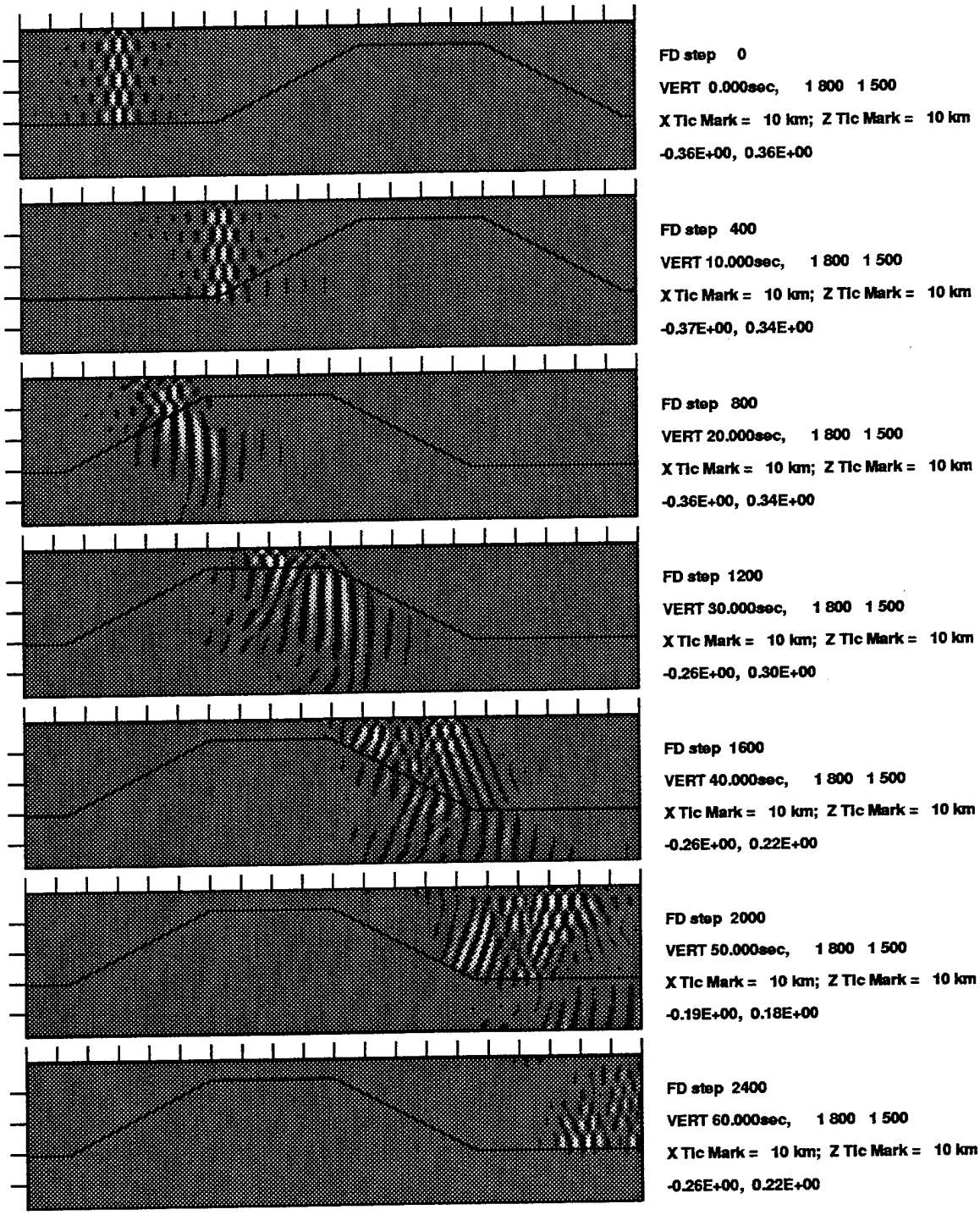

LFD Simulation of Lg Propagation: Model 0Aa

Figure 11. Same as Figure 9 except for the model 0Aa, which has a gentle continental-to-oceanic transition. The L_g -to-S_n conversion is quite clear at 20 and 30 seconds. The energy that crosses the oceanic crust as the 3rd overtone (see, at 30 seconds) does not touch the free surface as the crust thickens. Instead, it propagates along the descending Moho (at 40 and 50 seconds) before it reaches the flat Moho and starts to bounce back to the ground (see, at 60 seconds). The "L_g blockage" occurs because only S_n and R_g could reach ground sensors in the oceanic-to-continental transition zone.

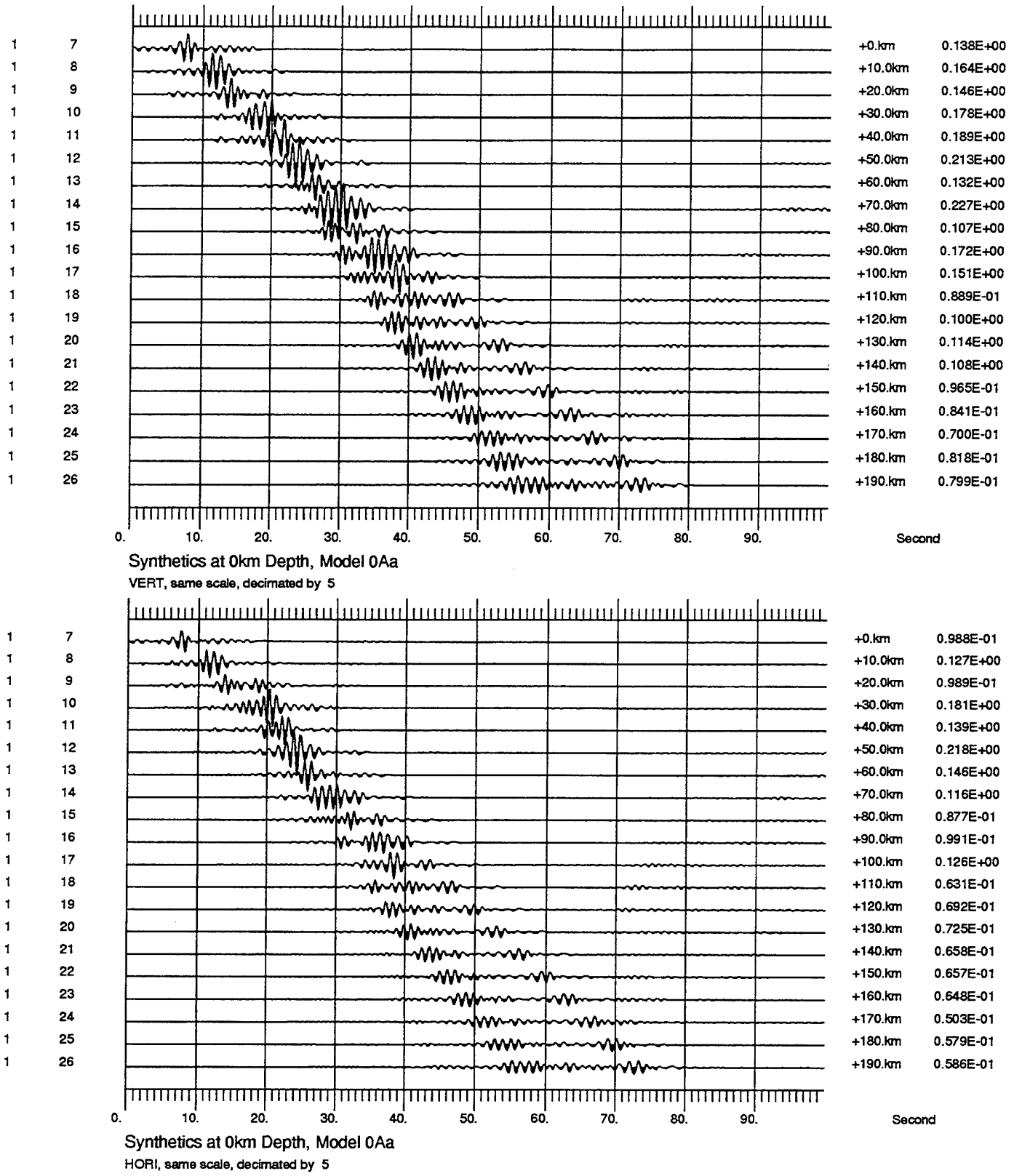

Figure 12. Seismic sections of surface synthetics for the model 0Aa. The dominating phase is the "early L_g" with a group velocity about 4.0 km/sec, followed by R_g waves with a group velocity of 3.0 km/sec. There is no prominent phase arriving at the expected "on-time" L_g window at 3.3 km/sec.

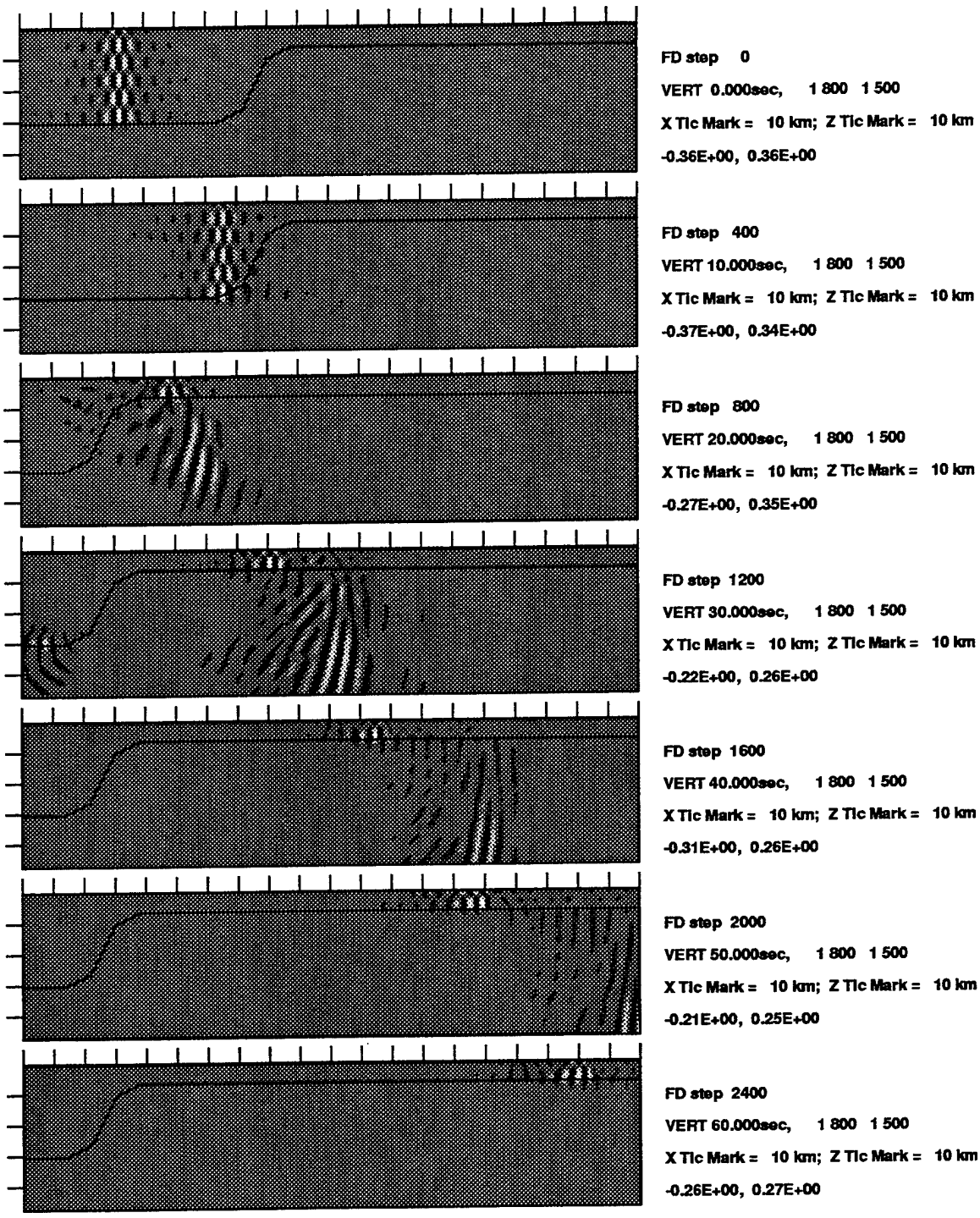

LFD Simulation of Lg Propagation: Model 0B

Figure 13. The vertical-component snapshots of L_g wave propagation in model 0B in which the crustal thickness decreases abruptly from 30 to 6 km. A significant fraction of L_g energy enters the deeper mantle and detaches from the Moho (see 30, 40, and 50 seconds). This energy never reaches the surface sensors, and as a result, the most prominent phase is the stabilized 3rd overtone, which stays in the thin crust.

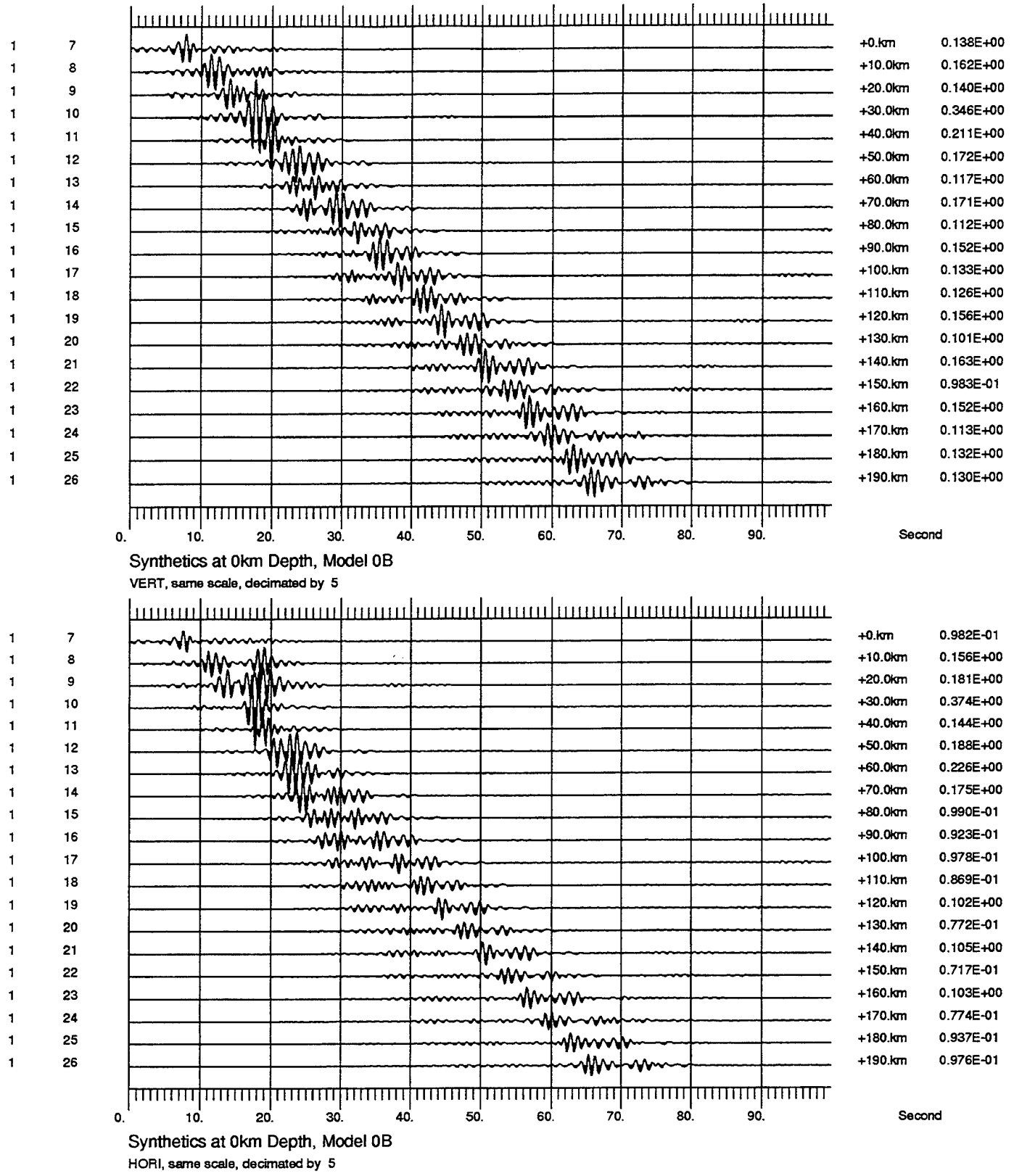

Figure 14. Seismic sections of surface synthetics for model 0B. The most prominent phase is the 3rd overtone converted from the original L_g. Note that no "L_g blockage" would be observed here since this 3rd overtone has a peak amplitude and a group velocity very similar to those of the "on-time L_g" in the reference model (see Figure 3).

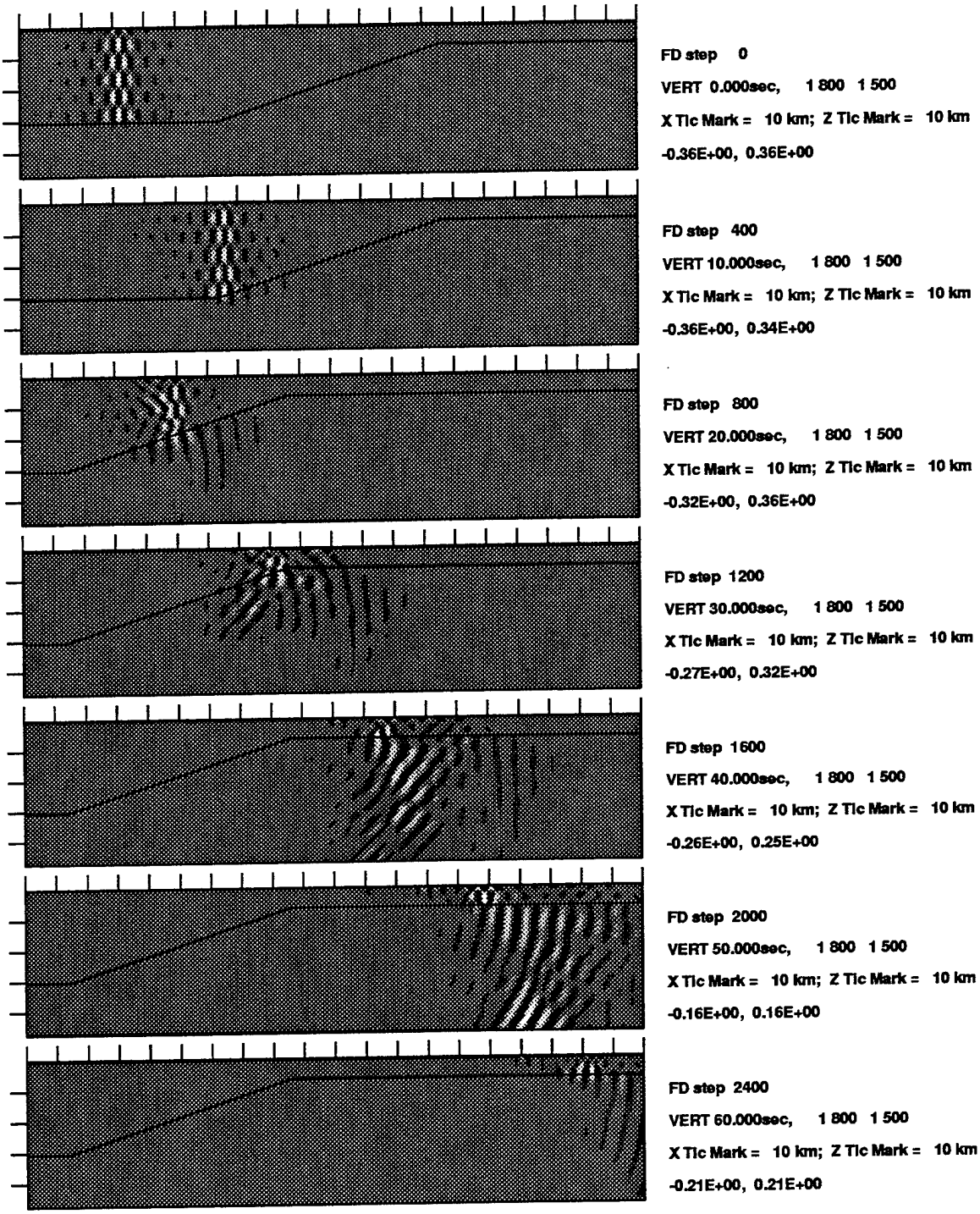

LFD Simulation of Lg Propagation: Model 0Ba

Figure 15. The vertical-component snapshots of L_g wave propagation in model 0Ba with a crustal thickness gradually decreasing from 30 to 6 km. As in model 0B, the L_g is only partially blocked with some energy traveling within the thin crust as the 3rd overtone. Much of the energy leaks into deeper mantle apparently in the form of body waves radiating from the corner where the thin crust starts, which is easier to see on the horizontal component.

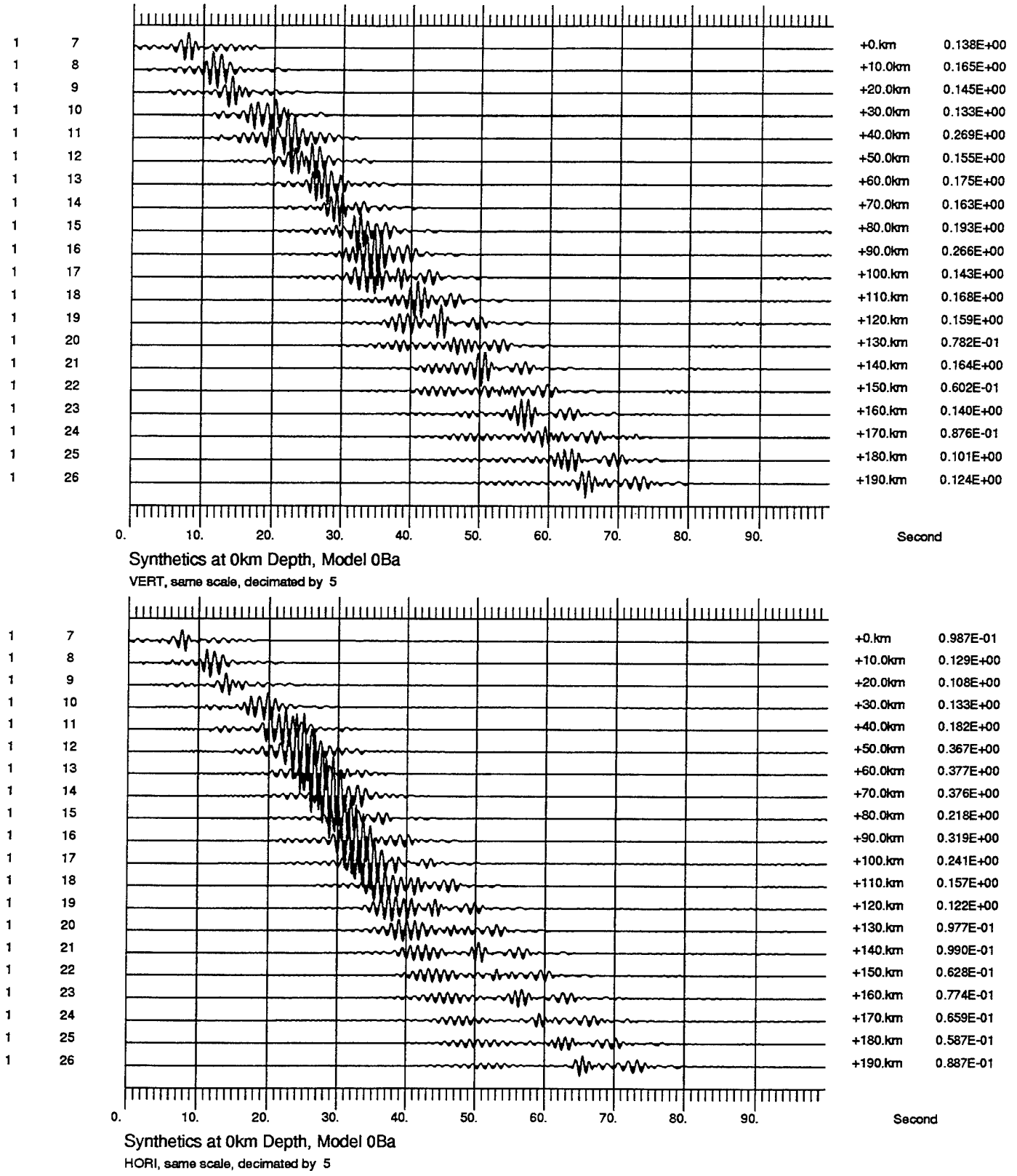

Figure 16. Seismic sections of surface synthetics for model 0Ba. The most prominent phase on trace No. 26 is the 3rd overtone converted from the original L_g, which arrives "on-time" and hence only a partial blockage is observed. A strong L_g-to-P conversion at the corner generates a very prominent arrival on the horizontal component. This phase dies out very fast on the surface recordings.

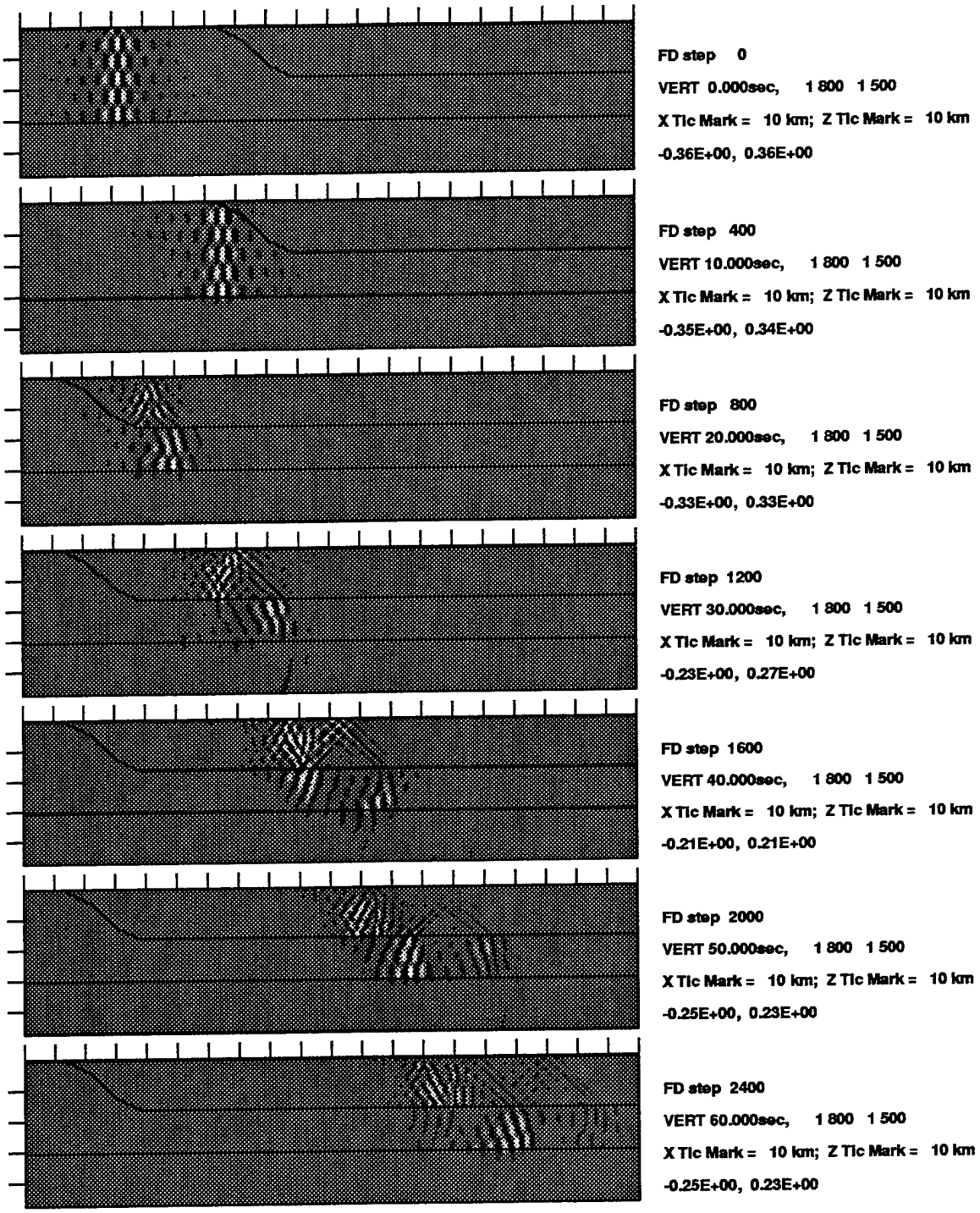

LFD Simulation of Lg Propagation: Model 0C

Figure 17. The vertical-component snapshots of L_g wave propagation in model 0C, which has a sedimentary layer 16 km thick. The sediment slows down the L_g waves, as expected. However, this structure does not generate a S_n conversion as strong as in other models with irregular Moho or contained basin.

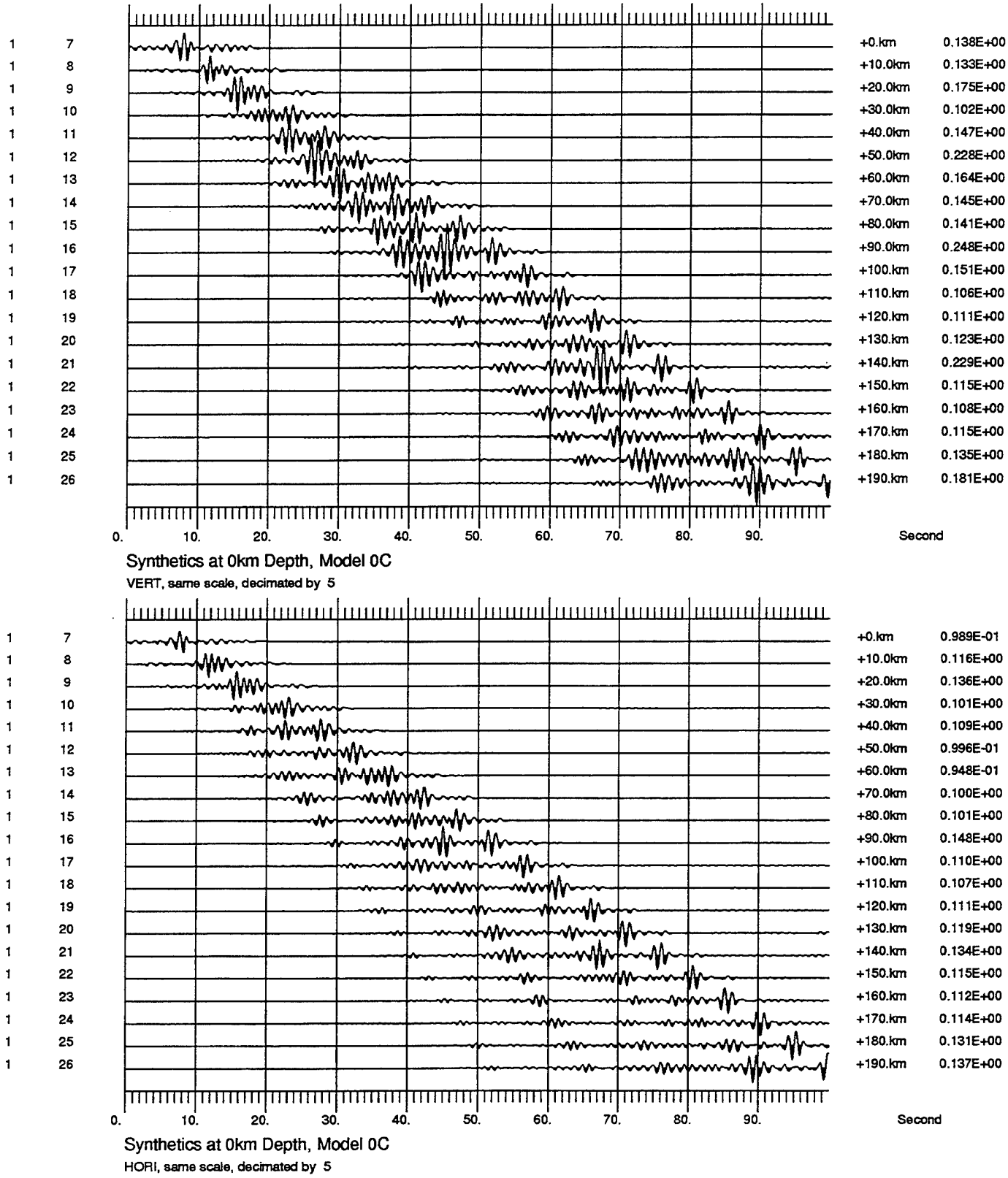

Figure 18. Seismic sections of surface synthetics for model 0C.

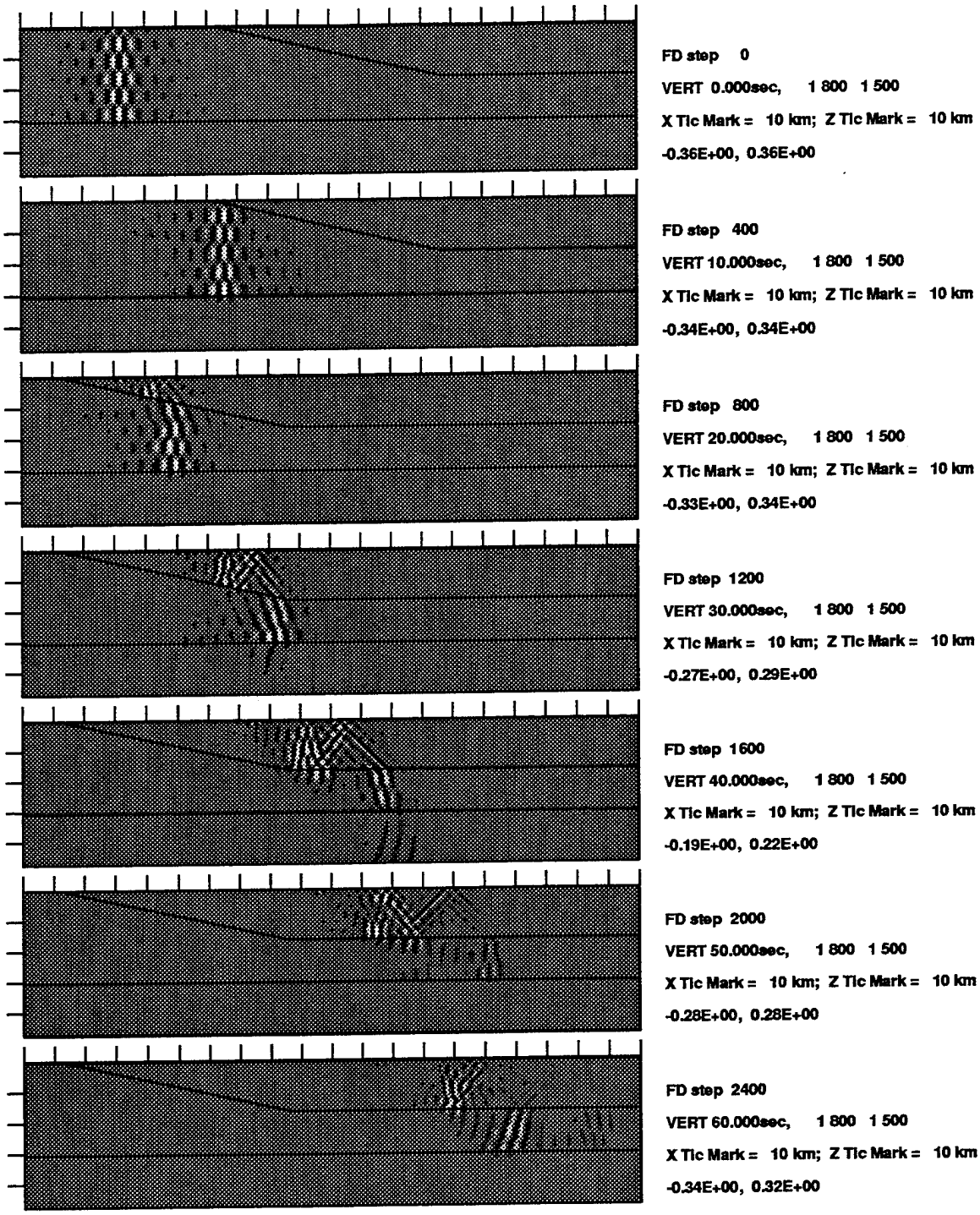

LFD Simulation of Lg Propagation: Model 0Ca

Figure 19. Same as Figure 17 except that the basin has a gentle edge.

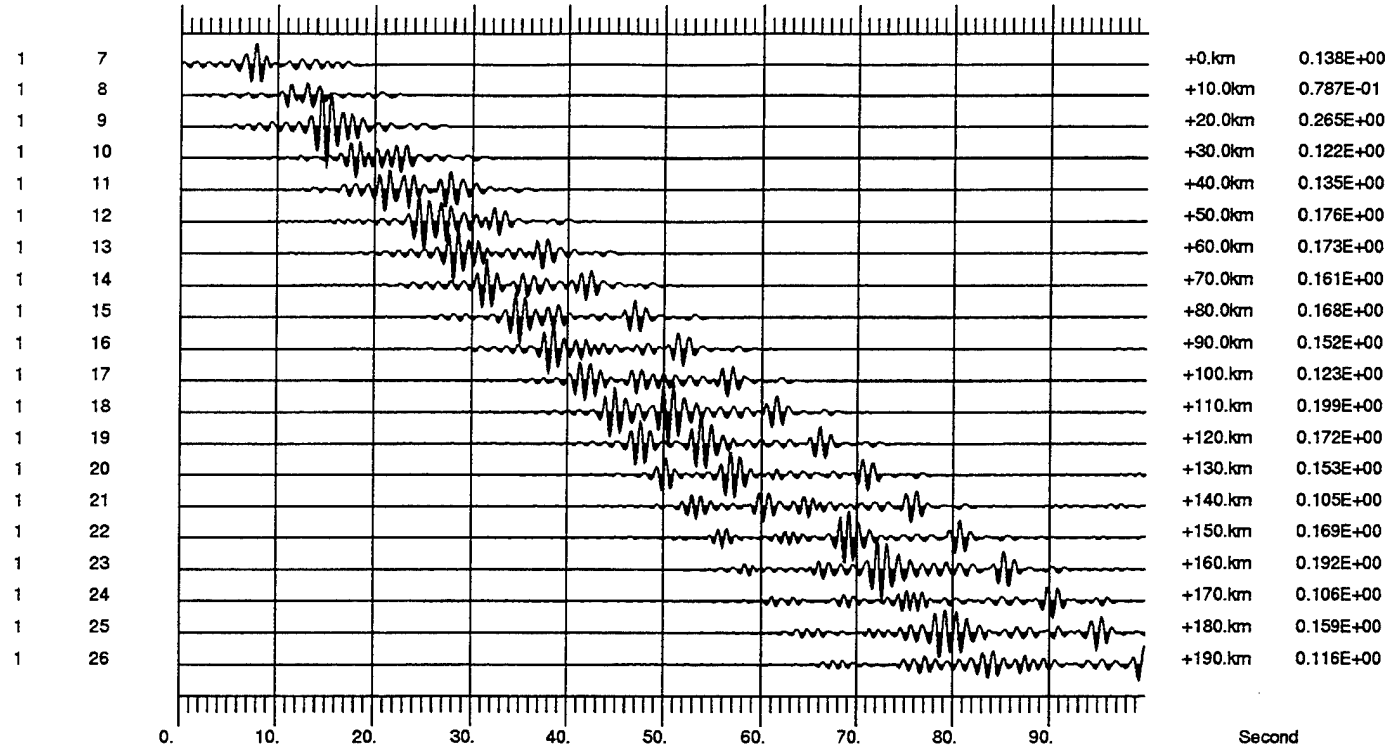

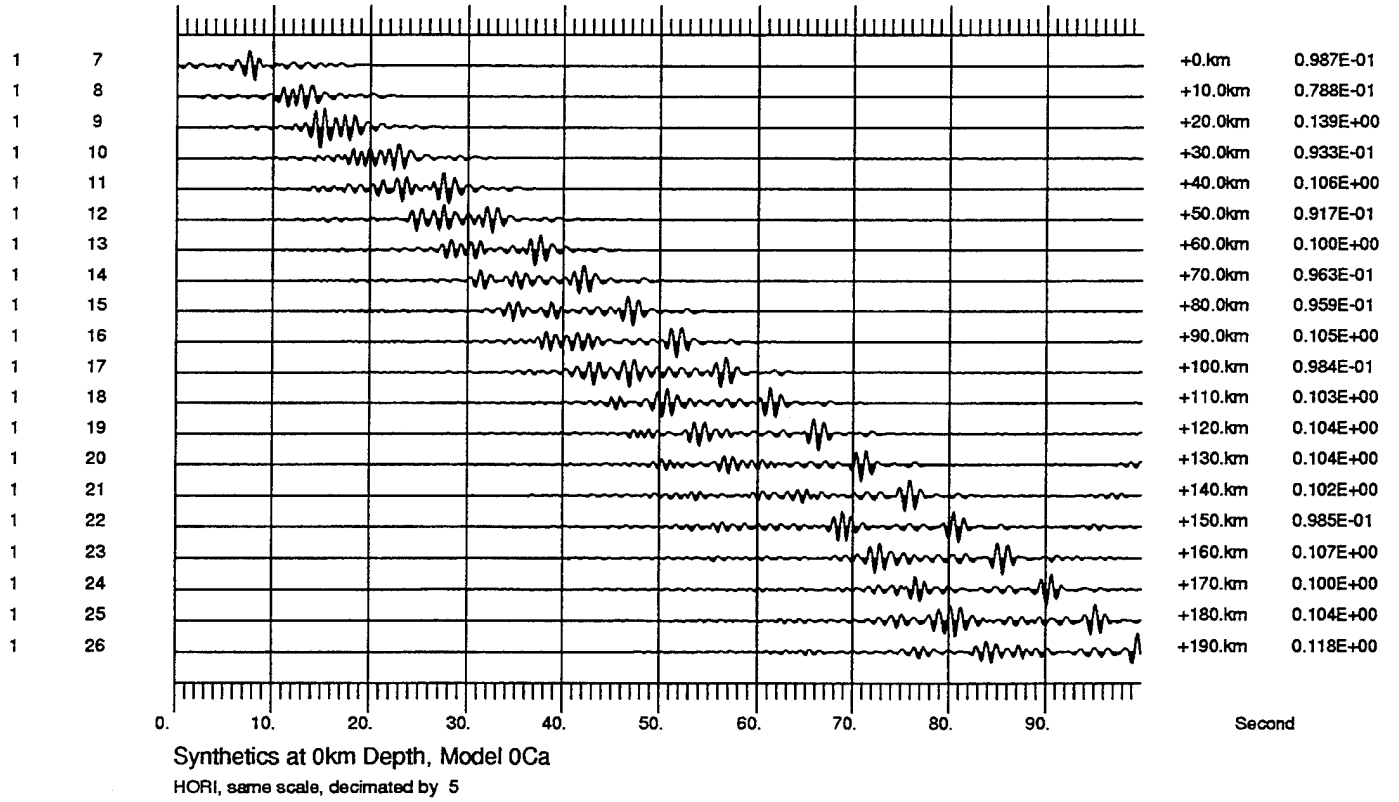

Figure 20. Seismic sections of surface synthetics for model 0Ca.

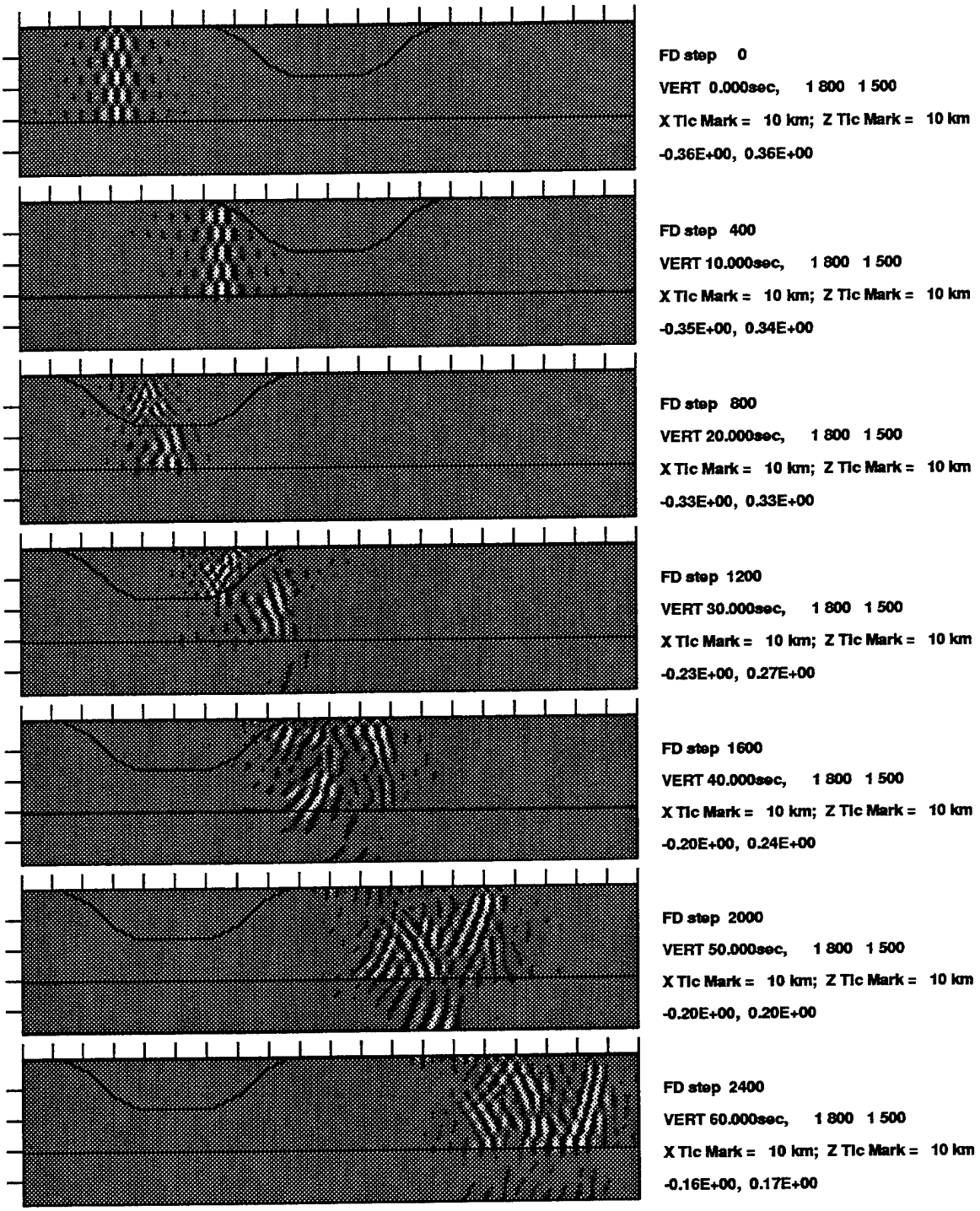

LFD Simulation of Lg Propagation: Model 0D

Figure 21. Because of the contained structure of the basin, the L_g that tunnels underneath the basin eventually recovers characteristics like a multiply bouncing SmS. This phase has the same group velocity as the "on-time L_g" on those surface sensors co-located at the bounce points. The amplitude is smaller, however. A more prominent phase comes from the energy that first enters the basin and then leaks out from the ascending edge of the basin. The corner where the pinched basin ends also radiates some body waves.

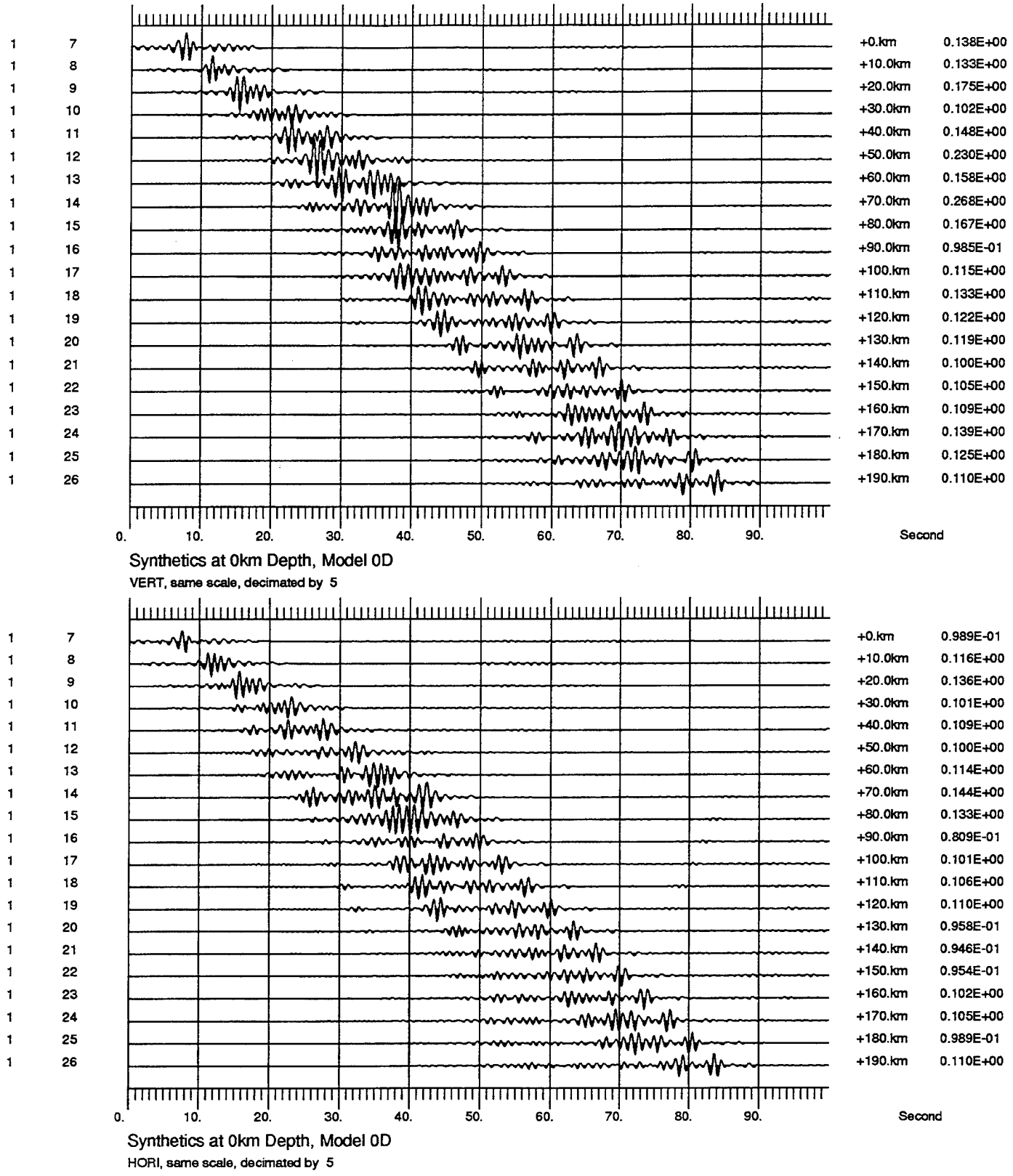

Figure 22. The contained basin structure removes some energy from the "on-time L_g" and converts it to the so-called "late L_g" which has the same phase velocity as the reference L_g but is significantly delayed. Depending on the location of surface sensors, some sensors will observe either complete or partial blockage of the "on-time L_g".

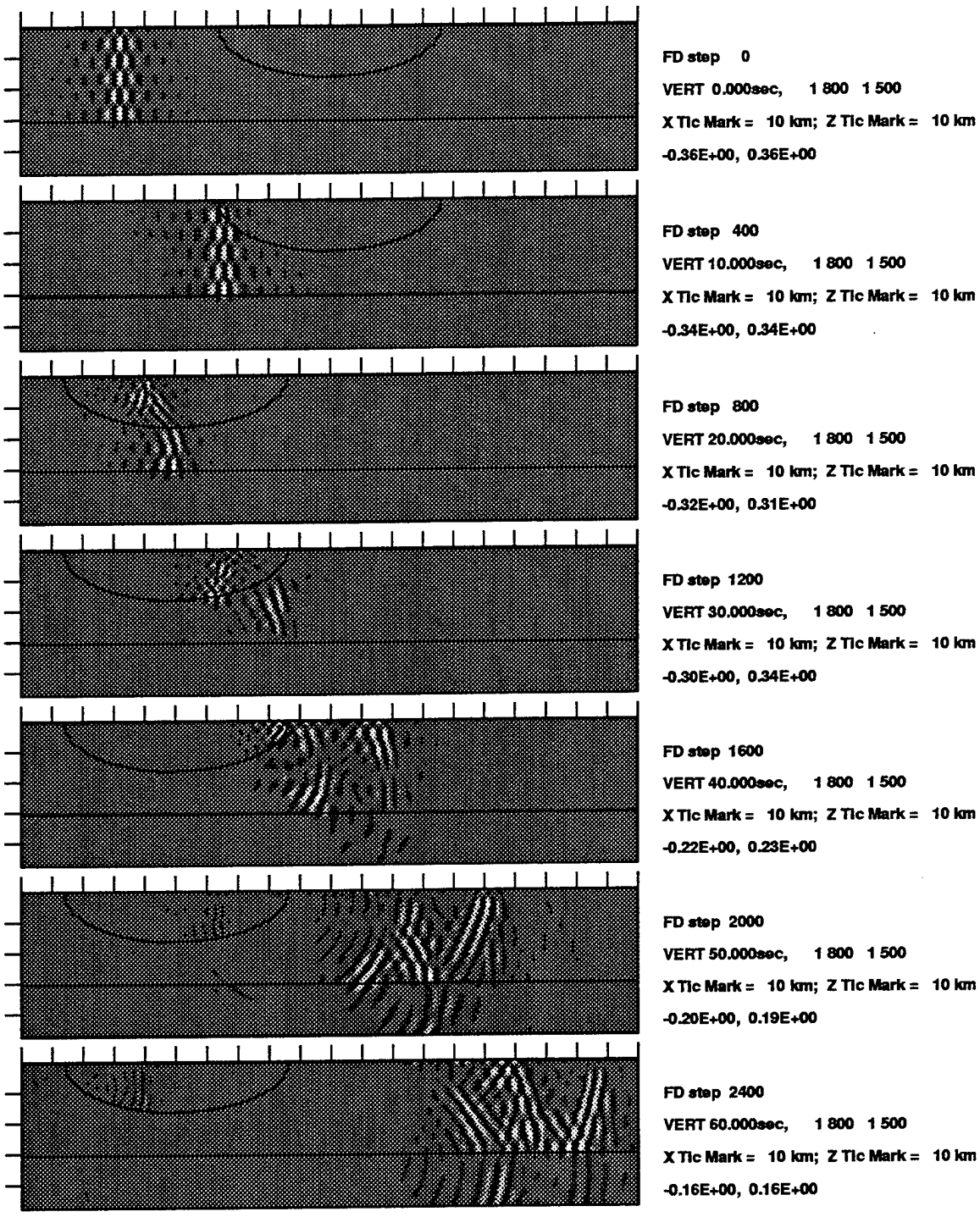

LFD Simulation of Lg Propagation: Model 0Da

Figure 23. Same as Figure 21 except for an elliptical basin. The results are very similar to those of model 0D. Thus the details of the basin shape appear to be not that important.

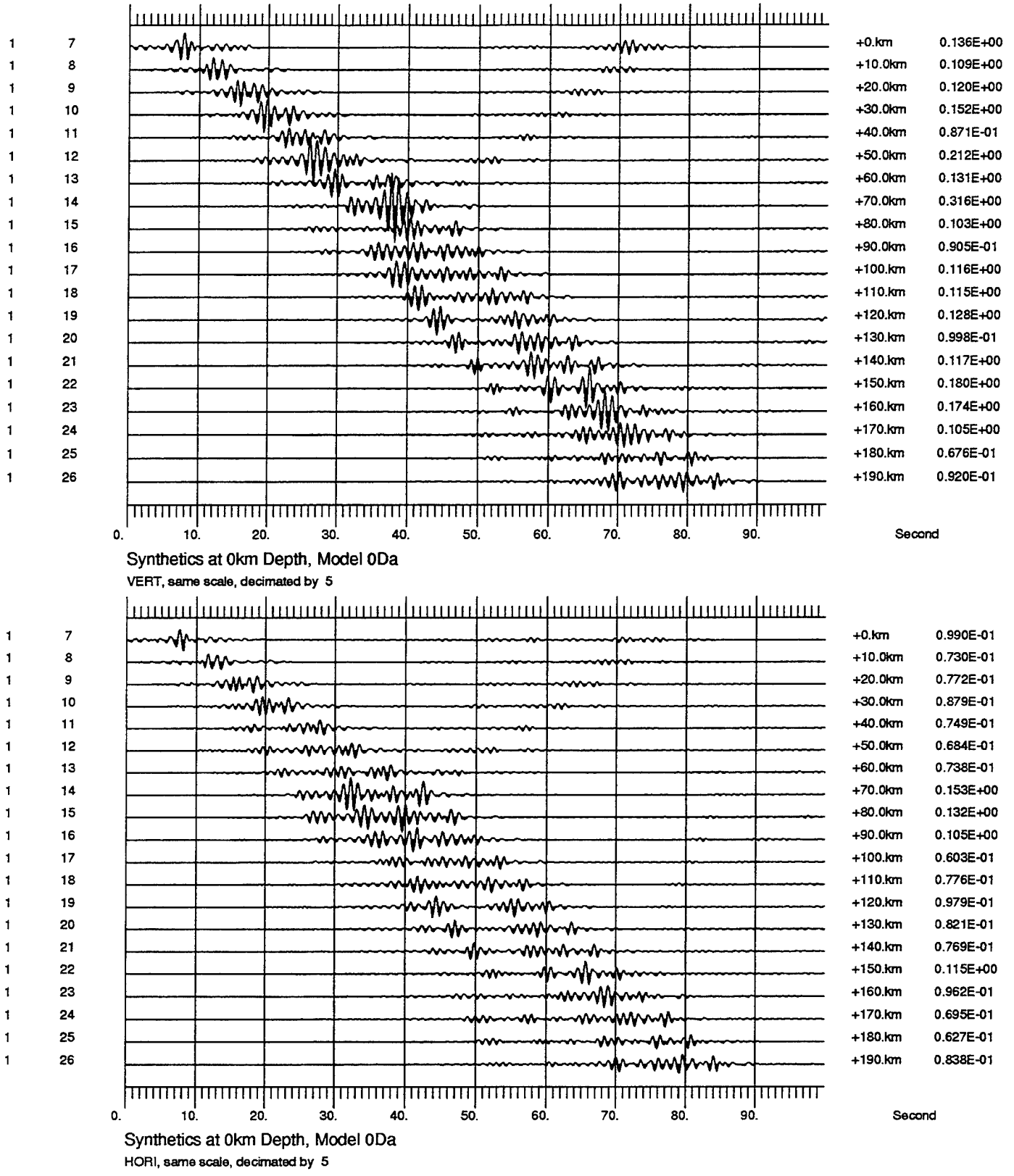

Figure 24. Similar to Figure 22 except for an elliptical basin. Although the results are very similar to those of model 0D, the blockage of the "on-time L_g" is more apparent. Also note the strong backscattering at the terminating edge of the basin.

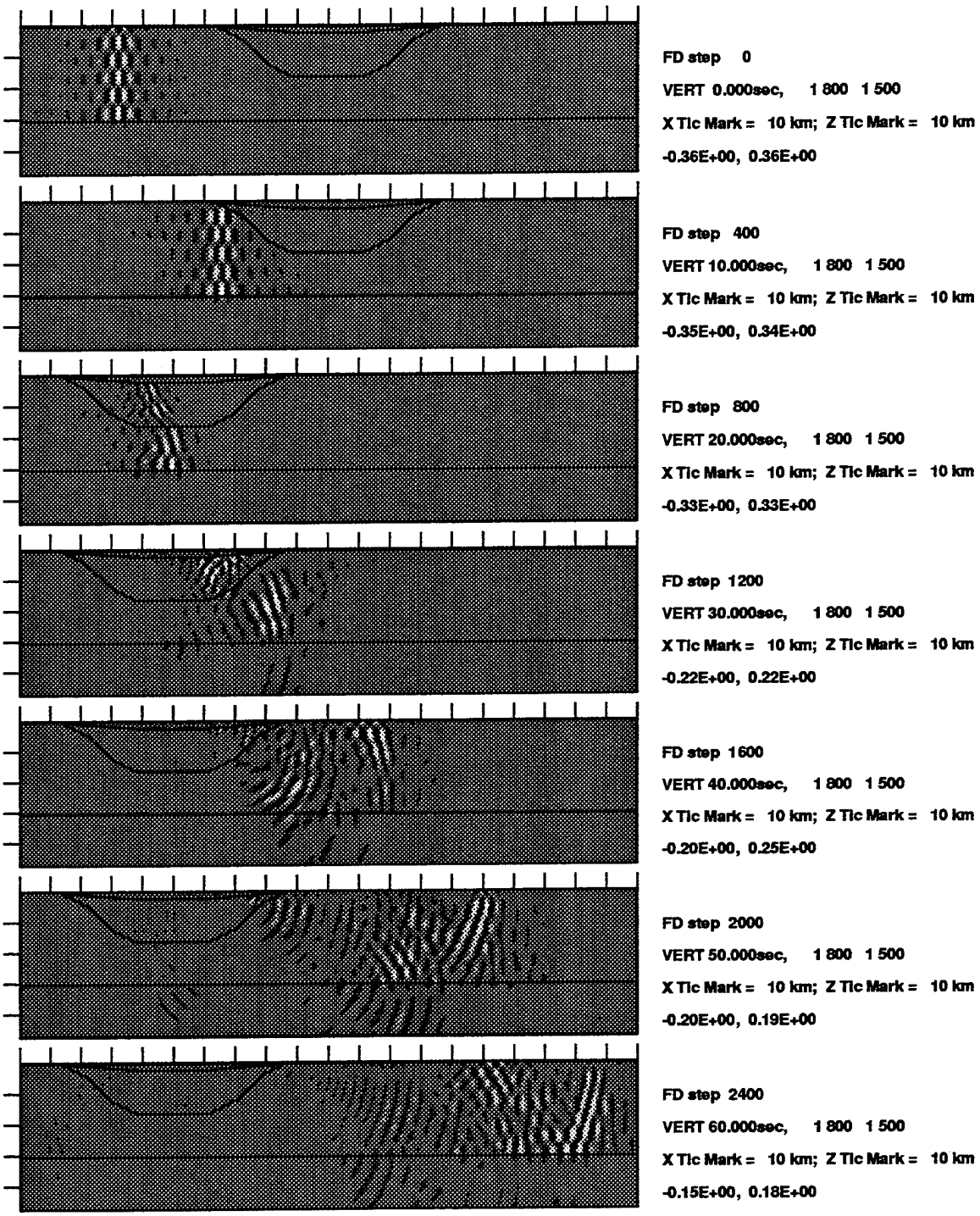

LFD Simulation of Lg Propagation: Model 0Db

Figure 25. The vertical-component snapshots of L_g wave propagation in the basin model 0Db. As in models 0D and 0Da, the bodywave coupling occurs at the pinched end of the basin where part of the energy that traverses the basin starts to leak out (at 40 and 50 seconds). This suggests that even in a model with no lateral variation in the Moho, the lateral structural heterogeneity in the uppermost crust still can produce mantle phases through scattering. The pinched edge is essential in this mechanism.

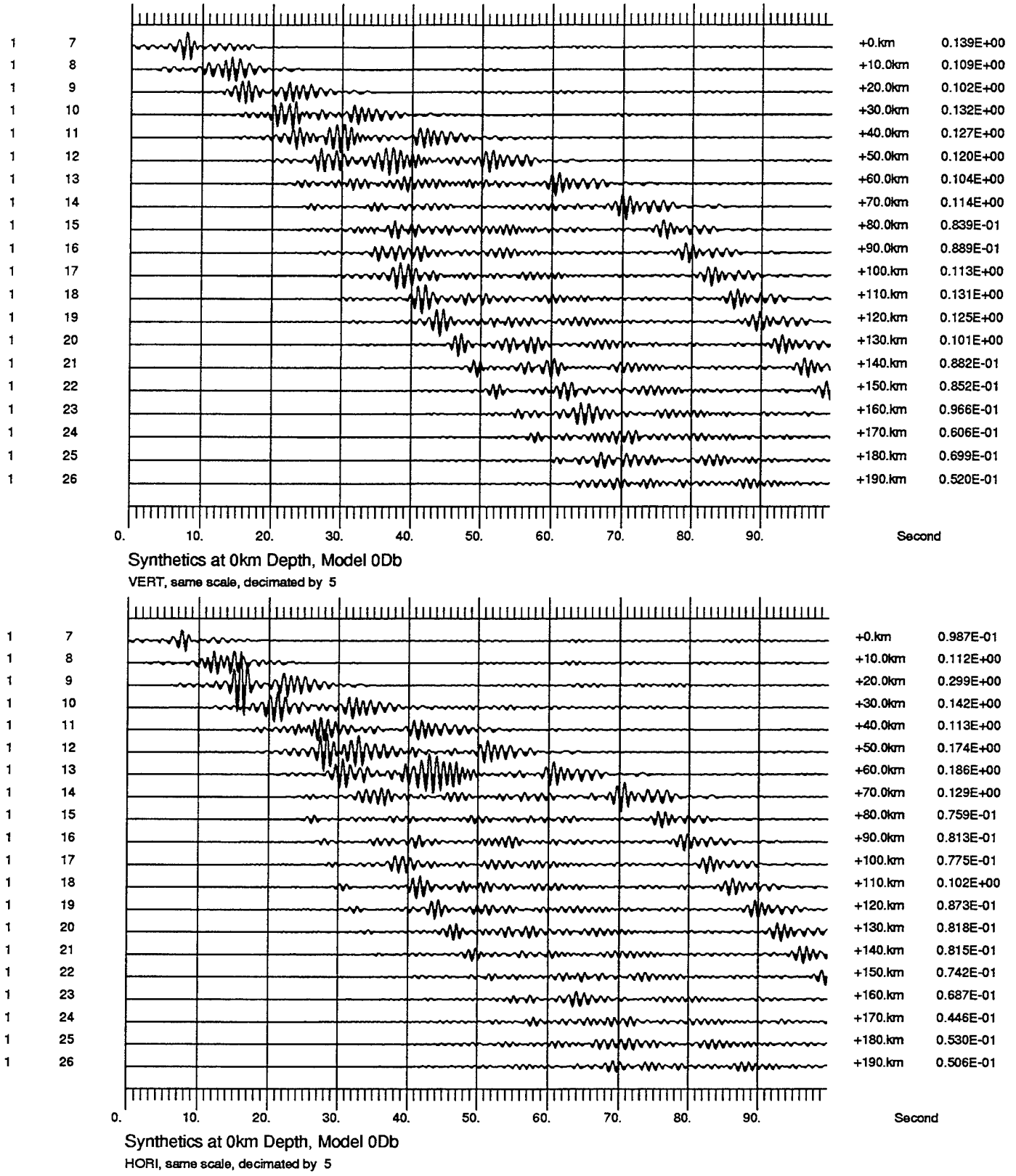

Figure 26. Similar to Figure 22 except that a thin, slow sedimentary layer is added. Both the R_g phase and the "late L_g" become prominent in this case. The "on-time L_g" wave is weakened and only certain surface sensors at the right locations can observe it.

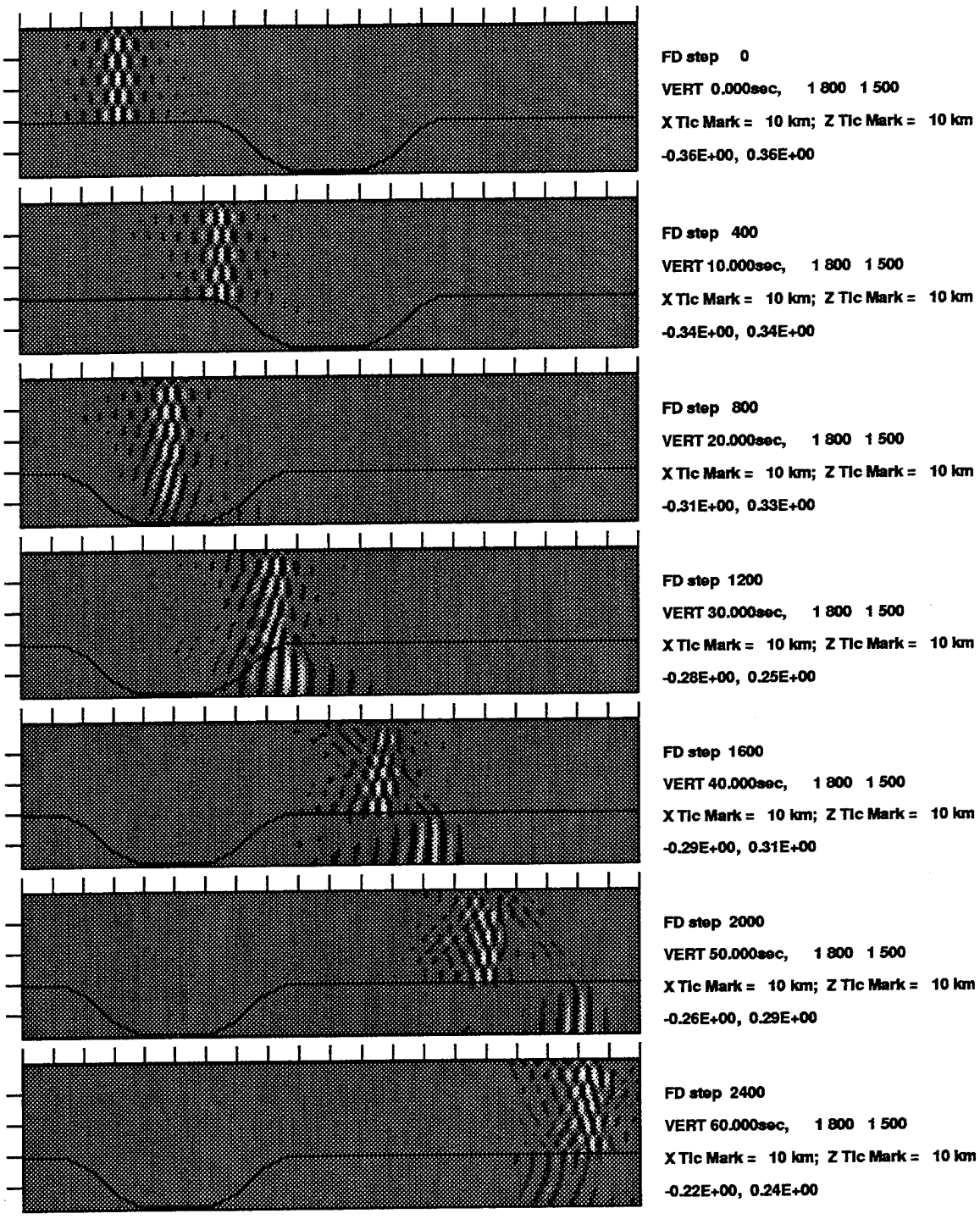

LFD Simulation of Lg Propagation: Model 0E

Figure 27. The vertical-component snapshots of L_g wave propagation in model 0E with a thickened crust. A very strong L_g-to-S_n conversion occurs along the ascending interface (see, 30, 40, and 50 seconds). Horizontal-component snapshots (not shown) indicate that some focusing of energy occurs at the corner where the Moho turns flat. This corner becomes a secondary point source, radiating upgoing body waves. Sensors right above this corner would detect a prominent arrival due to a nearly vertical incidence of shear waves (see traces No. 16 and 17 of Figure 28).

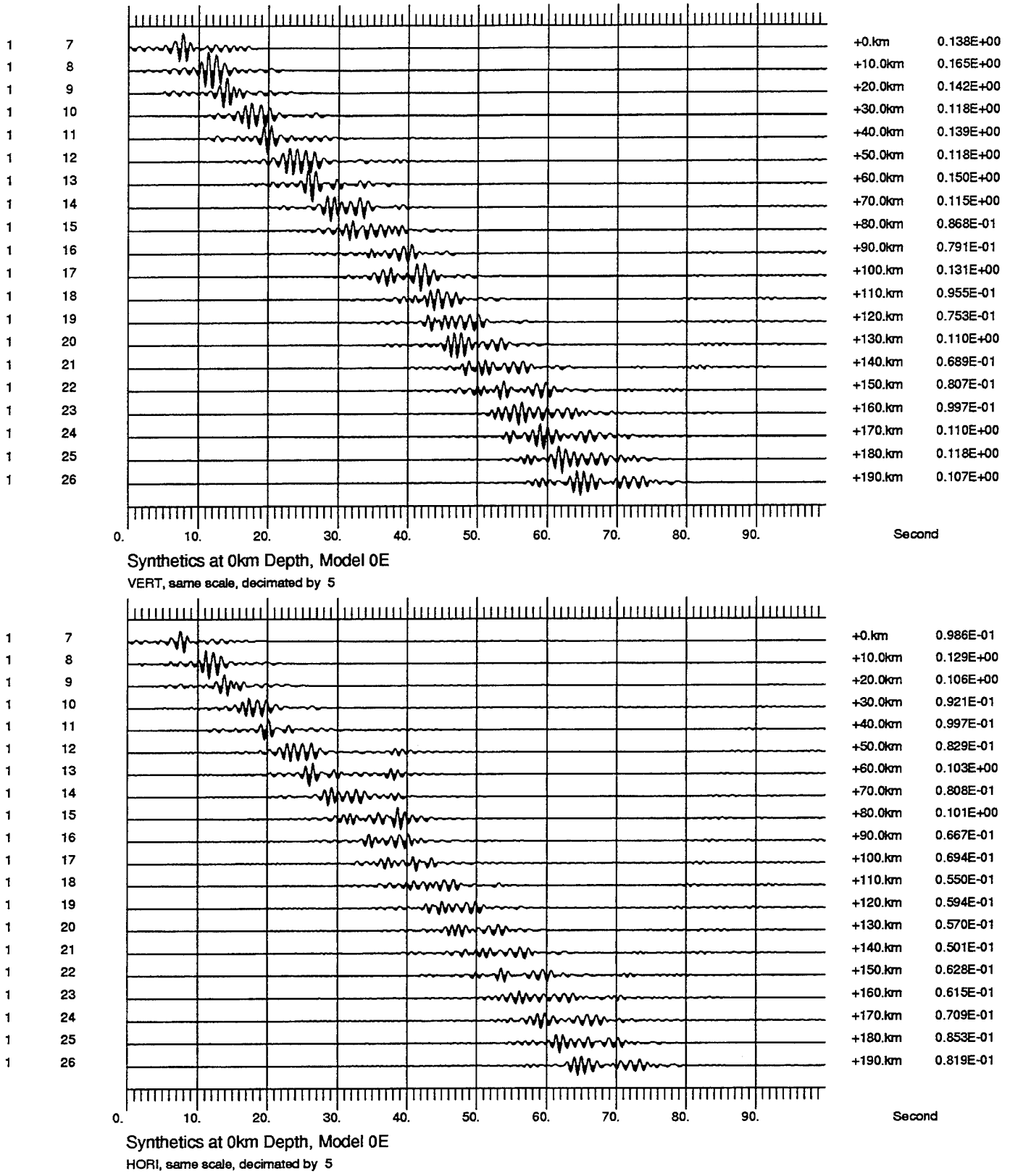

Figure 28. Seismic sections of model 0E, which has a thickened crust. The corner where the Moho turns flat is a secondary point source radiating upgoing body waves. The prominent arrival on traces 16 and 17 has a very large apparent velocity, due to a nearly normal incidence. The "on-time L_g" is only partially blocked.

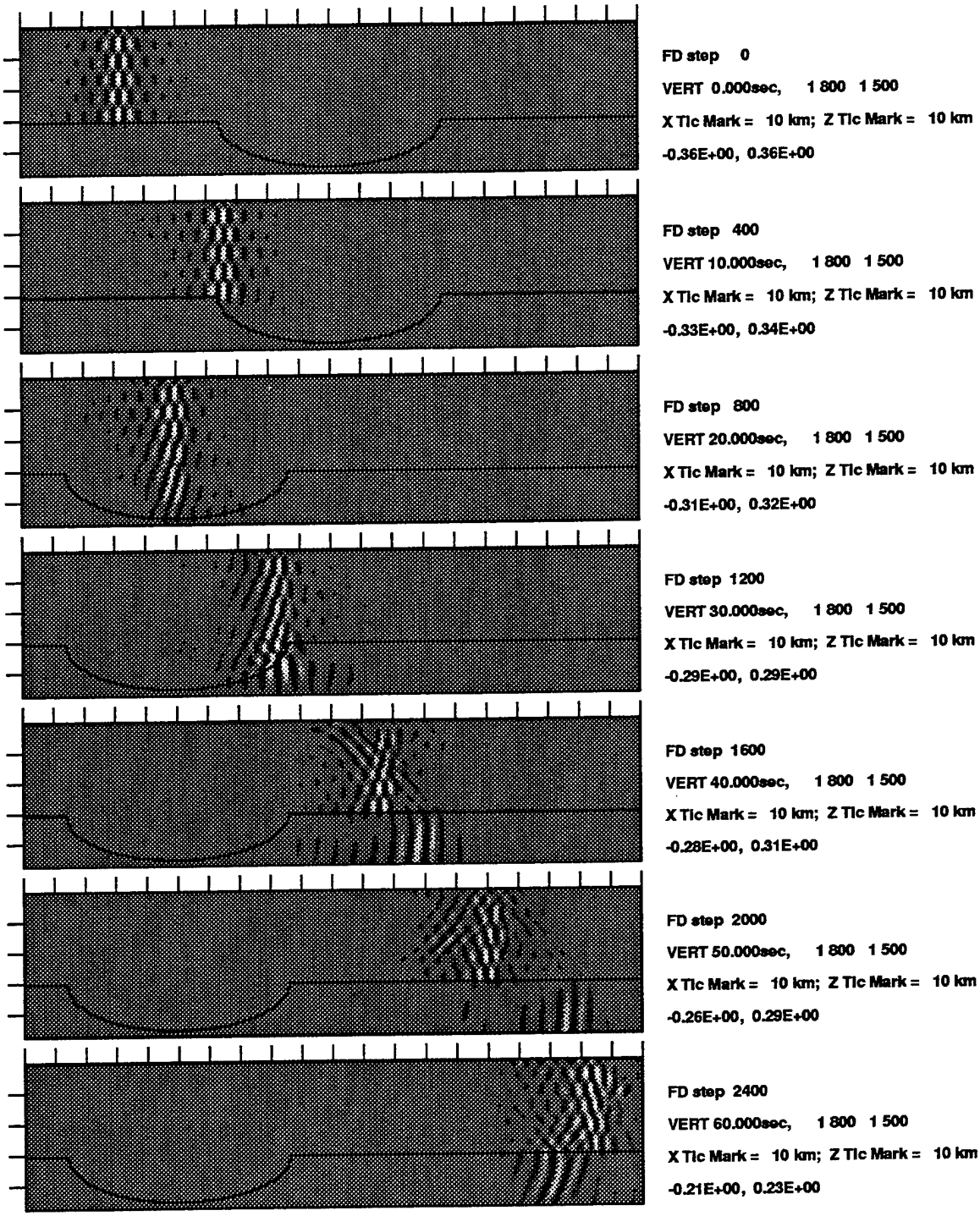

LFD Simulation of Lg Propagation: Model 0Ea

Figure 29. The vertical-component snapshots of L_g wave propagation in model 0Ea with a thickened crust.

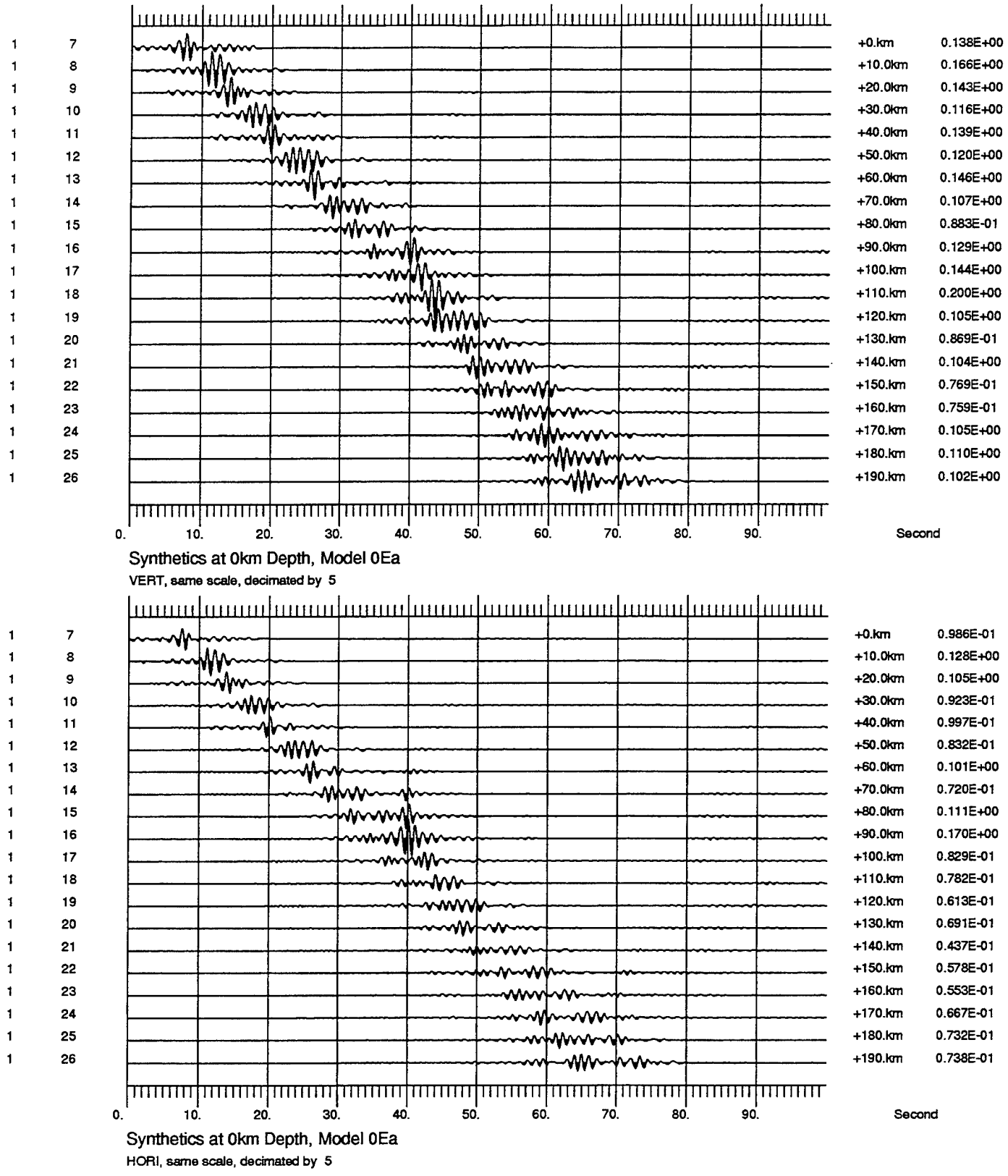

Figure 30. Seismic sections of model 0Ea, which has a thickened crust. The corner where the Moho turns flat is a secondary point source radiating upgoing body waves. The prominent arrival on traces 16 and 17 has a very large apparent velocity, due to a nearly normal incidence. The "on-time L_g" is only partially blocked.

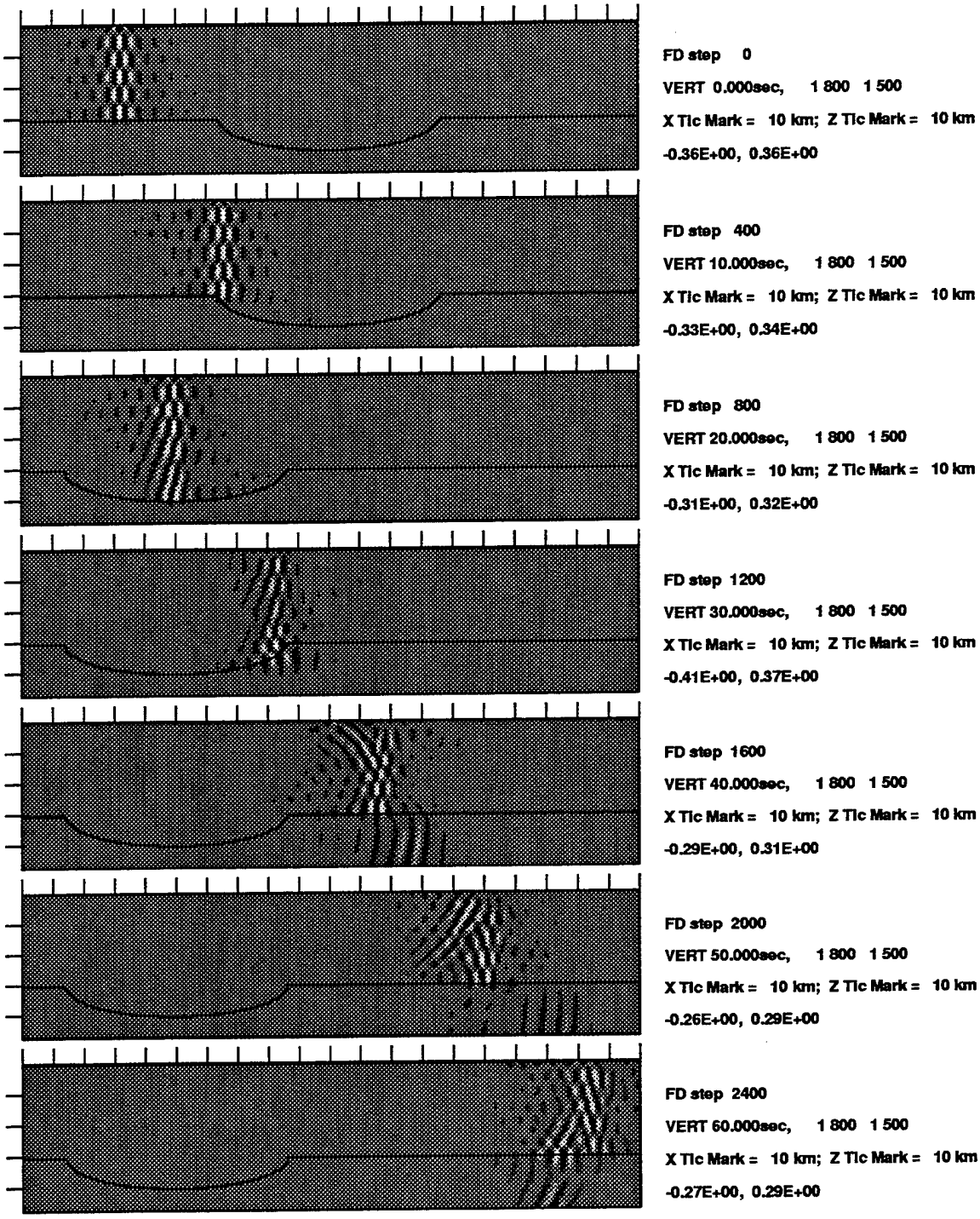

LFD Simulation of Lg Propagation: Model 0Eb

Figure 31. The vertical-component snapshots of L_g wave propagation in model 0Eb, with a thickened crust.

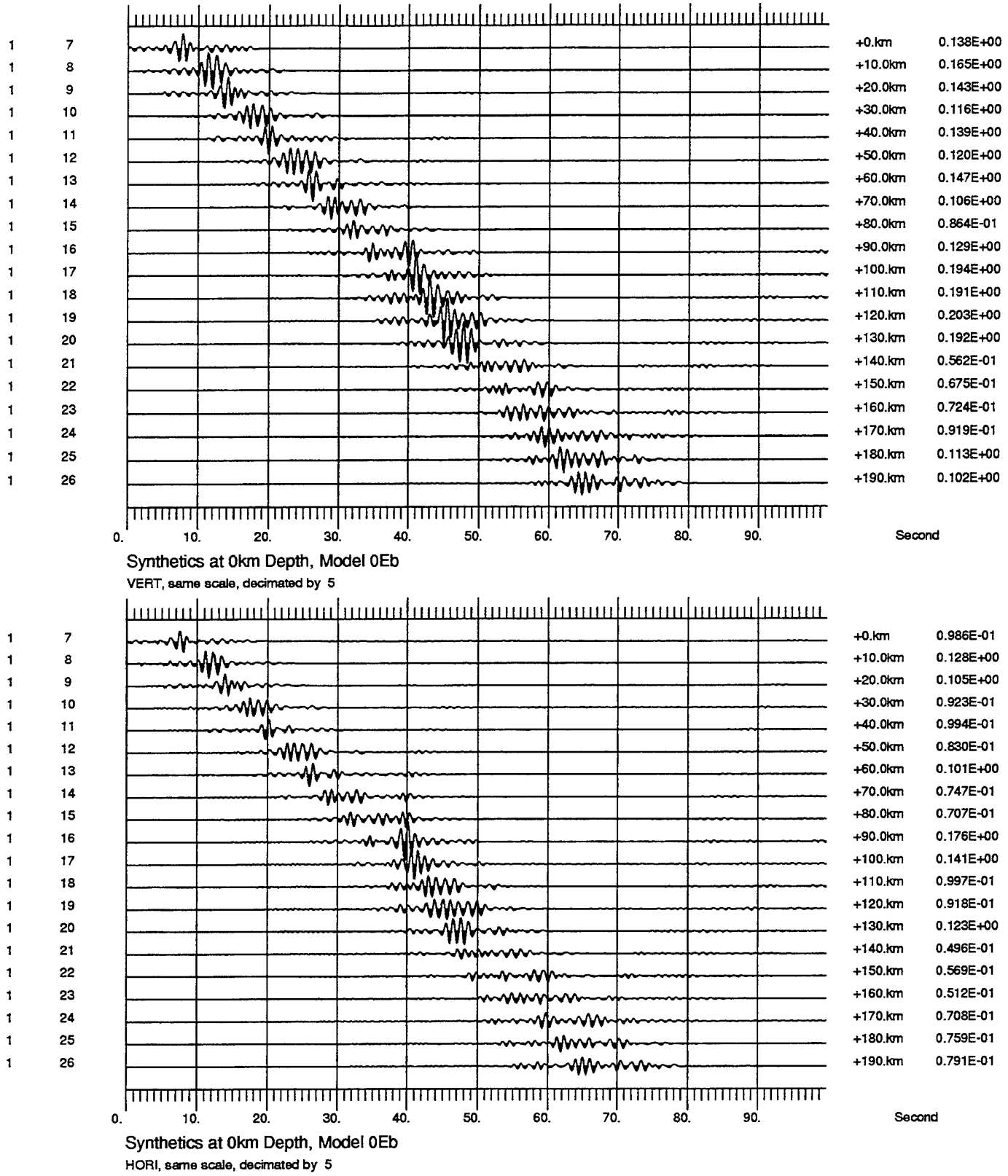

Figure 32. Seismic sections of model 0Eb, which has a thickened crust. The corner where the Moho turns flat is a secondary point source radiating upgoing body waves. The prominent arrival on traces 16 and 17 has a very large apparent velocity, due to a nearly normal incidence. The "on-time L_g" is only partially blocked.

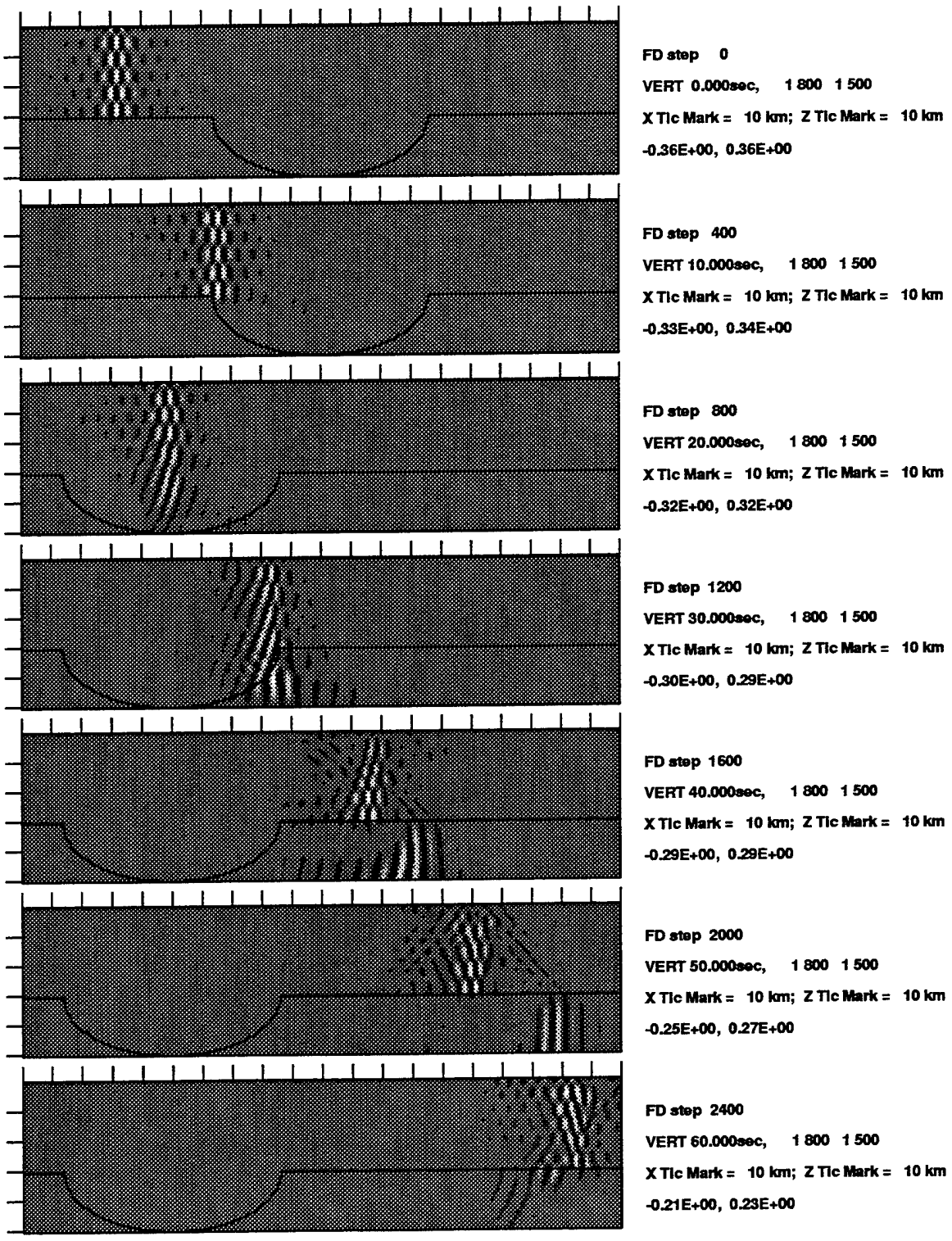

LFD Simulation of Lg Propagation: Model 0Ec

Figure 33. The vertical-component snapshots of L_g wave propagation in model 0Ec, with a thickened crust.

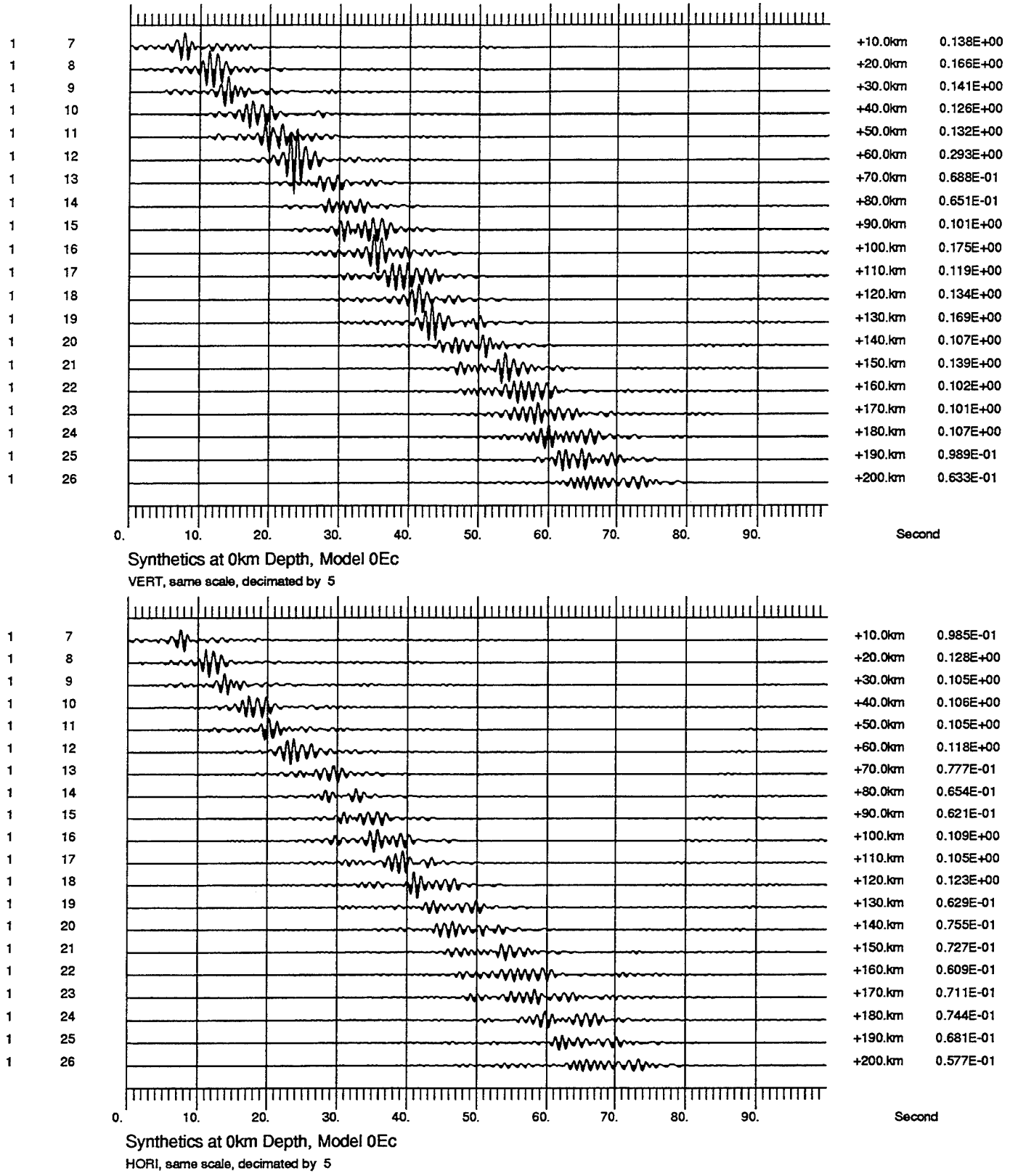

Figure 34. Seismic sections of model 0Ec, which has a thickened crust. The "on-time L_g" is only partially blocked.

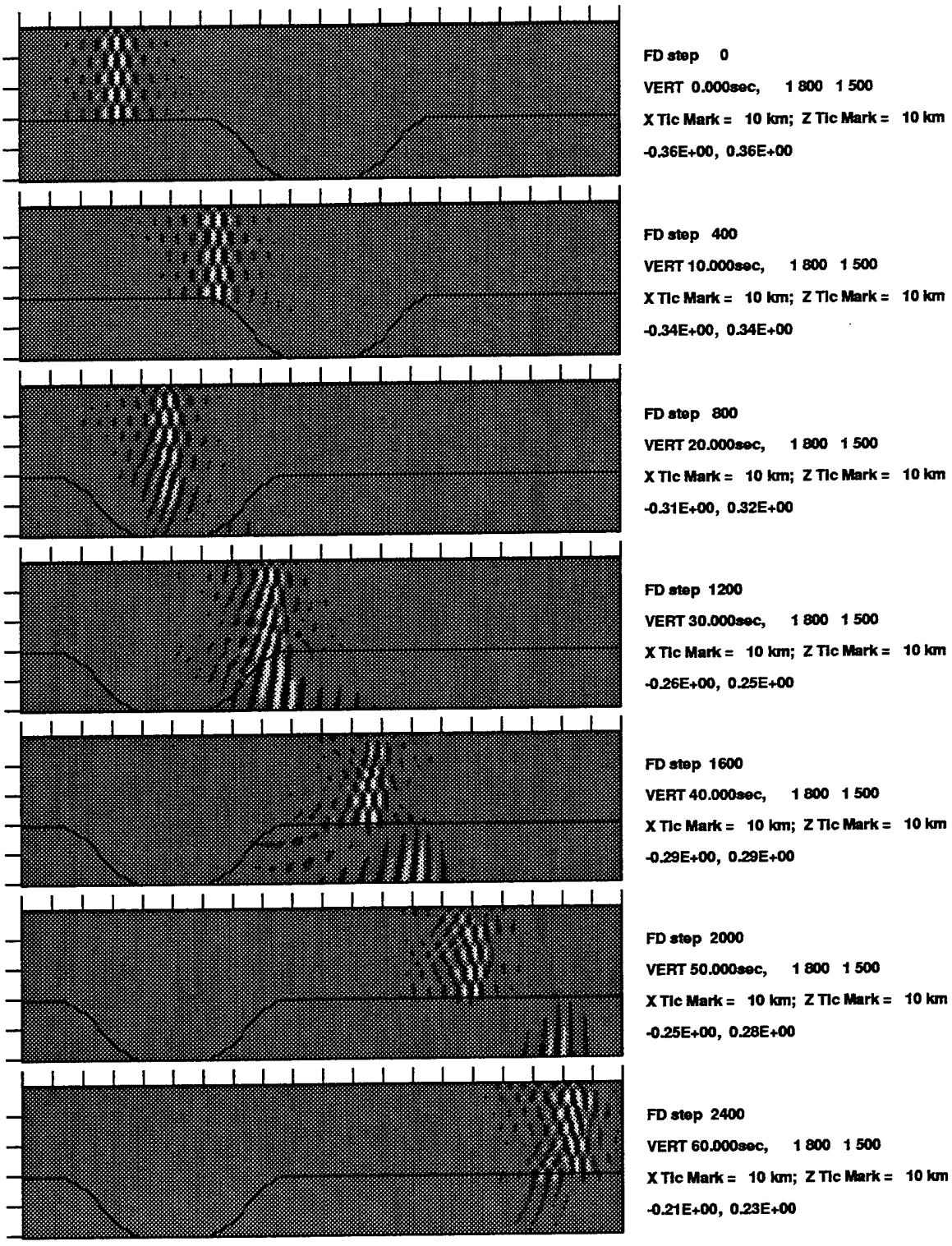

LFD Simulation of Lg Propagation: Model 0Ed

Figure 35. The vertical-component snapshots of L_g wave propagation in model 0Ed, with a thickened crust.

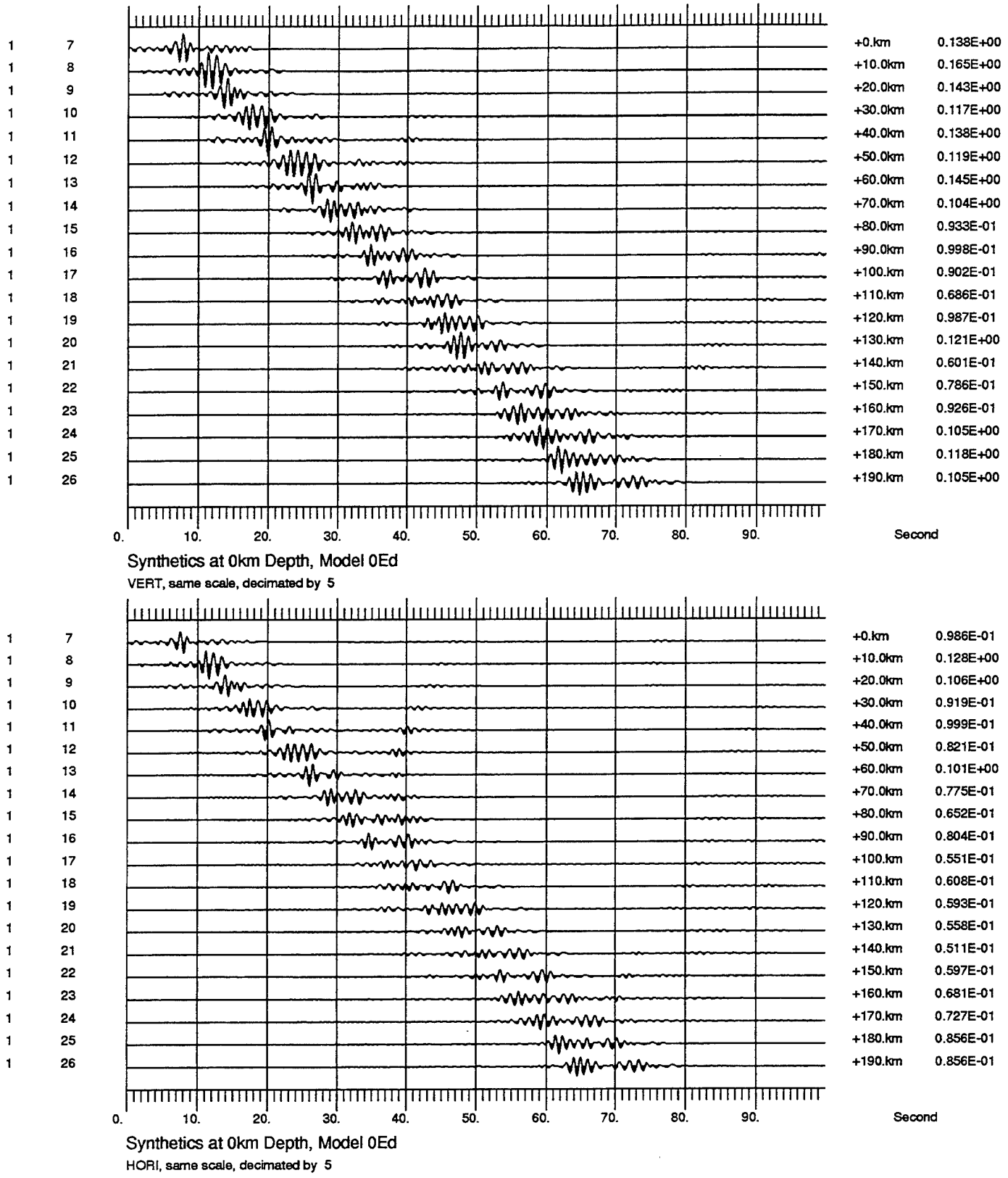

Figure 36. Seismic sections of model 0Ed, which has a thickened crust. The corner where the Moho turns flat is a secondary point source radiating upgoing body waves. The prominent arrival on traces 16 and 17 has a very large apparent velocity, due to a nearly normal incidence. The "on-time L_g" is only partially blocked.

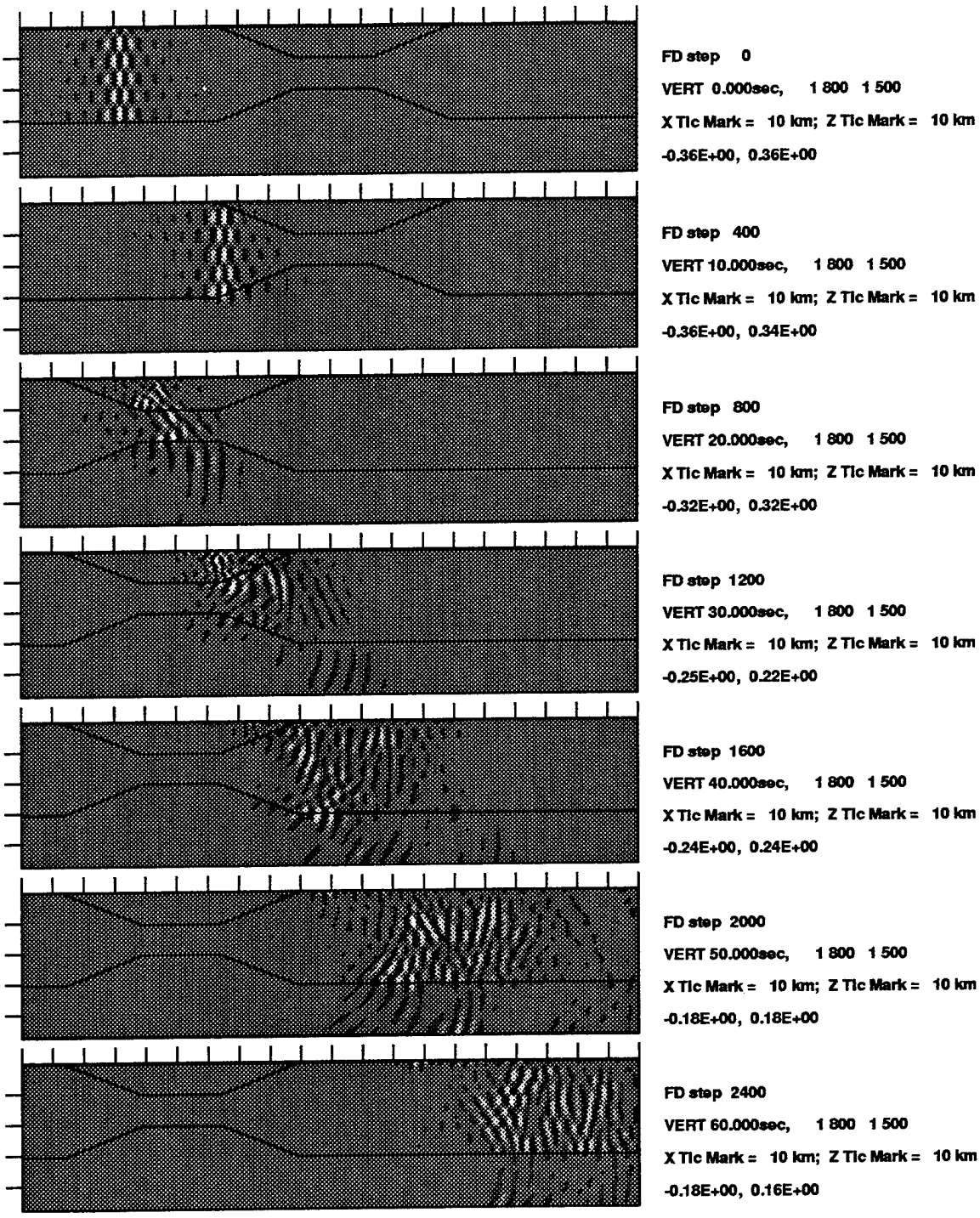

LFD Simulation of Lg Propagation: Model 0F

Figure 37. The vertical-component snapshots of L_g wave propagation in model 0F, which has both a sedimentary basin and a Moho uplift. The Moho uplift causes a strong S_n conversion (see, at 20 seconds). The pinched end of the basin radiates body waves outward, and some of those rays leak into deeper mantle.

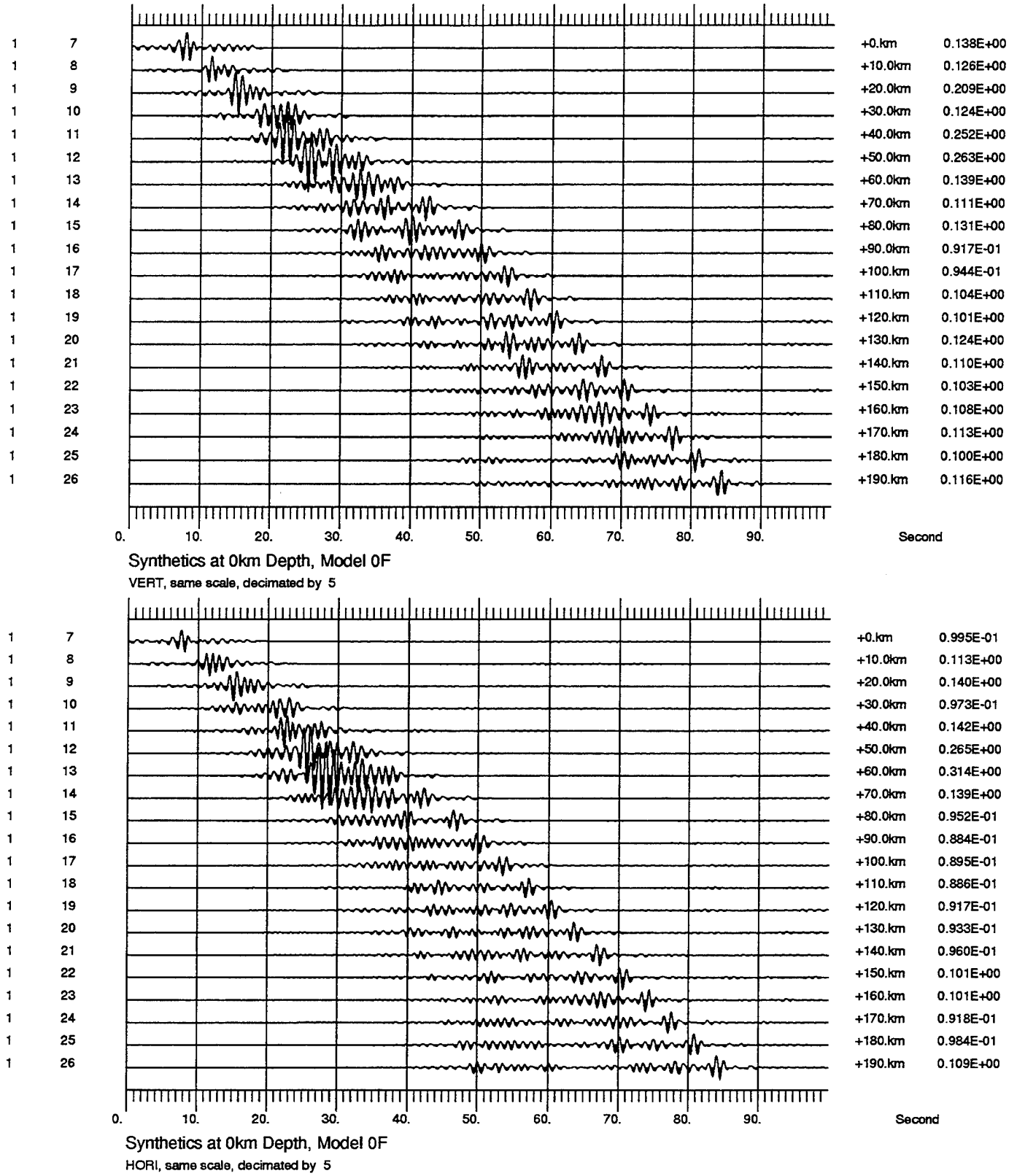

Figure 38. Seismic sections of model 0F, which has a Moho uplift and a sedimentary basin.

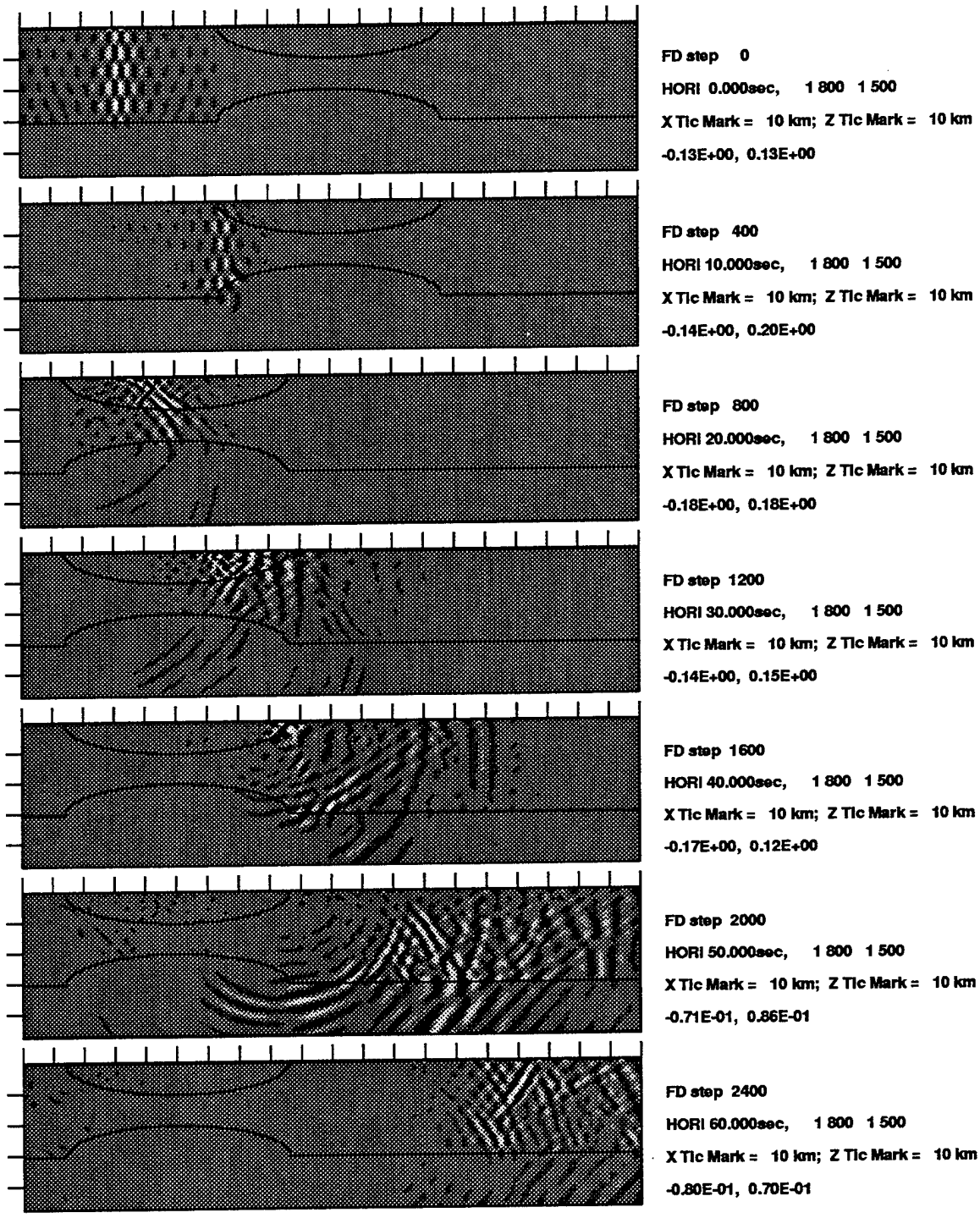

LFD Simulation of Lg Propagation: Model 0Fa

Figure 39. The horizontal-component snapshots of L_g wave propagation in model 0Fa, which has both a sedimentary basin and a Moho uplift. Observations similar to those with the model 0F can be made. The pinched end of the basin radiates body waves outward, and some of those rays leak into deeper mantle (see, at 50 seconds). Some direct P waves are also present (see, at 40 seconds).

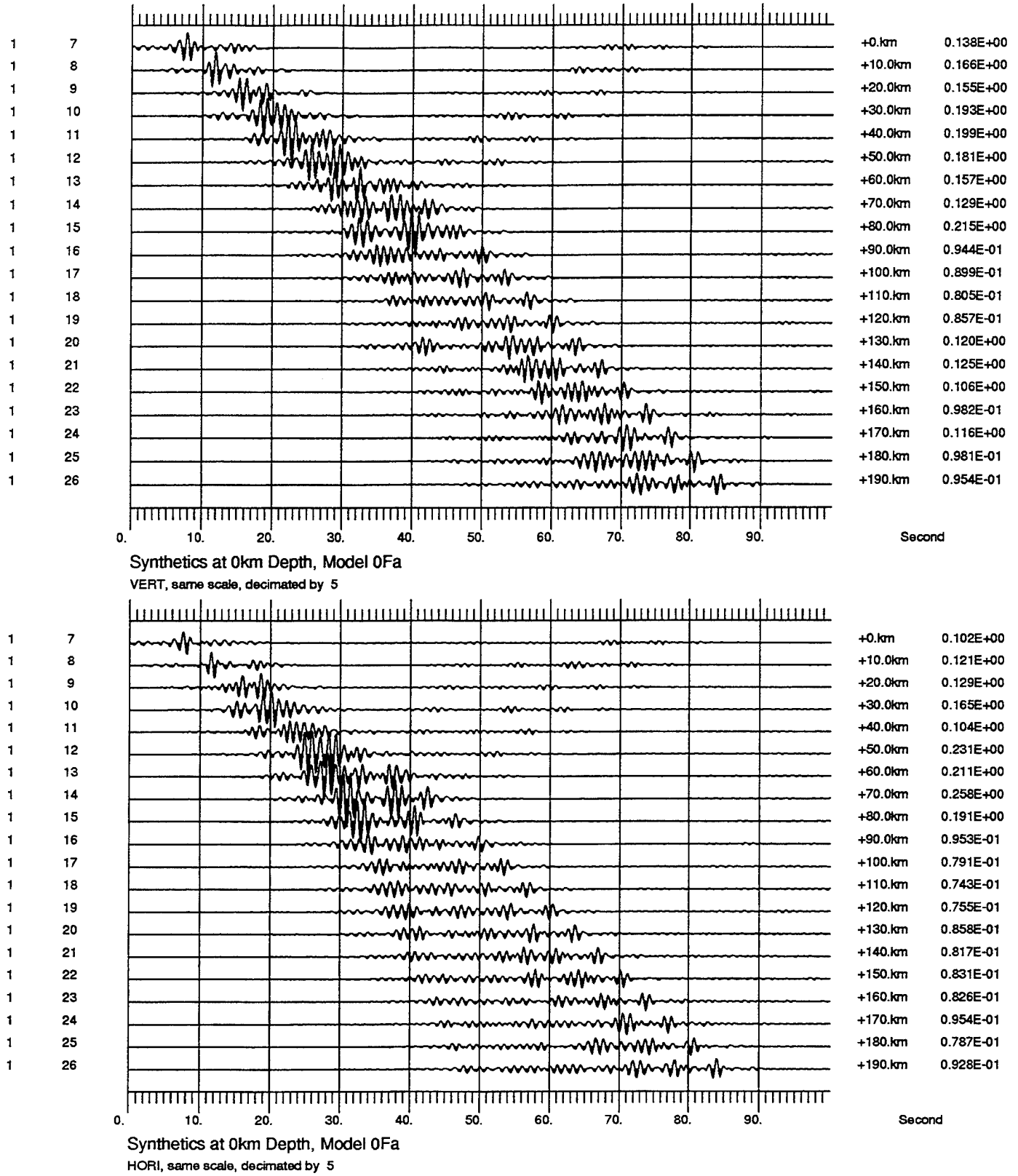

Figure 40. Seismic sections of model 0Fa, which has a Moho uplift and a sedimentary basin. Partial blockage of "on-time L_g" is observable. Much of the energy is delayed because of the sedimentary basin. Direct P waves radiated from the basin's terminating edge can be seen on the horizontal components.

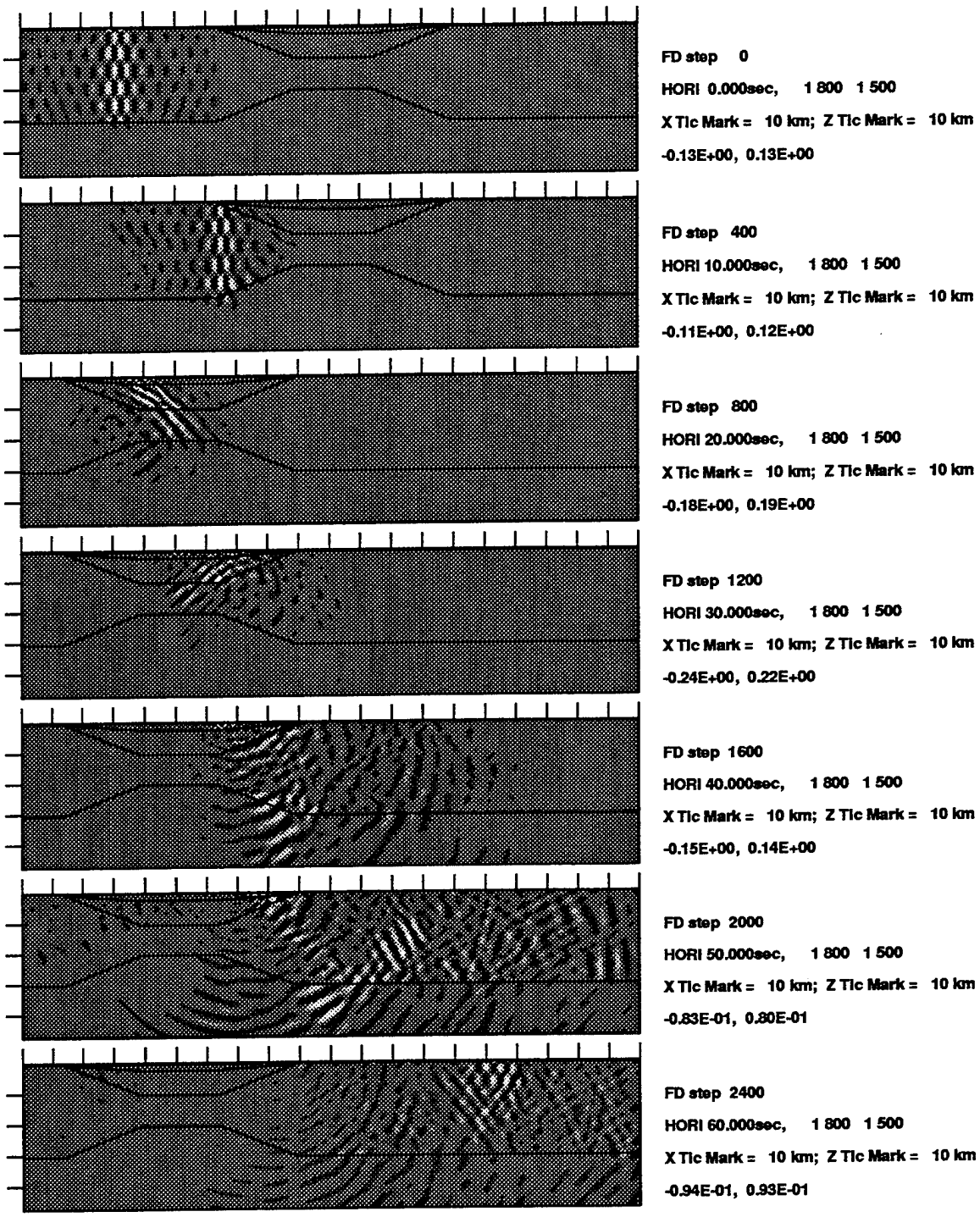

LFD Simulation of Lg Propagation: Model 0Fb

Figure 41. The horizontal-component snapshots of L_g wave propagation in model 0Fb, which has two sedimentary layers and a Moho uplift. Observations similar to those with the models 0F and 0Fa can be made: the basin edge acts like a secondary point source. A prominent SmS-mode of propagation is quite clear at 50 seconds. The visibility of this phase is distance-dependent.

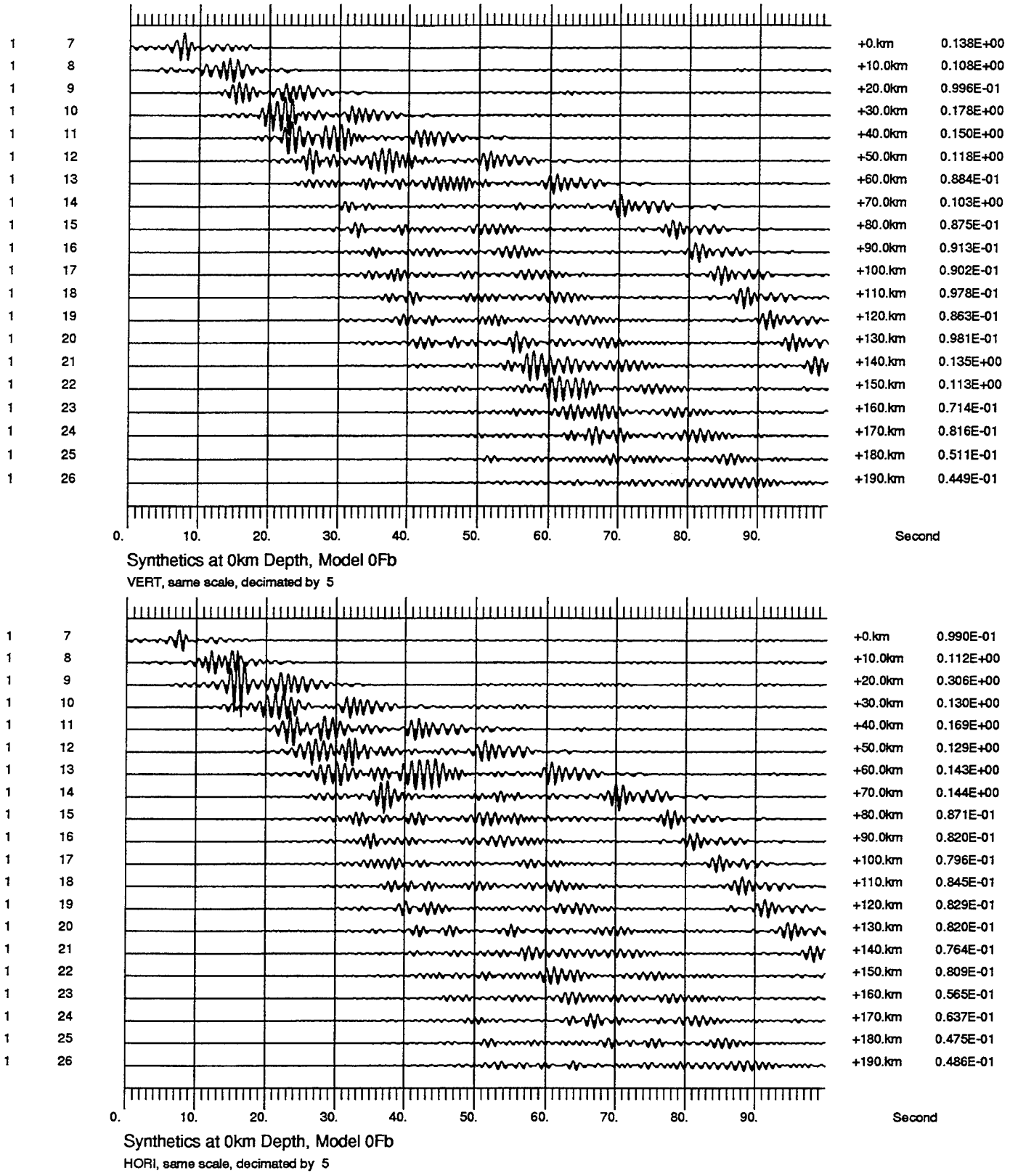

Figure 42. Seismic sections of model 0Fb, which has a Moho uplift and two sedimentary layers. "On-time L_g" is essentially blocked whereas two groups of "late L_g" waves as well as the further delayed R_g are present. The prominent phase arriving between 55 and 70 seconds on traces 20 through 24 is a SmS phase originated from the basin edge.

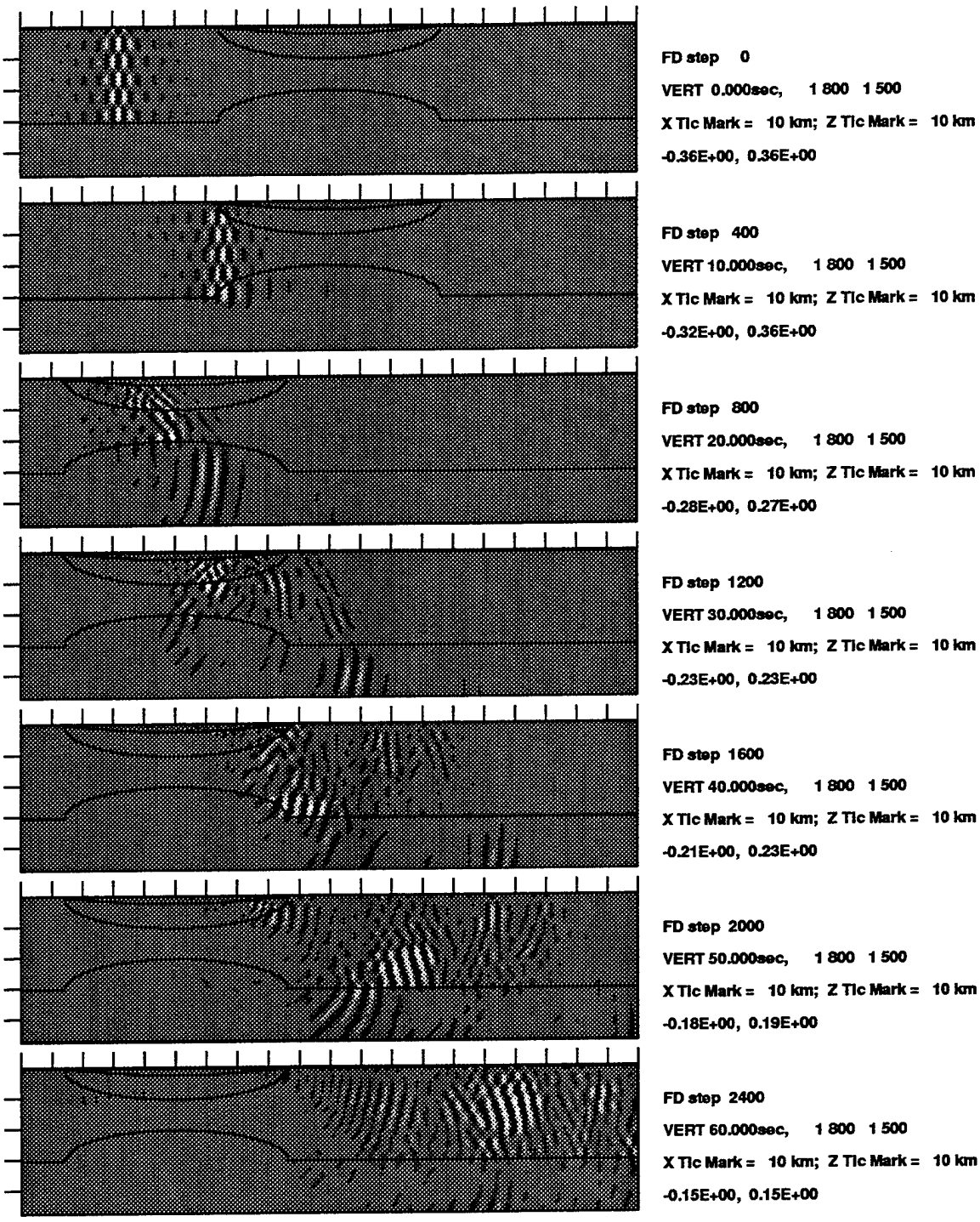

LFD Simulation of Lg Propagation: Model 0Fc

Figure 43. The vertical-component snapshots of L_g wave propagation in model 0Fc, which has two sedimentary layers and a Moho uplift. Observations similar to those with model 0Fb can be made: the basin edge acts like a secondary point source. A prominent SmS-mode of propagation is quite clear at 50 and 60 seconds. The visibility of this phase is distance-dependent, however.

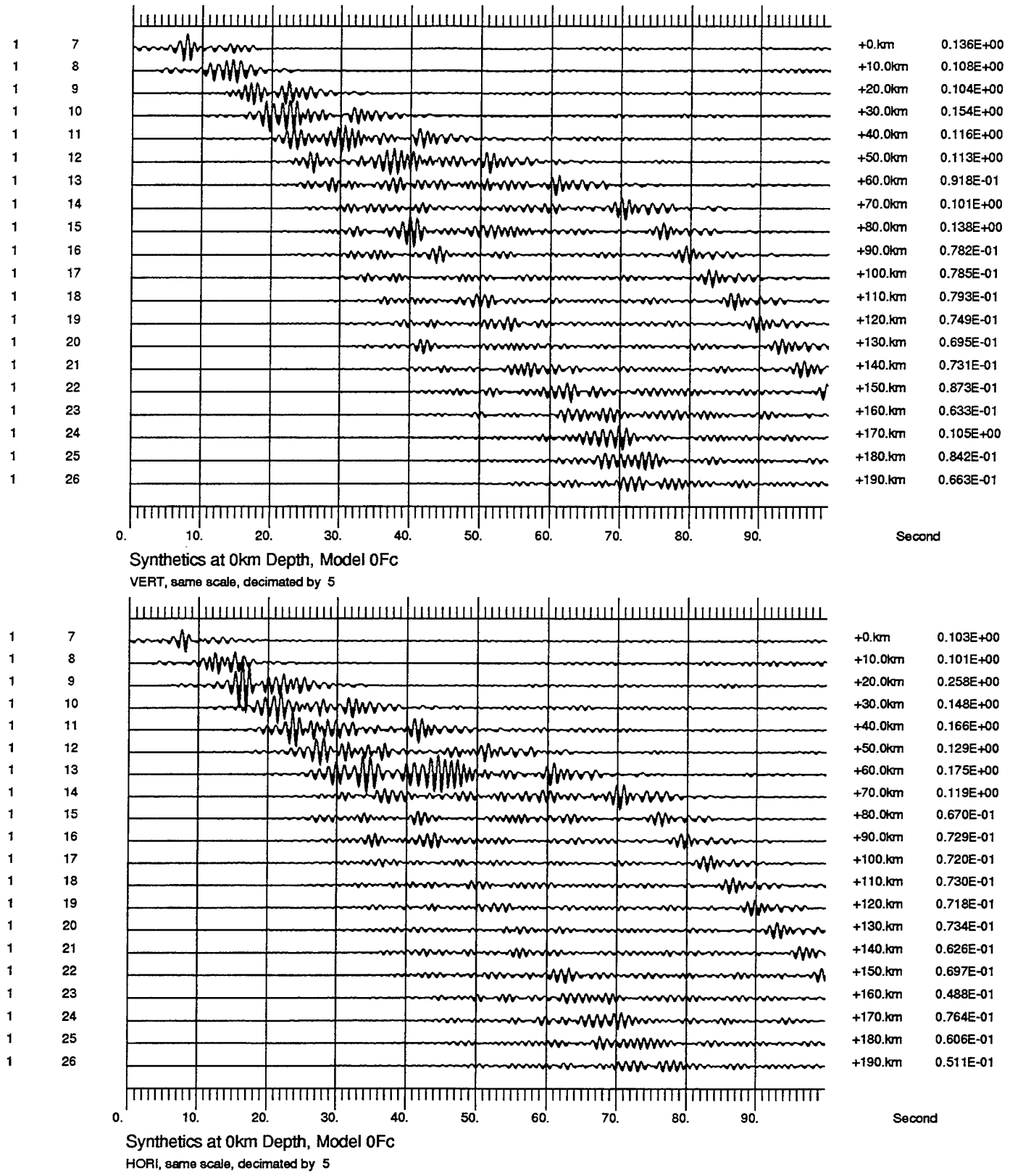

Figure 44. Seismic sections of model 0Fc, which has a Moho uplift and two sedimentary layers. The most prominent phase before R_g is the SmS radiated from the basin edge, which can be seen at certain receivers, depending on the distance (see traces No. 21 through 26).

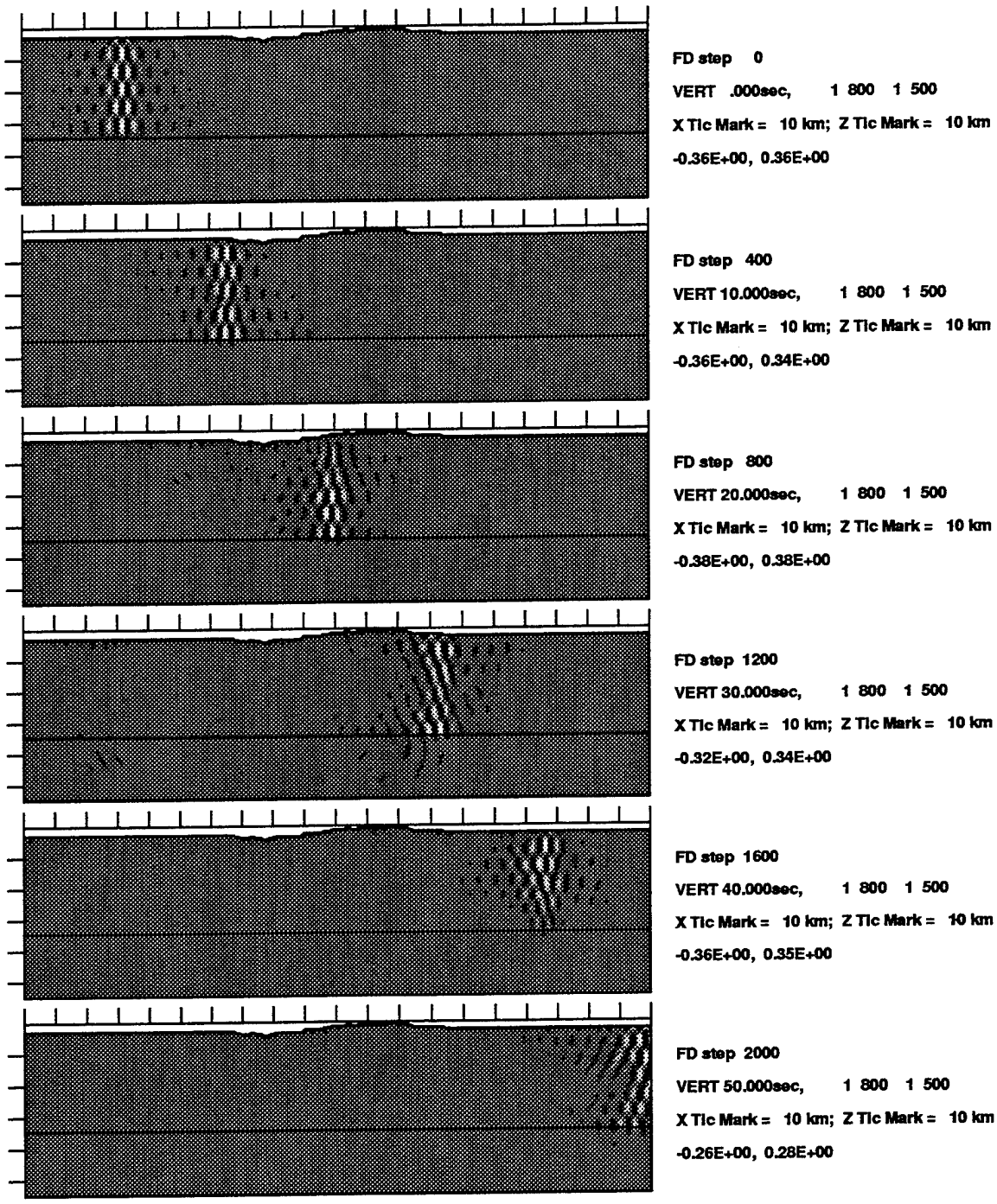

Figure 45. The vertical-component snapshots of L_g wave propagation of model 2, which has a flat Moho and a moderate free-surface topography. The L_g-to-S_n conversion is relatively weak. This is very different from the case of R_g where scattering by rough topography would cause very strong apparent attenuation.

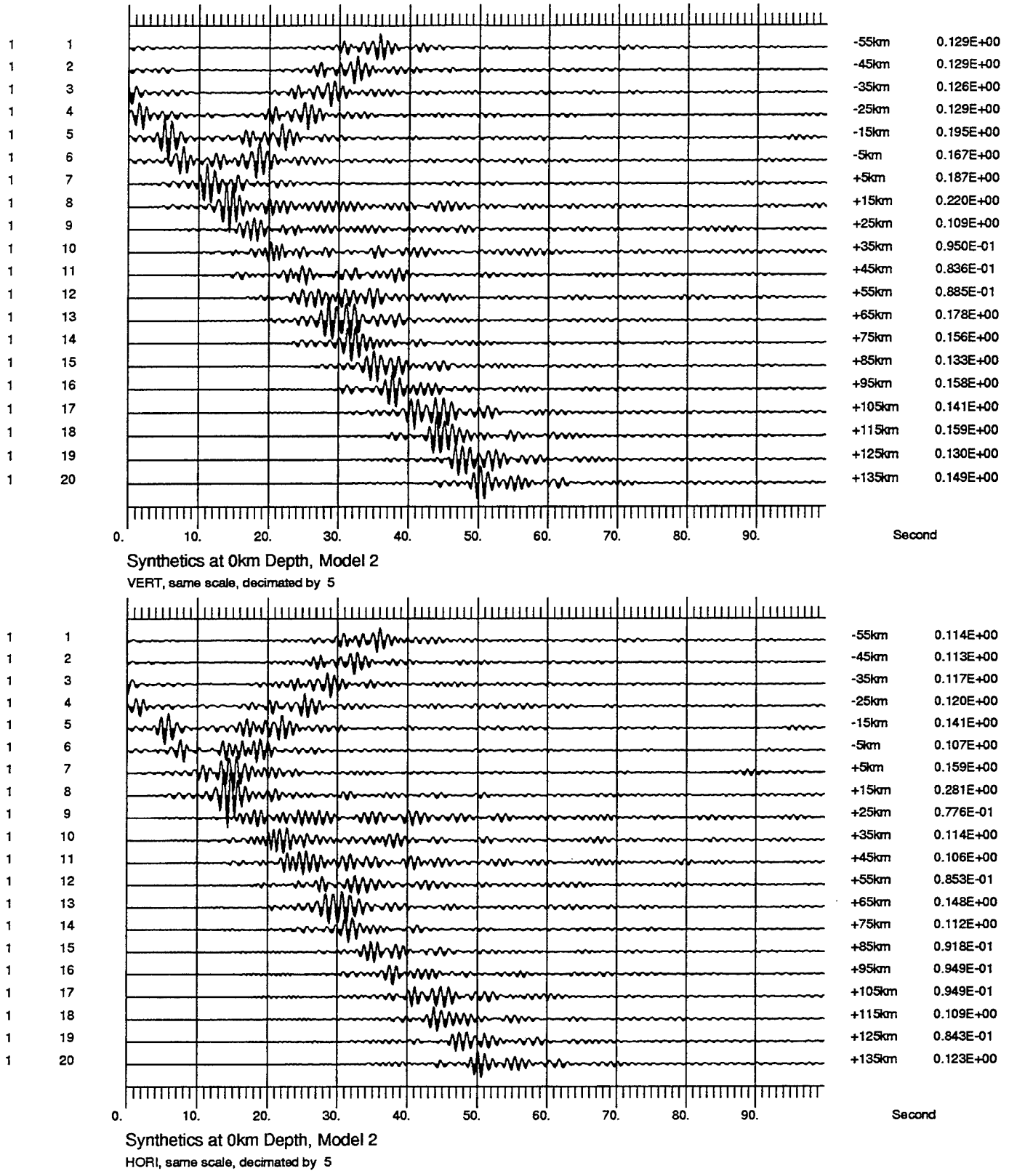

Figure 46. Seismic sections of model 2, which has a moderate free-surface topography. The scattering effects of topography on L_g are not as strong as those due to large-scale structural discontinuities.

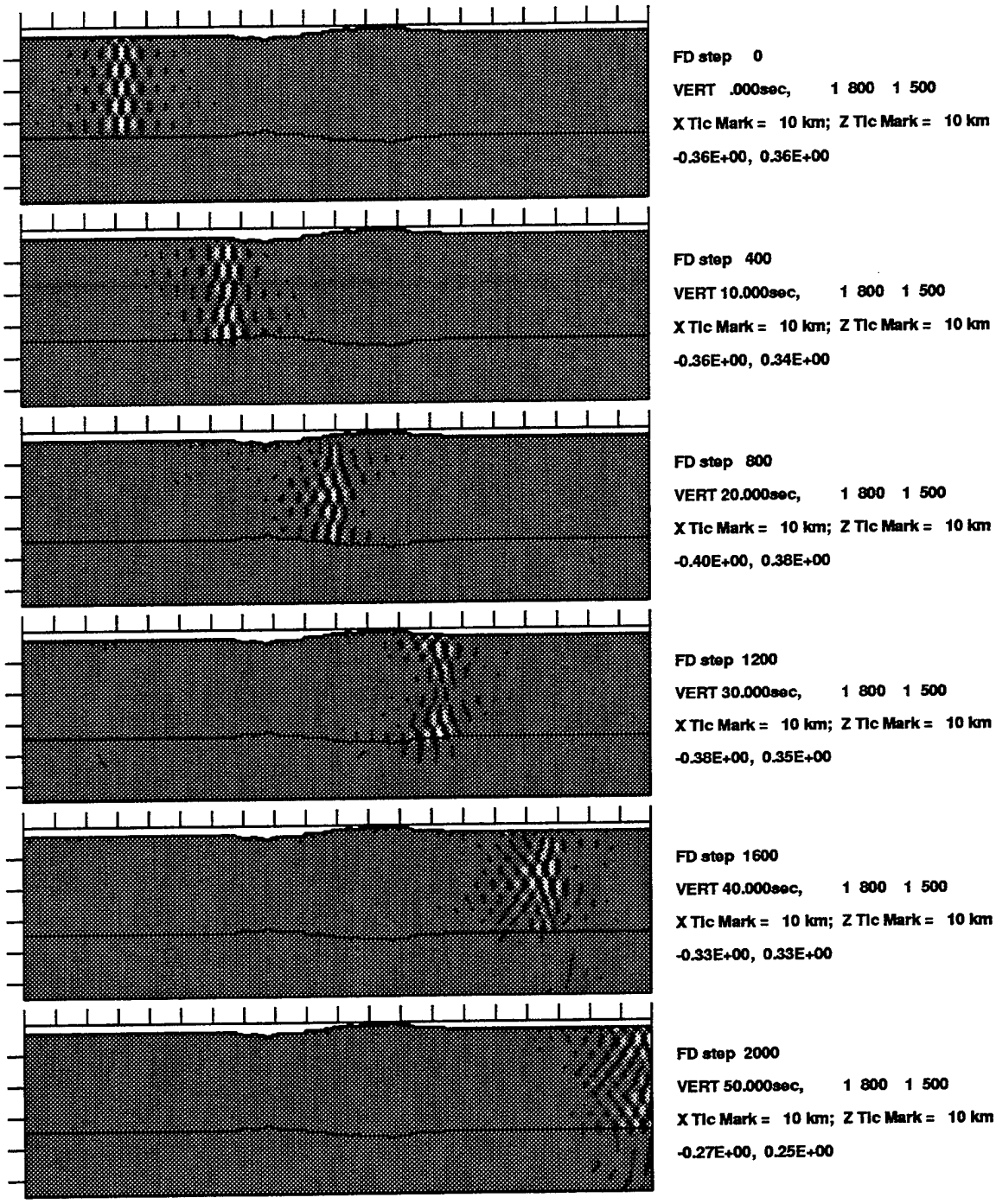

Figure 47. The vertical-component snapshots of L_g wave propagation of model 2a, in which the Moho is fully compensated. The elevation change of this topographic profile is relatively small compared to the thickness of the homogeneous crust, and hence the transmission of L_g is still fairly efficient.

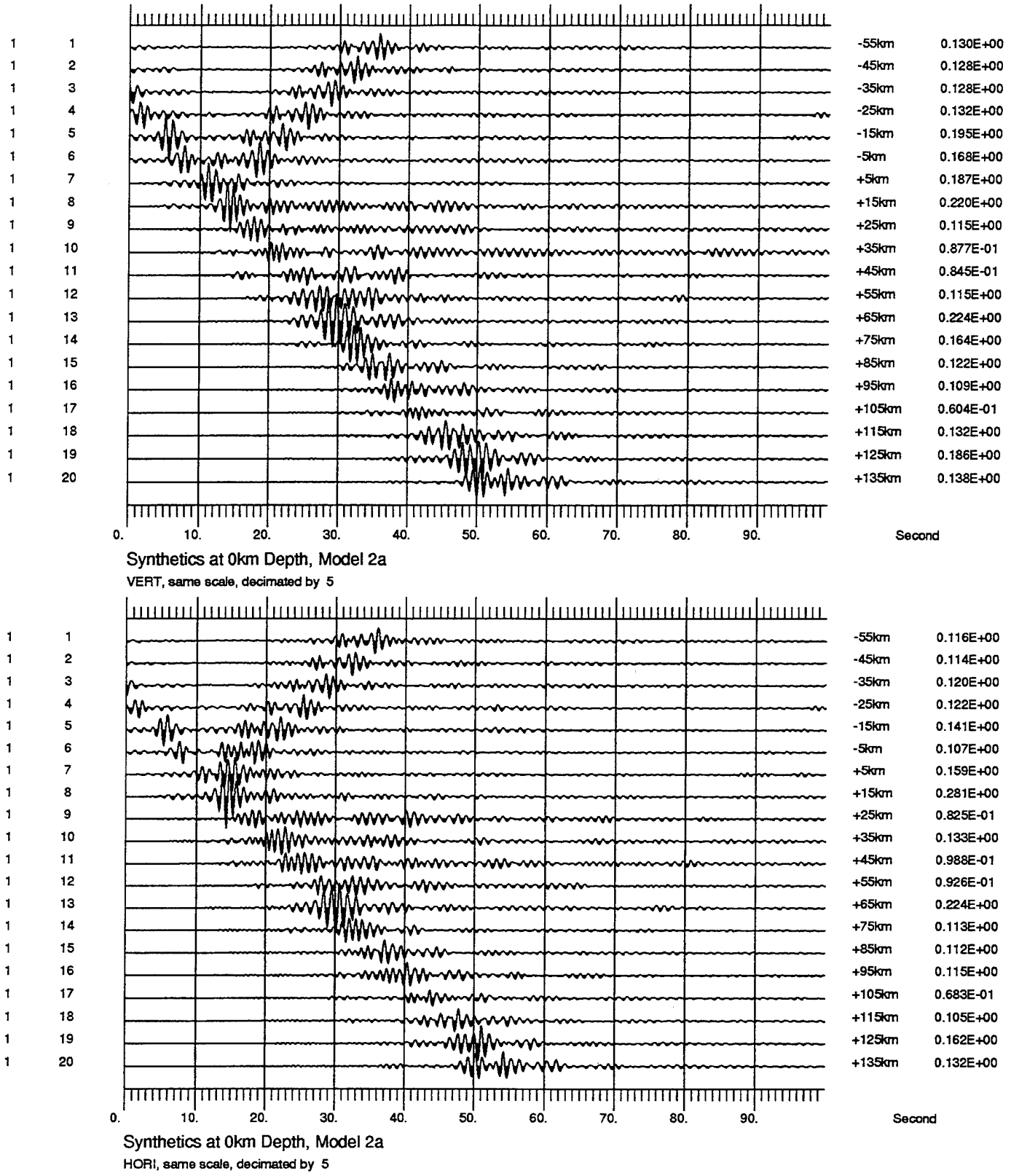

Figure 48. Seismic sections of model 2a, which has a moderate free-surface topography and a fully compensated Moho. The scattering effects of topography on L_g are not as strong as those due to large-scale structural discontinuities.

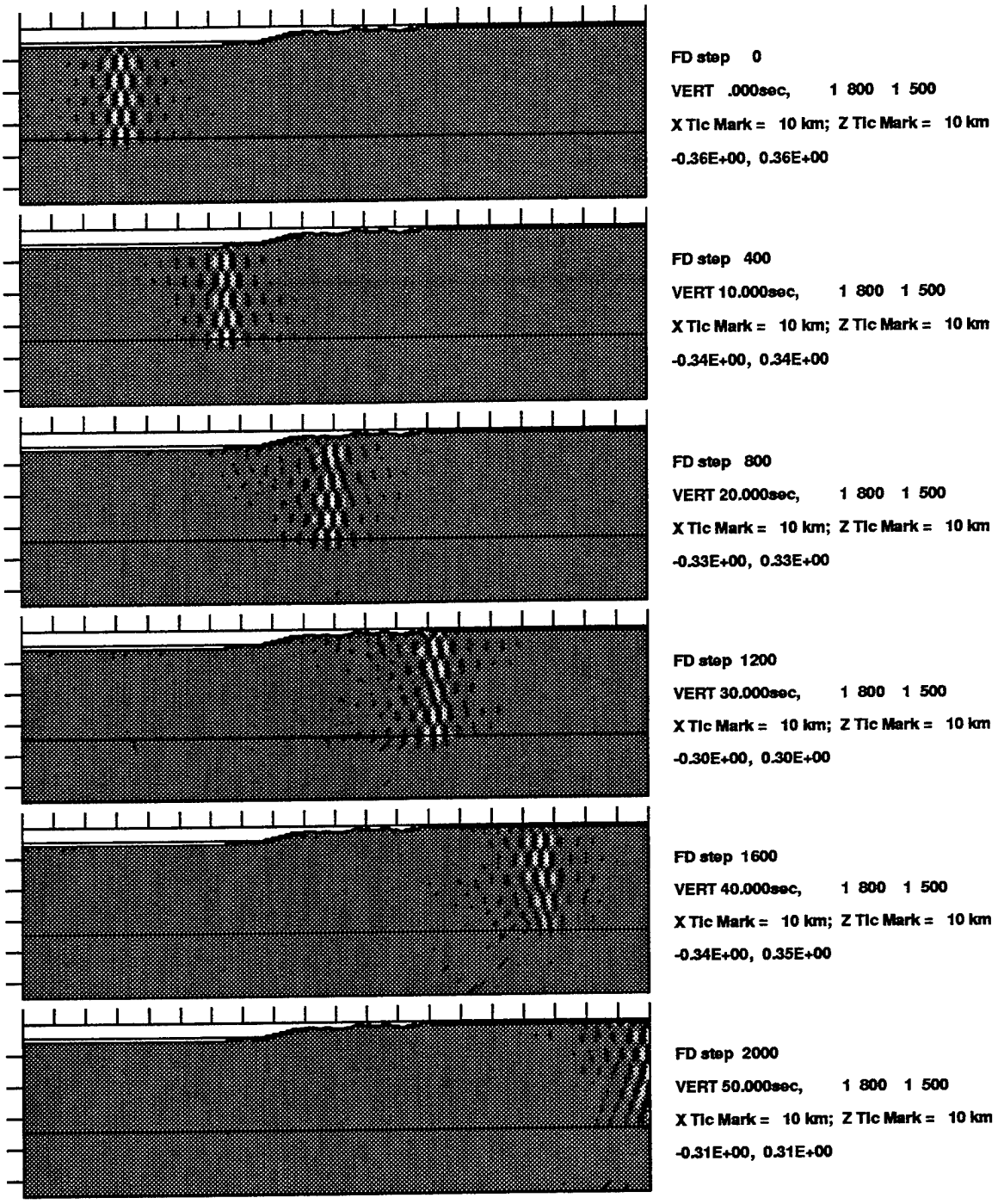

Figure 49. The vertical-component snapshots of L_g wave propagation of model 3. The elevation change of this topographic profile is relatively small compared to the thickness of the homogeneous crust, and hence the transmission of L_g is still fairly efficient.

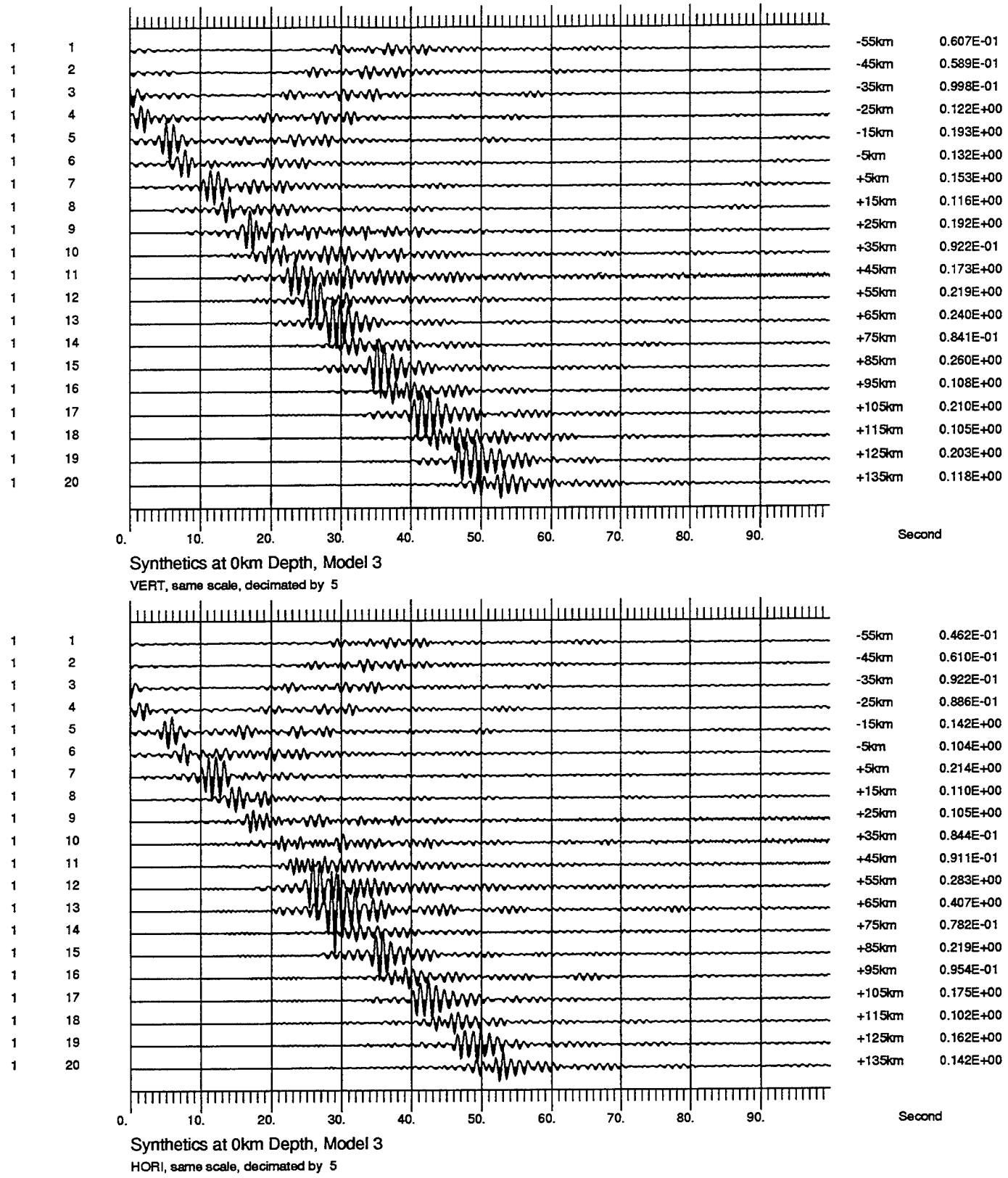

Figure 50. Seismic sections of model 3, which has a moderate free-surface topography and a flat Moho. The scattering effects of topography on L_g are not as strong as those due to large-scale structural discontinuities.

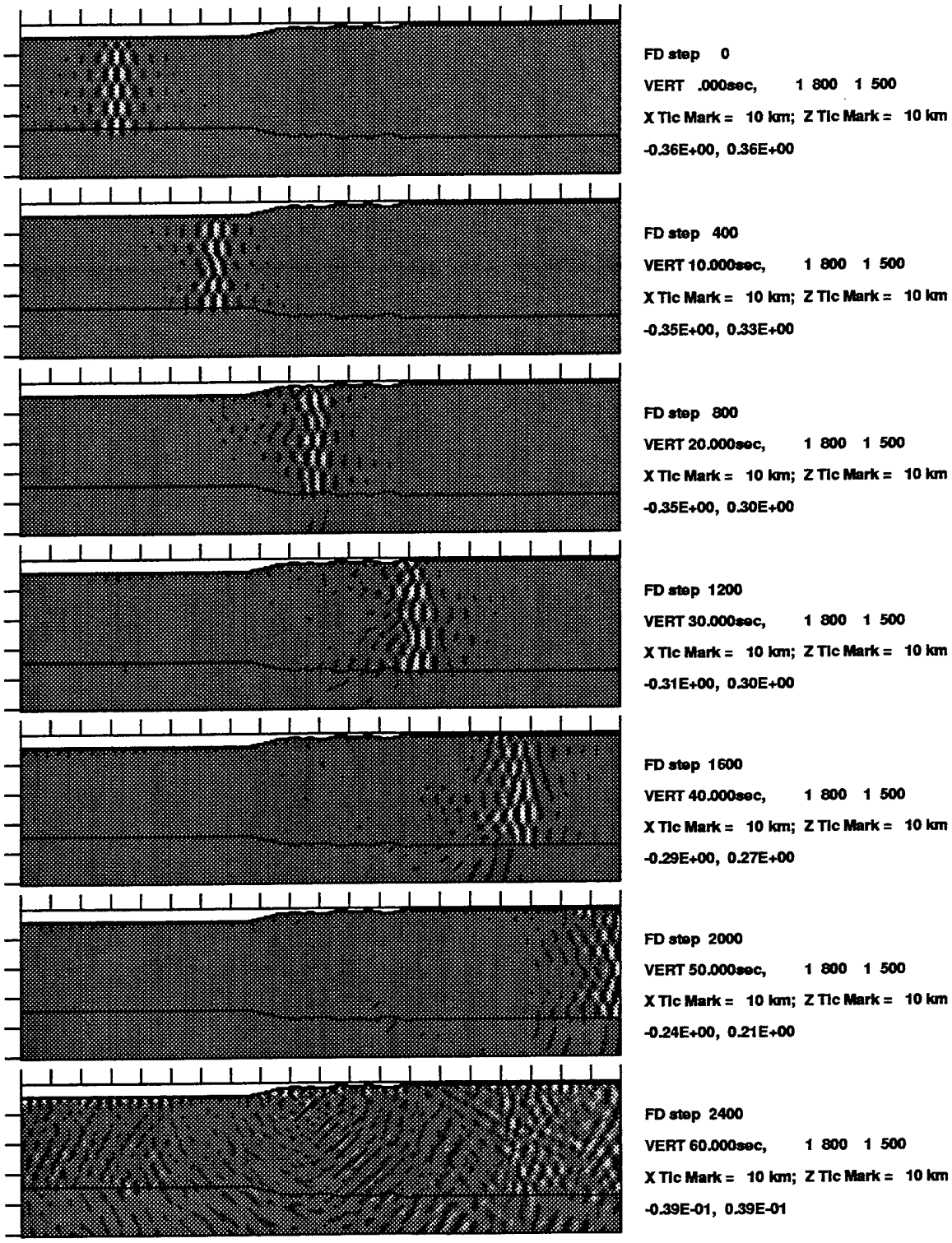

LFD Simulation of Lg Propagation: Model 3a

Figure 51. The vertical-component snapshots of L_g wave propagation of model 3a, in which the Moho is fully compensated. The elevation change of this topographic profile is relatively small compared to the thickness of the homogeneous crust, and hence the transmission of L_g is still fairly efficient.

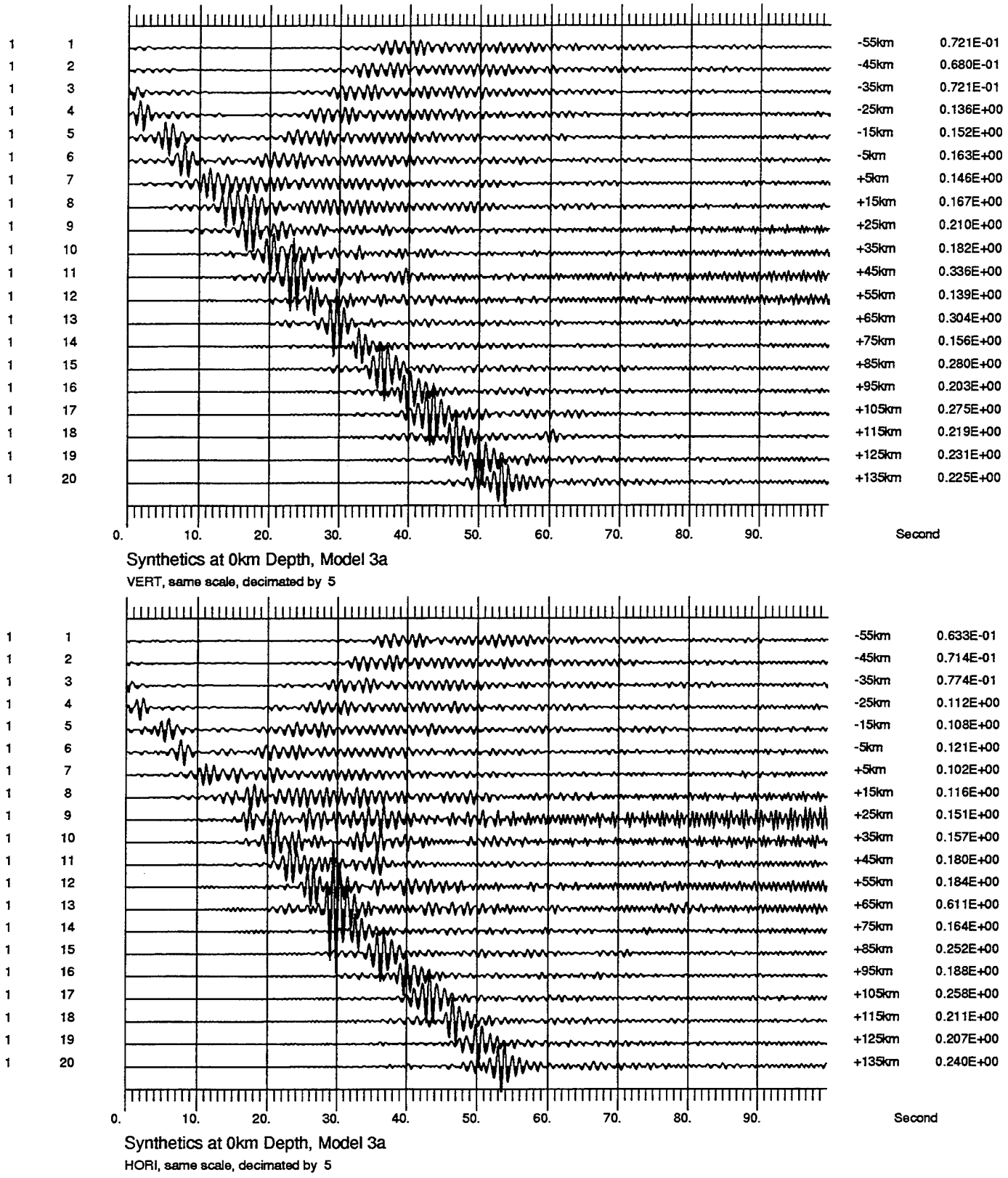

Figure 52. Seismic sections of model 3a, which has a moderate free-surface topography and a fully compensated Moho. The scattering effects of topography on L_g are not as strong as those due to large-scale structural discontinuities.

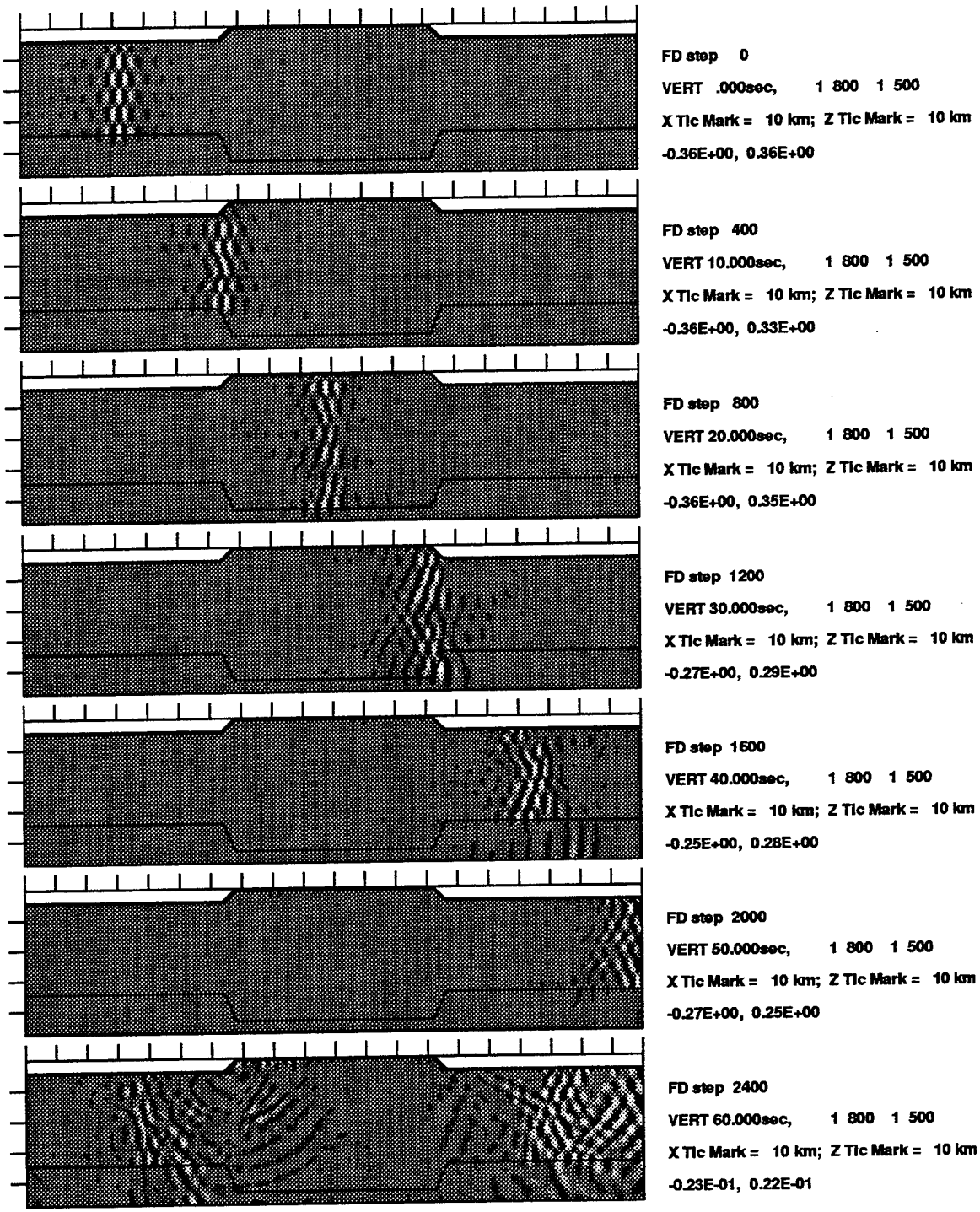

LFD Simulation of Lg Propagation: Model 4

Figure 53. The vertical-component snapshots of L_g wave propagation of model 4.

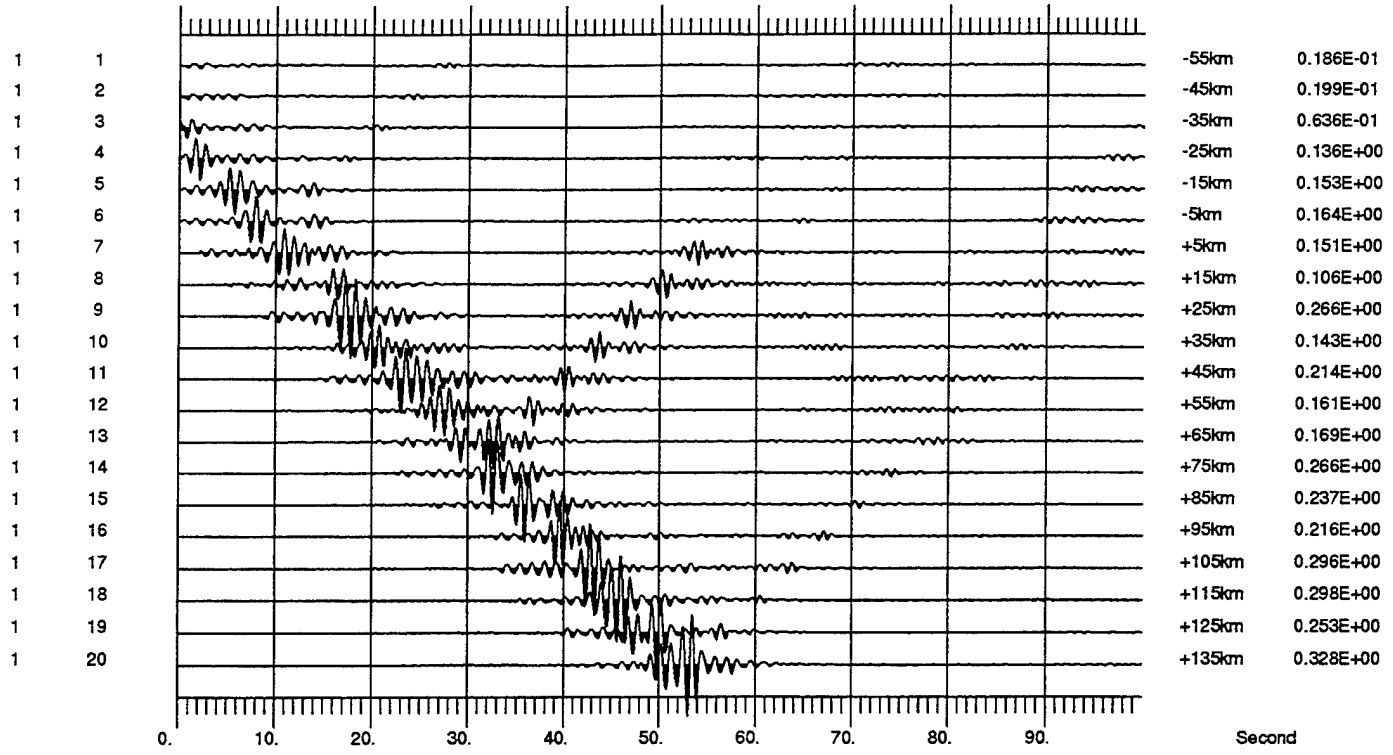

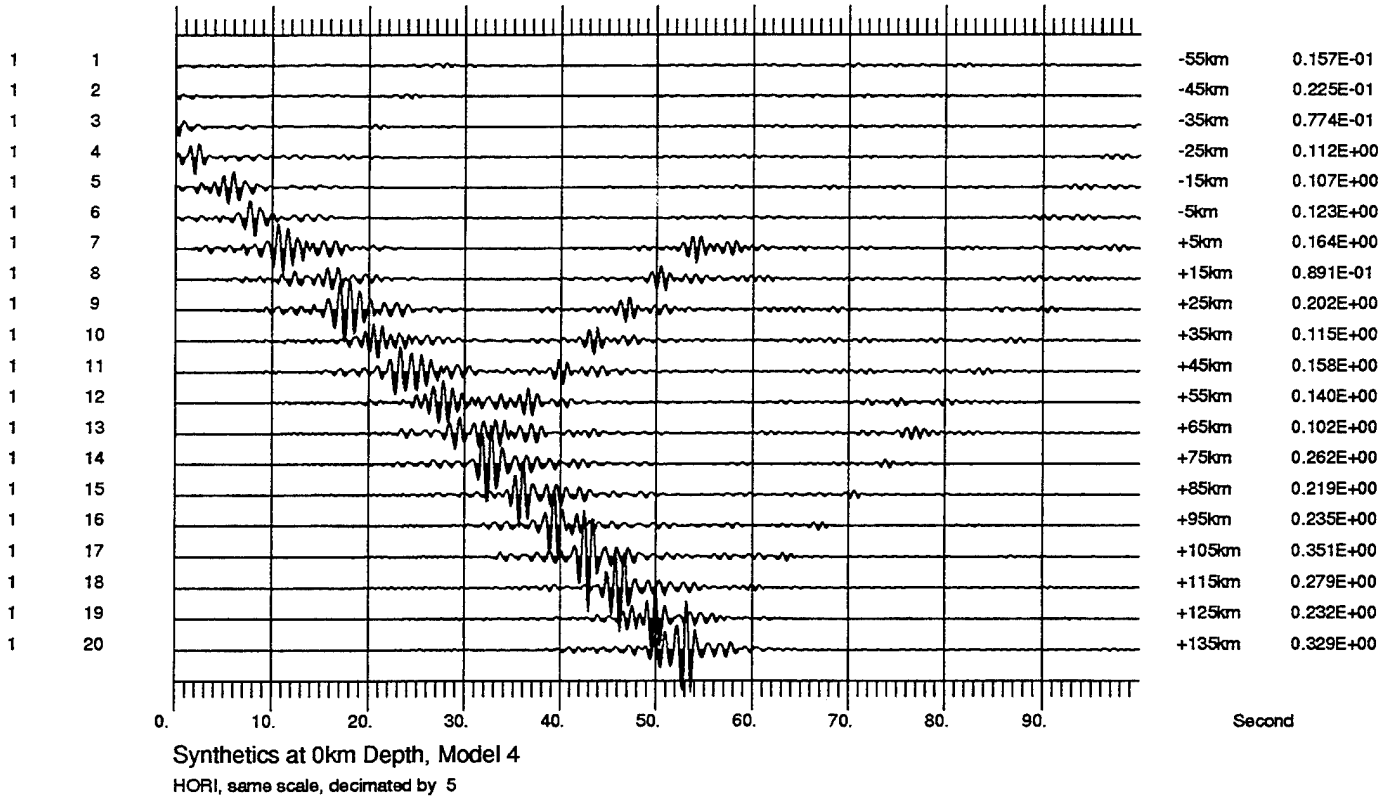

Figure 54. Seismic sections of model 4, which has a trapezoidal topography and a fully compensated Moho.

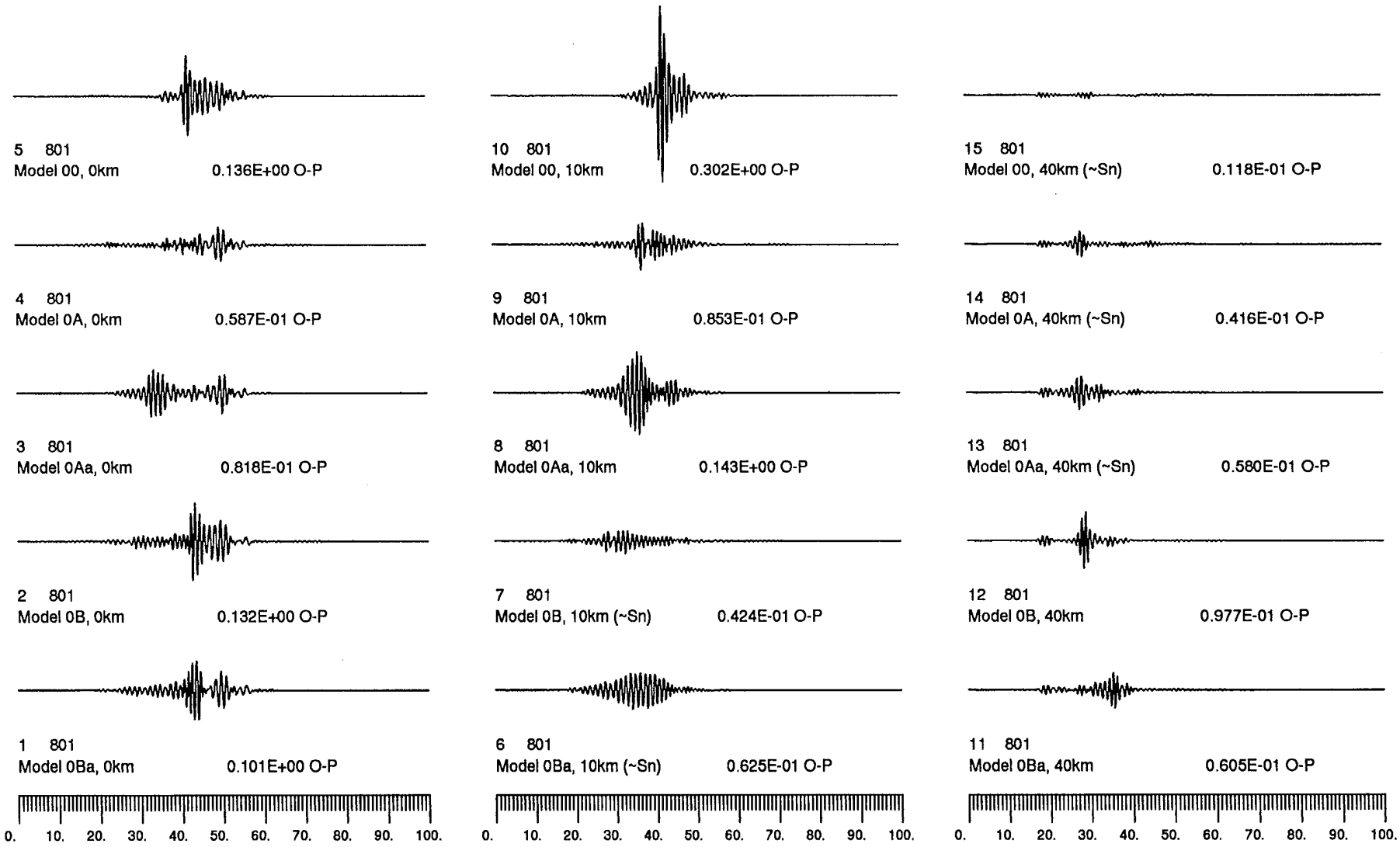

Synthetics (@ 3 Depths) of Various Crustal Models: 0Ba, 0B, 0Aa, 0A, 00

Figure 55. Vertical-component synthetic seismograms recorded at 3 depths (0km, 10km, and 40km) and started at 20 seconds for models 00, 0A, 0Aa, 0B, and 0Ba, respectively. While both models with Moho uplift (0A and 0Aa) clearly exhibit a blockage for the "on-time L_g", only model 0Aa generates the "early L_g" (left). Although the "on-time L_g" on surface synthetics of models 0B and 0Ba (bottom left) have a peak amplitude in the same order as that of the reference model, they are not the same overtone of the Rayleigh mode.

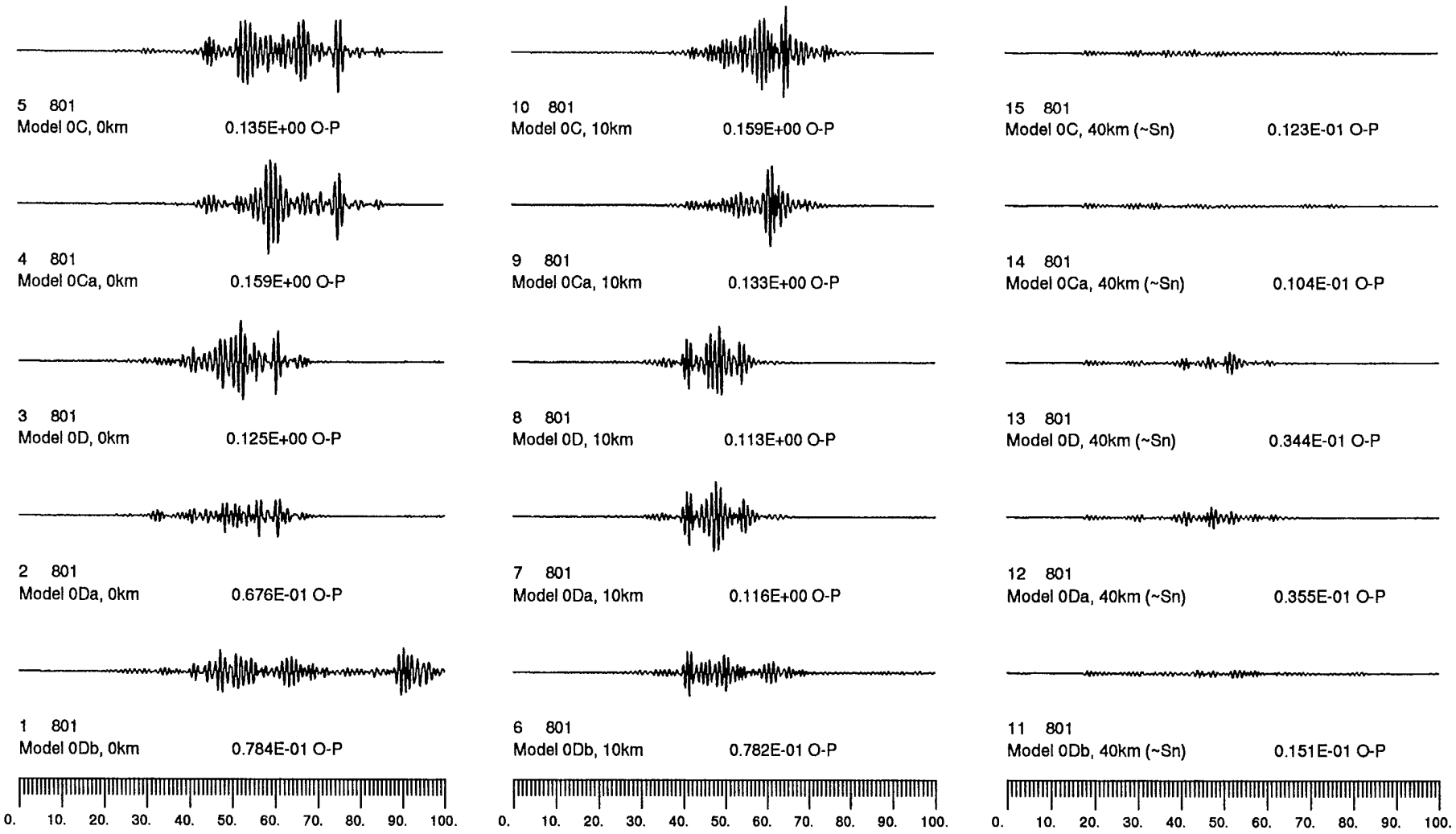

Synthetics (@ 3 Depths) of Various Crustal Models: 0Db, 0Da, 0D, 0Ca, 0C

Figure 56. Same as Figure 55 except for models 0C, 0Ca, 0D, 0Da, and 0Db. All these models have embedded sedimentary layer(s) and hence the L_g energy is delayed. There is relatively less energy that would penetrate the Moho, as shown on the waveforms at 40 km. The model 0Db generates enhanced R_g waves (bottom left).

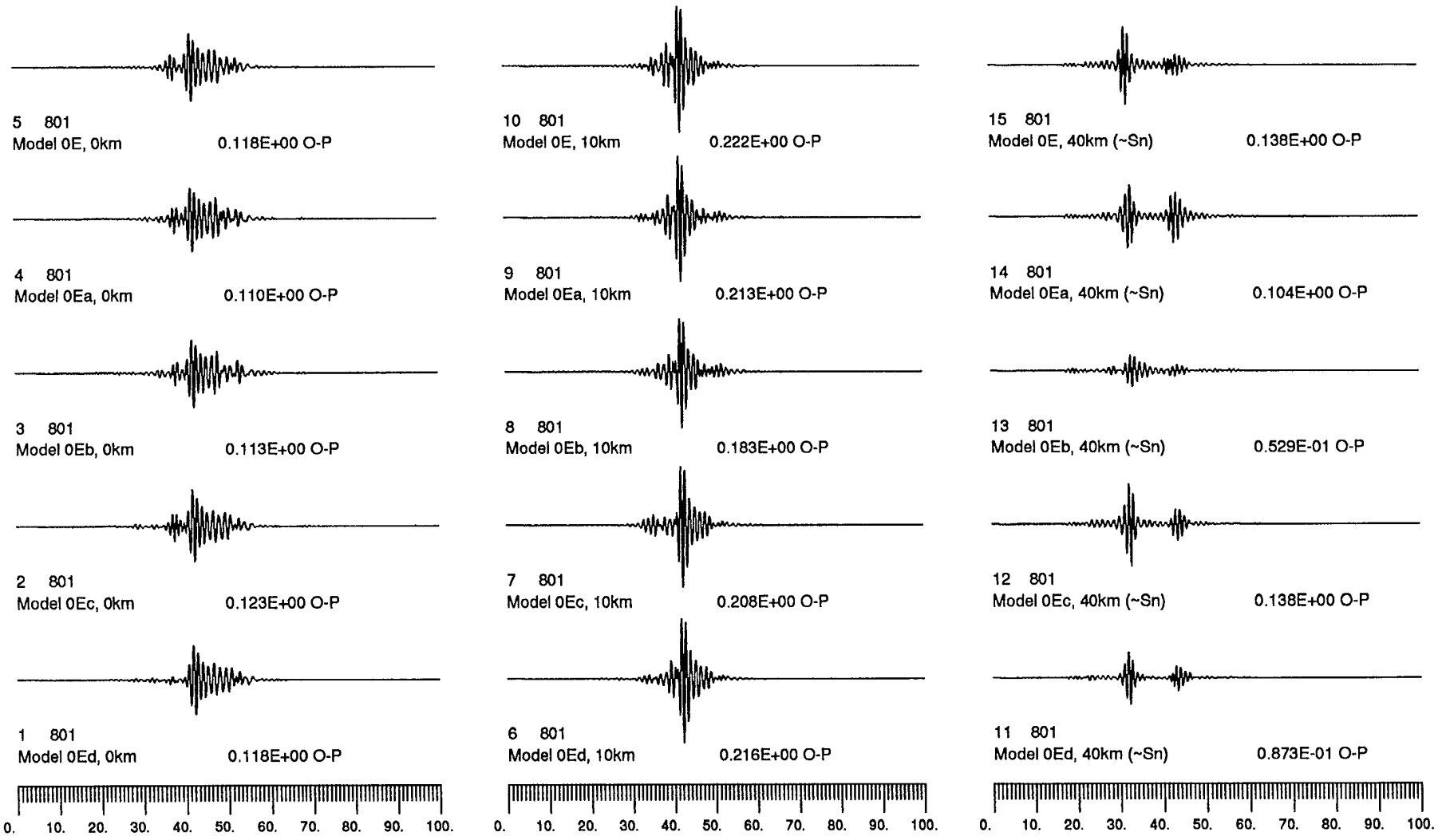

Synthetics (@ 3 Depths) of Various Crustal Models: 0Ed, 0Ec, 0Eb, 0Ea, 0E

Figure 57. Same as Figure 55 except for models 0E, 0Ea, 0Eb, 0Ec, and 0Ed. Models of the "E" series excite very strong Sm phase.

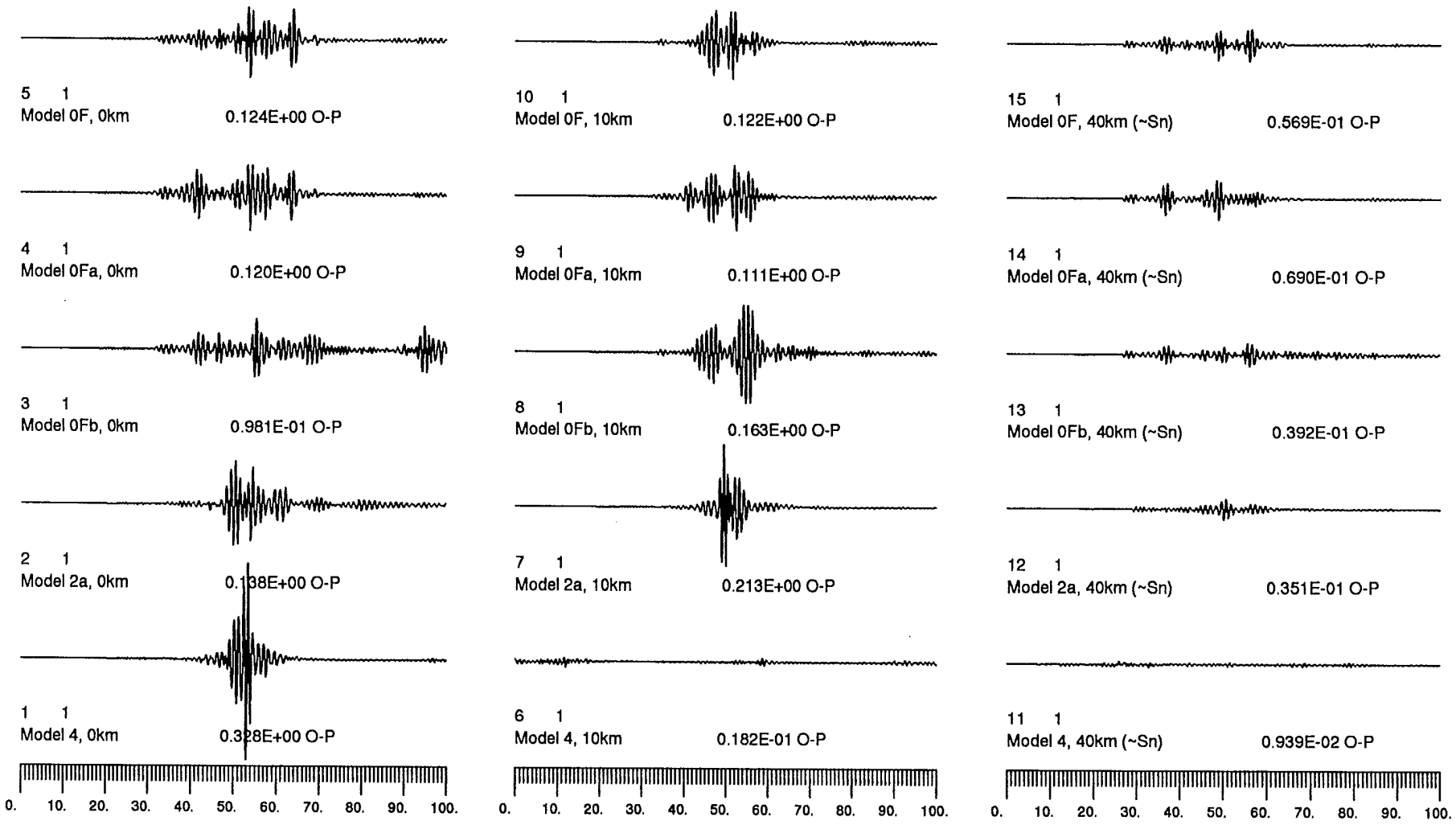

Synthetics (@ 3 Depths) of Various Crustal Models: 4, 2a, 0Fb, 0Fa, 0F

Figure 58. Same as Figure 55 except for models 0F, 0Fa, 0Fb, 2a, and 4. The moderate surface and Moho topography in model 2a affect L_g waveform characteristics only mildly. Model 0Fb excites very strong R_g phase, very similar to model 0Db (see bottom left of Figure 56).

4. L_g PROPAGATION IN ANELASTIC MODELS

The incorporation of intrinsic attenuation due to an arbitrary absorption law is believed to be straightforward in frequency-domain methods. However, so far many codes used in waveform synthesis (such as the reflectivity method and the wavenumber-integration method) can only handle a frequency-independent Q.[1] Bache *et al.* (1981) found that L_g synthetics made for models with frequency-independent Q do not attenuate with the proper frequency dependence. If models are constructed that match L_g amplitude-distance relationship at 1 Hz, then L_g synthetics would attenuate too rapidly at higher frequencies.

For the time-domain-based numerical methods, it has been very difficult to add the intrinsic attenuation because the anelastic stress-strain relation has the form of a convolution integral, which is intractable in a numerical computation. Vidale and Helmberger (1988) convolved finite-difference synthetics with a time-varying operator to model the effect of anelastic attenuation. This method is not suitable for media with spatially-varying Q. This method is also not appropriate when there are significant wave conversions (P to S *etc.*) in media where Q_P is not equal to Q_S. The first successful attempt to incorporate realistic attenuation laws into time-domain methods was made by Day and Minster (1984) based on the method of Pade approximation, which yields an expansion of the frequency-dependent viscoelastic modulus into a rational function. Emmerich and Korn (1987) propose a slightly different method based on the rheological model of the generalized Maxwell body, which has a modulus of the desired rational form. The major inconvenience of these approaches is that they demand a continual storage of five or more time steps of the wave field, depending on the accuracy of the approximation. The non-causal nature of some of these techniques is another fundamental drawback, at least conceptually, since in reality the anelastic attenuation of the Earth should act in a causal manner. That is, the dissipation of energy should occur as soon as the seismic wave arrives, and that the resulting displacement at the current time step should not be dependent on future displacement.

With all these considerations in mind, a different procedure is developed in this study to incorporate the anelastic attenuation. It turns out that if we drop the ambitious attempt of imposing an arbitrary (that is, user-defined) frequency-dependence on the Q operator, then it becomes very easy to implement a causal, phase-independent damping operator which is quite suitable for the LFD calculation. Several researchers have readily demonstrated that the performance of commonly used absorbing boundary conditions can be greatly improved if a viscous damping zone is added to the grid boundary (Cerjan *et al.*, 1985; Levander, 1985a). The damping zone simply reduces the amplitude in a pointwise manner. There is no reason why this technique can not be exploited to model the anelastic attenuation.

[1] A wavenumber-integration code with this limitation lifted is being developed at S-Cubed by K. McLaughlin.

Different seismic waves are used as the initial pulse in these examples to demonstrate the effectiveness of this algorithm.

Consider the simplest isotropic homogeneous medium in which the amplitude of seismic waves decays exponentially with traveling distance:

$$A(f, \Delta) = A_0(f) \cdot G = A_0(f) \cdot e^{-\gamma \cdot \Delta} \quad , \qquad [1]$$

where $\gamma = \frac{\pi \cdot f}{U \cdot Q}$, U is the group velocity, and Δ is the distance traveled. In LFD calculations, Δ is taken to be the distance that the seismic wave would travel within one temporal step of the LFD iteration, that is, $\Delta = U \cdot dt$. Thus G can also be written as $e^{-\frac{\pi \cdot f \cdot dt}{Q}}$. There exists a constant η such that

$$G = e^{-\gamma \cdot \Delta} = 1 - \eta \cdot \gamma \cdot \Delta \, . \qquad [2]$$

It implies that $G = 1 - \frac{\eta \cdot \pi \cdot dt \cdot f}{Q}$ and hence $Q = Q_0 \cdot f$ if we define Q_0 to be $\frac{\eta \cdot dt \cdot \pi}{1 - G}$. If the damping term G is a function of the grid coordinate only and invariant with frequency, then we would have a Q increasing linearly with frequency. If, however, a frequency-dependent G is used at separate LFD simulations, then combining the band-limited LFD results would produce the solution for that particular frequency-dependent Q model. Here the parameter η is a function of γ or G, and the means of determining η will be discussed later. In practice, however, the users only need to specify a multiplicative constant G slightly less than 1 for each grid point. These localized damping factors are used to modify the displacement field pointwise at each iteration step. The decay rate (γ) and the quality factor (Q) can be determined later, after the finite-difference calculation is done. A possible drawback of this approach is that if a specific frequency-dependent Q model is desired, then several separate LFD simulations need to be carried out for each frequency–Q pair of interest, as discussed above. Nevertheless, this possible shortcoming of this approach is outweighed by its simplicity. More importantly, this procedure preserves the causality. Another characteristic of this approach is that, given a damping factor G in a P-SV LFD calculation, $Q_0 = \frac{\eta \cdot dt \cdot \pi}{1 - G}$ would be applicable to both P and S phases. Thus, Q_P and Q_S should be about the same.

So far we have derived several necessary conditions for an anelastic attenuation model, based on the desired exponential decay of seismic amplitude. In the following, we shall take a schematic view of this proposed algorithm. Consider the heterogeneous acoustic wave equation in the nondissipative medium:

$$\frac{\partial^2 P}{\partial t^2} = c^2(x, z)\left[\frac{\partial^2 P}{\partial x^2} + \frac{\partial^2 P}{\partial z^2}\right] \, , \qquad [3]$$

where P is the acoustic displacement potential, and c(x, z) is the acoustic velocity at the node (x, z).

LFD iteratively solves for the current pressure at (x, z) using that of the past within a spatially-limited region surrounding the grid (x, z). The actual size of the temporal and spatial buffers required depends on the order of the LFD scheme. At each time step, the resulting unattenuated pressure P is then multiplied by the damping G to get the dissipated $\tilde{P}$. Once the whole pressure field is updated and dissipated (grid by grid) with the corresponding spatial damping factors, the standard LFD iteration restarts for the next pressure field without damping, and then damping factors are applied again. The procedure for the P-SV LFD calculation is exactly the same. It should be obvious that the extra calculation and memory required in this procedure are minimum. We can envision the pointwise damping factor as a degenerate digital filter which has only one point of temporal span (that is, memory). It can be regarded as the limiting case of the convolutional integral of many attenuation operators typically used in the frequency-domain approach.

The attenuated pressure, $\tilde{P} = P \cdot G$, can also be written as

$$\tilde{P} = P - \frac{\eta \cdot \pi \cdot dt \cdot f}{Q} \cdot P \,. \qquad [4]$$

That is, $\tilde{P}$ can be obtained by adjusting the undissipated P a little. The coefficient of pressure loss, $\frac{\eta \cdot \pi \cdot dt \cdot f}{Q}$ is very similar to the coefficient of friction term that Levander (1985) (and Frankel and Wennerberg, 1987) used in the telegraphy equation. The difference is that we have added the η term here to account for the correct relationship between Q and the damping effect. Jih (1996) gives a more detailed discussion as well as several examples using different seismic waves as input to demonstrate the effectiveness of this algorithm.

Seven models with Q_0 values varying from 60 to 500 are tested in this study. The attenuative portion is 100 km long and 30 km thick. In each case, a significant fraction of the energy is lost due to absorption. Nevertheless, the chessboard pattern of the initial L_g wave packet is retained for all models. In fact, none of these seven models exhibits any notable scattering (see Figures 59 through 62). Also, the linear frequency-dependence of the resulting Q is quite clear, so is the frequency-independent γ (Table 3). These observations strongly indicate that the simple attenuation operator proposed for the LFD method is adequate for operational purposes.

Following the same quantification procedure as in the previous section, amplitude ratios representing the L_g transmission and coupling to other phases are computed. Instead of using the surface synthetic to measure the quality factor and γ, the amplitude ratio of transmitted L_g waves is based on that at a depth of 10 km, which we find to be a more stable measure of the transmitted energy. The results are summarized in Table 3 below.

Table 3. L_g Propagation Statistics of 7 Anelastic Models

Model, $e^{-\gamma\Delta}$	BK	T	S_n/L_g	far-P/L_g	far-S/L_g	Q_0	γ (1 Hz)	Q(2 Hz)	γ (2 Hz)
0Qa, 0.99747	0.175	0.200	0.053	0.026	0.014	59	0.0162	139	0.0138
0Qb, 0.99873	0.418	0.445	0.049	0.026	0.013	117	0.0082	249	0.0077
0Qc, 0.99916	0.590	0.614	0.056	0.027	0.014	196	0.0049	398	0.0048
0Qd, 0.99937	0.672	0.695	0.059	0.028	0.015	263	0.0036	531	0.0036
0Qe, 0.99949	0.718	0.739	0.060	0.028	0.017	316	0.0030	635	0.0030
0Qf, 0.99958	0.770	0.786	0.060	0.028	0.018	396	0.0024	796	0.0024
0Qh, 0.99968	0.826	0.835	0.060	0.029	0.020	530	0.0018	1054	0.0018

BK: spectral amplitude ratio at 1 Hz of "on-time L_g " (3.33 km/sec) to that of the reference model.

T: spectral amplitude ratio at 1 Hz of transmitted L_g (recorded at a depth of 10 km) to that of the reference model.

Sn/Lg: spectral amplitude ratio at 1 Hz of converted S_n to the reference L_g .

far-P/Lg: spectral amplitude ratio at 1 Hz of converted teleseismic P to the reference L_g .

far-S/Lg: spectral amplitude ratio at 1 Hz of converted teleseismic S to the reference L_g .

As Q increases, the transmission efficiency (T) also increases, as expected. However, the coupling of L_g into S_n or teleseismic phases does not seem to be affected. Reducing the thickness of the attenuating body does not seem to change this observation (Figure 62). This is different from the case of R_g in which Jih (1995, 1996) reported that the undissipated R_g energy could actually be converted into S or L_g waves. The reason for this difference is not clear as yet. A possible explanation is that it has to do with the fundamental difference between R_g and the higher modes. The particle motion of R_g is very localized in that the energy causing retrograde (or prograde) rolling at greater depths does not interact with the shallow portion of the crust. When the rolling at shallow depths is dissipated, the "waveguide" is actually changed and the undissipated energy at greater depth can no longer propagate in the same mode as R_g . As a result, it is converted into a pure shear or L_g -like wave (see Jih, 1995). On the other hand, L_g waves are the interference of planar S waves multiply reflected at the free surface and the Moho. This mode of propagation is more robust in that even if part of the energy on the wavefront is dissipated in the upper crust, the remaining part of the wavefront might still be able to propagate more or less along the original direction. L_g energy in the deeper crust will also be dissipated when it eventually reaches the upper crust. Likewise, the L_g energy in the shallow portion of the crust will be dissipated first and then eventually enter the deeper crust and so forth. Thus the shallow attenuating layer will affect the whole L_g wavefield in a relatively more uniform manner without breaking up the mode (eigenfunction). As a result, there will be no notable enhancement of S_n or teleseismic coupling.

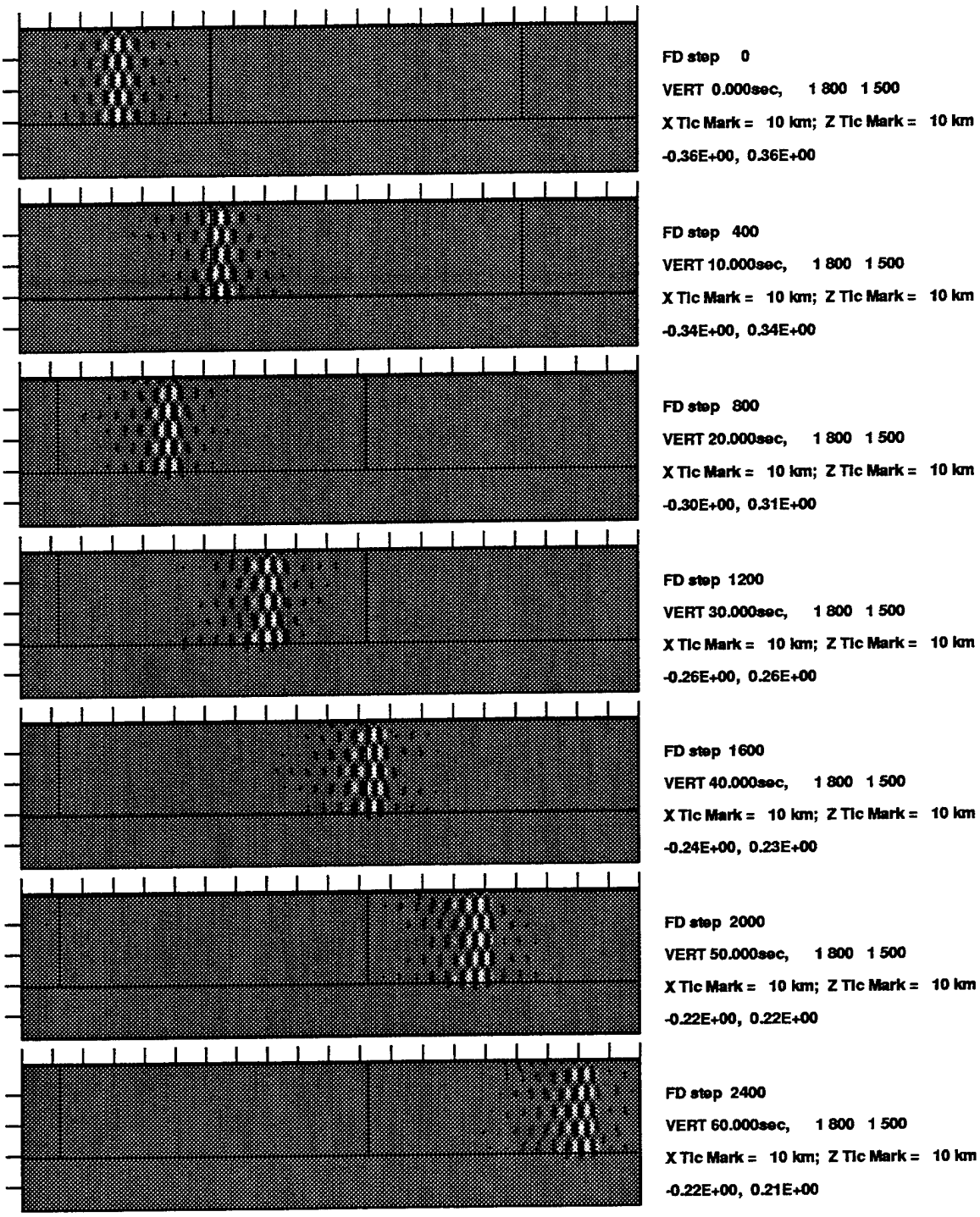

LFD Simulation of Lg Propagation: Model 0Qd,122

Figure 59. The vertical-component snapshots of L_g wave propagation in an anelastic mode, 0Qd, with Q_0 (L_g) = 263 for L_g waves. The anelastic portion of the model is 100 km long and 30 km thick. In this case, the effect of the intrinsic attenuation is to reduce the amplitude through dissipation. No significant scattering is observed.

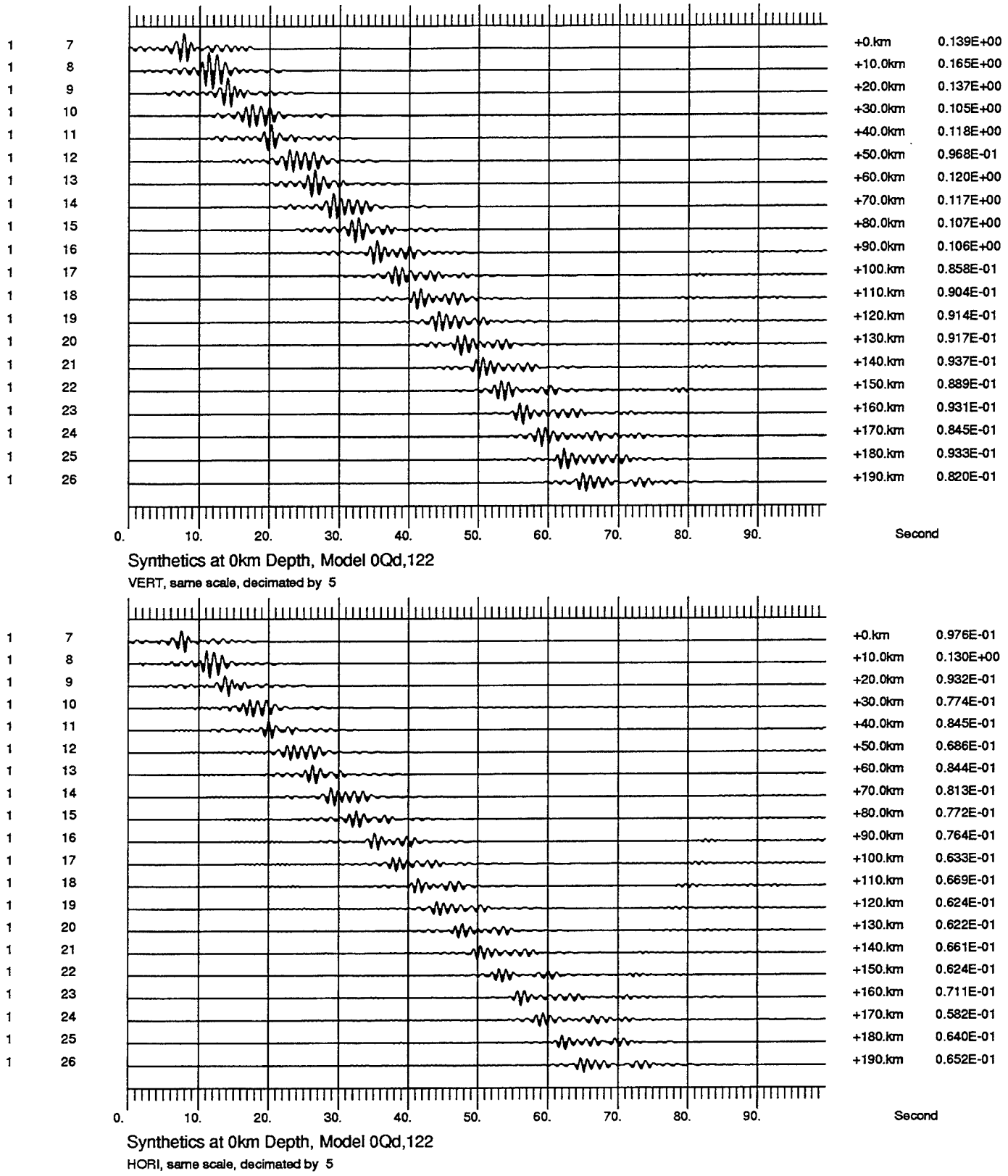

Figure 60. Seismic sections of model 0Qd,122 which has an attenuating body 100 km long, 30 km thick, with $Q_0(L_g) = 263$.

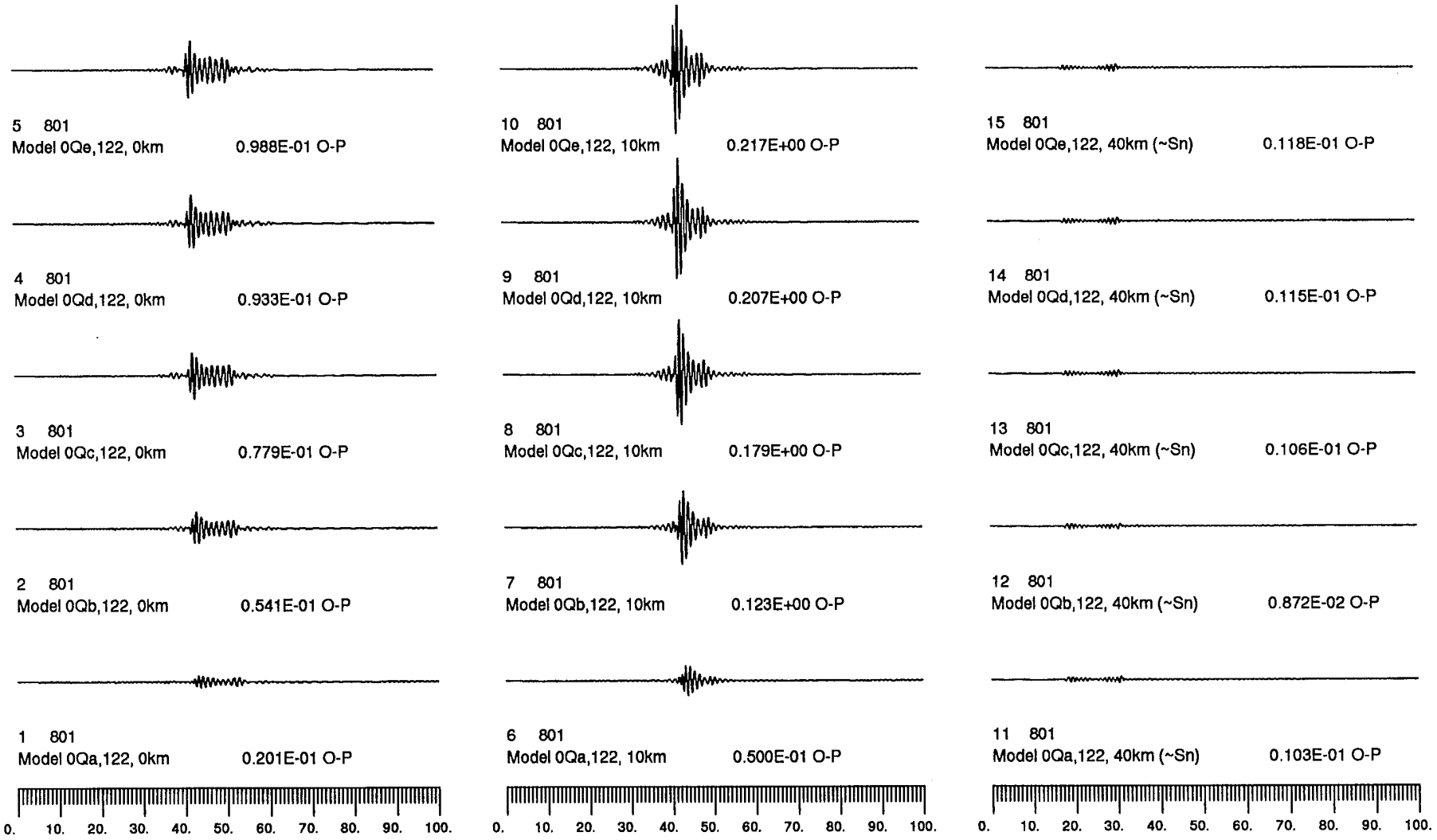

Synthetics (@ 3 Depths) of Various Crustal Models: 0Qa, 0Qb, 0Qc, 0Qd, 0Qe

Figure 61. Synthetic seismograms recorded at 3 depths (0km, 10km, and 40km) after crossing an anelastic zone 100 km wide and 30 km thick for five attenuative models. From top to bottom, the corresponding Q_0(Lg) values of these five models are 316, 263, 196, 117, and 59, respectively. Intrinsic attenuation reduces the L_g amplitude but does not cause any mode conversion.

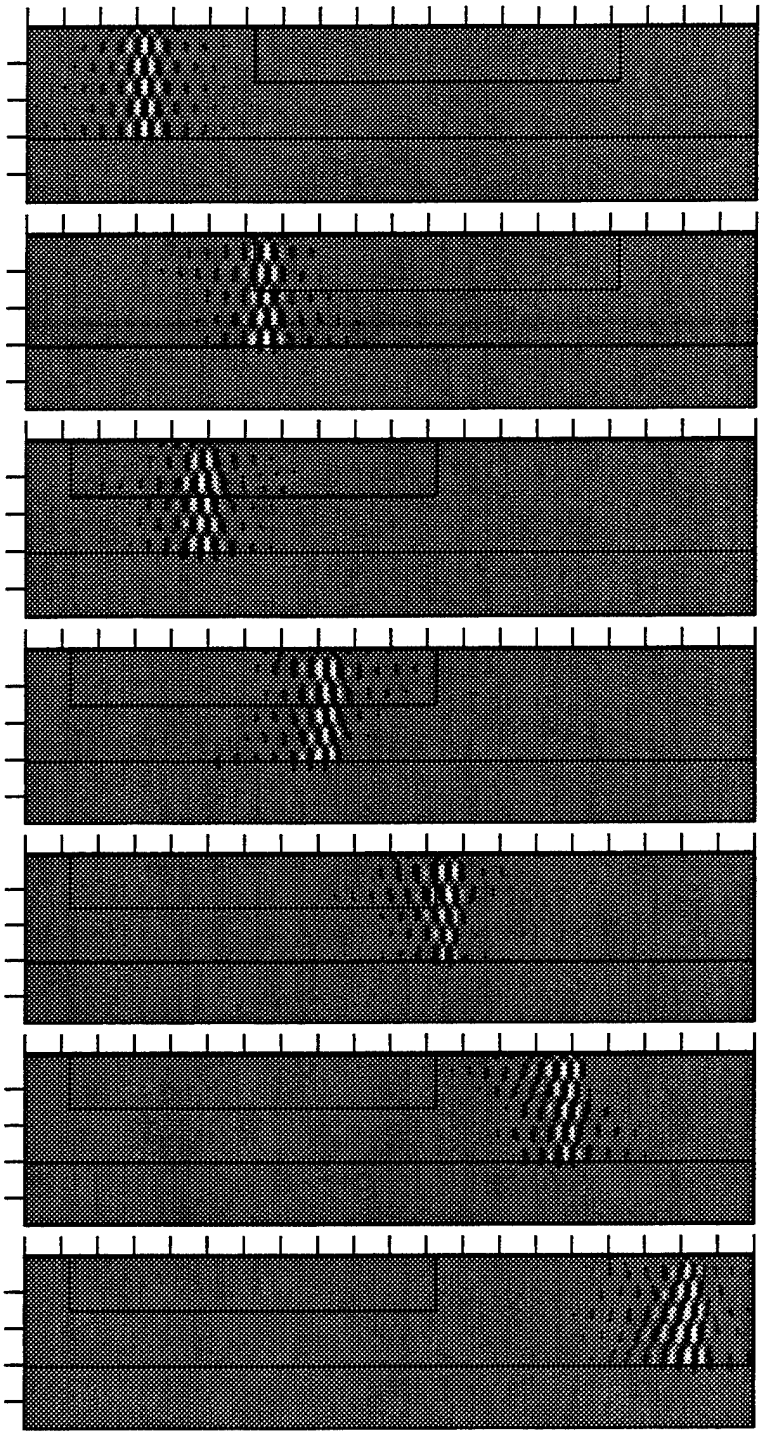

LFD Simulation of Lg Propagation: Model 0Qd,62

Figure 62. Similar to Figure 59 except a 15km-thick attenuative layer. For the L_g phase, the effect of intrinsic attenuation is to reduce the amplitude through dissipation. Changing the volume size (that is, the thickness) of the attenuating body does not seem to cause more mode conversion. This is very different from the case for R_g.

5. L_g PROPAGATION IN MODELS WITH RANDOM VELOCITY VARIATION

In an attempt to model the L_g blockage observed in the west Pyrenees Range, Chazalon *et al.* (1993) and Gibson and Campillo (1994) suggest that scattering by small-scale features within the lower crust is the primary reason for the observed blockage. In this section, several heterogeneous models with various RMS random velocity fluctuations are tested to quantify the scattering effects of small-scale heterogeneity on L_g. Figure 63 shows the vertical-component snapshots of L_g wave propagation in a single-layer model with a heterogeneous portion 100 km long and 30 km thick embedded in it. The self-similar random heterogeneity in this sandwiched portion has an RMS velocity fluctuation of 10 percent and a scale length of 1 km. The random medium is generated with the procedure described in Frankel and Clayton (1986).

As the RMS velocity variation increases to, say 20 percent, the scattered field becomes very complicated (*cf.* Figures 63 and 65). Contrary to the case with intrinsic attenuation alone, the small-scale random heterogeneity causes many kinds of coupling (scattering) (Figure 65). Table 4 below summarizes all the results. The "blocking" parameter (BK) was computed at two different depths, 0 and 10 km, and the latter is used in determining Q_0 and γ. Both the transmission of L_g and the coupling of other phases are directly affected by the change in the RMS velocity variation. As the RMS velocity variation increases, the amplitude ratio of transmitted L_g to the reference L_g wave drops significantly. The scattered energy enhances the coupling of S_n as well as those of teleseismic phases. It is interesting to note that L_g-to-S_n coupling is not a simple linear function of RMS velocity variation, unlike the coupling of teleseismic phases or L_g transmission. Figure 68 and Table 4 indicate that below 10%, the L_g-to-S_n coupling does exhibit a highly linear trend with the increasing complexity of the medium. The coupling drops as the RMS variation goes beyond 10%. Intuitively this could be because the scattered wavefield would become dominant and the isotropic point scatterers would radiate the energy in all directions.

Another observation is that as the RMS variation increases, the delay of the centroid of the L_g wave packet on the surface synthetics (see Figure 67) becomes very obvious. This is similar to the "stochastic dispersion" phenomenon McLaughlin and Anderson (1987) reported for P waves. In theory, the apparent attenuation and the dispersion should form a Hilbert transform pair, according to the Kramers-Kronig relation (Jacobson, 1987). This can be tested if the frequency band is broad enough.

Table 4. L_g Propagation Statistics of Random Models

Model	BK(0)	BK(10)	S_n/L_g	far-P/L_g	far-S/L_g	Q(1 Hz)	γ (1 Hz)
0Y, 2%	1.020	0.978	0.065	0.040	0.042	3934	0.0002
0Y, 3%	1.032	0.952	0.075	0.048	0.055	1878	0.0005
0Y, 4%	1.044	0.917	0.086	0.057	0.069	1088	0.0009
0Y, 5%	1.059	0.873	0.097	0.065	0.083	707	0.0014
0Y, 6%	1.077	0.822	0.108	0.073	0.096	494	0.0019
0Y, 7%	1.095	0.766	0.118	0.081	0.108	365	0.0026
0Y, 8%	1.114	0.706	0.126	0.089	0.118	280	0.0034
0Y, 9%	1.132	0.644	0.133	0.097	0.127	222	0.0043
0Y, 10%	1.146	0.583	0.138	0.106	0.134	181	0.0053
0Y, 11%	1.154	0.524	0.141	0.115	0.140	150	0.0064
0Y, 12%	1.154	0.471	0.143	0.126	0.144	128	0.0075
0Y, 13%	1.141	0.423	0.143	0.136	0.147	111	0.0086
0Y, 14%	1.115	0.381	0.142	0.145	0.150	98	0.0098
0Y, 15%	1.075	0.344	0.138	0.154	0.155	88	0.0108
0Y, 16%	1.020	0.313	0.133	0.161	0.161	81	0.0118
0Y, 17%	0.949	0.285	0.126	0.167	0.167	75	0.0127
0Y, 18%	0.859	0.260	0.118	0.171	0.173	70	0.0136
0Y, 19%	0.749	0.235	0.110	0.174	0.177	66	0.0146
0Y, 20%	0.625	0.210	0.103	0.174	0.181	61	0.0158

BK(0): spectral amplitude ratio at 1 Hz of "on-time L_g " (3.33 km/sec) to that of the reference model.
BK(10): spectral amplitude ratio at 1 Hz of transmitted L_g (recorded at a depth of 10 km) to that of the reference model.
Sn/Lg: spectral amplitude ratio at 1 Hz of converted S_n to the reference L_g.
far-P/Lg: spectral amplitude ratio at 1 Hz of converted teleseismic P to the reference L_g.
far-S/Lg: spectral amplitude ratio at 1 Hz of converted teleseismic S to the reference L_g.

Both anelasticity and small-scale random heterogeneity can contribute to the so-called "L_g blockage". Note that in practice the L_g blockage occurs whenever the peak L_g amplitude is below the signal level of other phases surrounding L_g. It certainly does not require the signal level in the predicted L_g window to be far below the noise level. In our calculations, a velocity variation of 8 percent or higher leads to an equivalent spatial Q of 270 or less, which would be sufficient to reduce the L_g amplitude by 30 percent or more for every 100 km it traverses (see the parameter T in Table 3). The classical example of "L_g blockage" along the path from the Novaya Zemlya test site to northern Scandinavia has a $Q_0(L_g)$ about 252, as discussed before. Based on Table 4, this level of attenuation is approximately equivalent to a model with a velocity variation of 8 percent alone. Stable shield regions are reported to have an RMS velocity variation less than 5 percent. For such paths, the corresponding spatial Q_0 value would be 700 or larger.

Some comparisons of various conversion mechanisms may be interesting. For a mountainous model, L_g -to-S is twice as strong as L_g -to-P (Table 2). (Here P and S refer to the teleseismic P and S, respectively.) For the "A" and "B" series of models, as well as the random media, these two mechanisms are about equally strong (see Tables 2 and 4). Anelastic models and "C"-type models have a L_g -to-S weaker than the L_g -to-P (Table 3), whereas models of the "D", "E", and "F" series show the opposite trend (Table 2).

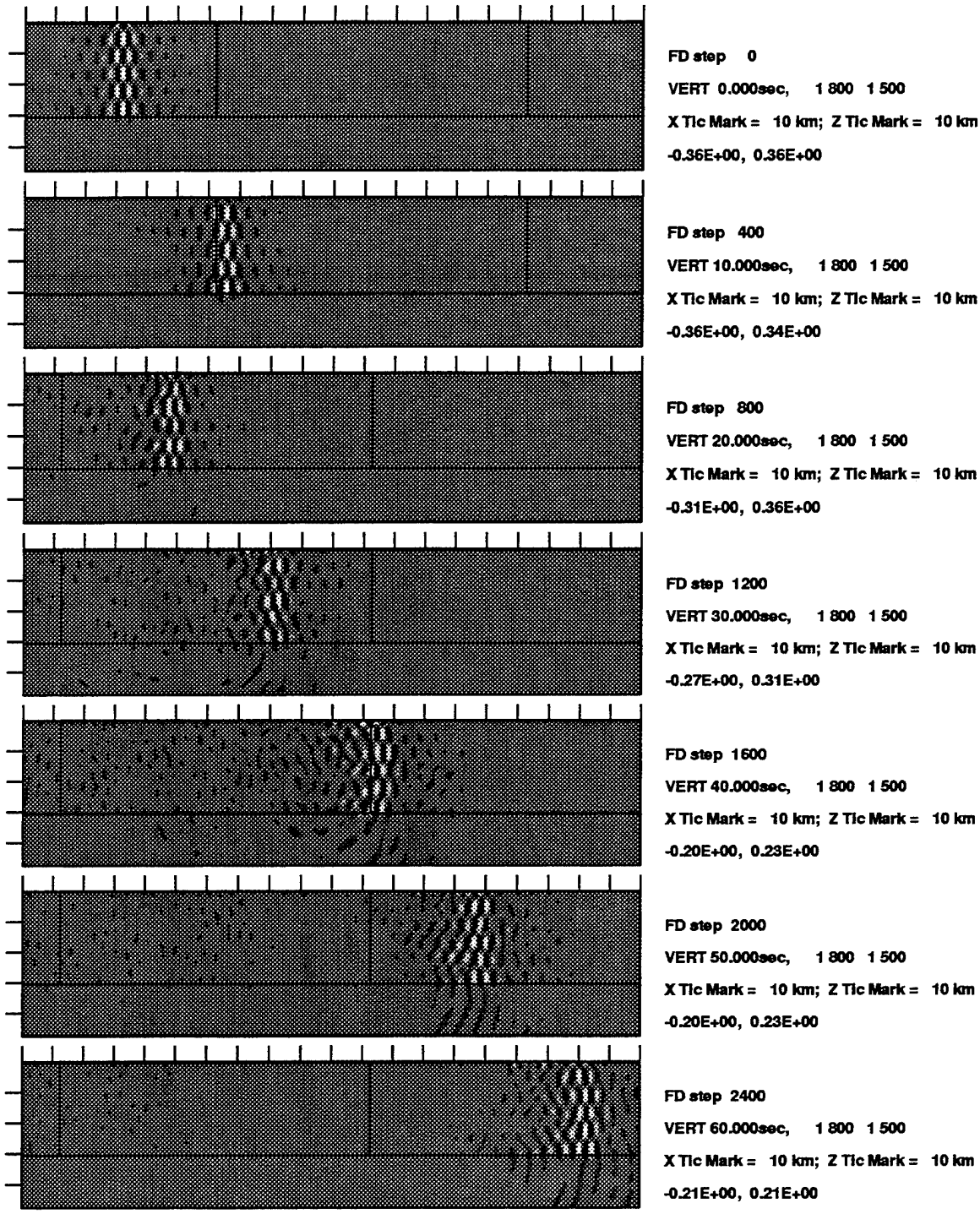

LFD Simulation of Lg Propagation: Model 0Y,10%

Figure 63. The vertical-component snapshots of L_g wave propagation in a single-layer model with a heterogeneous portion 100 km long and 30 km thick embedded in it. The self-similar random heterogeneity in this sandwiched portion has an RMS velocity fluctuation of 10 percent and a scale length of 1 km.

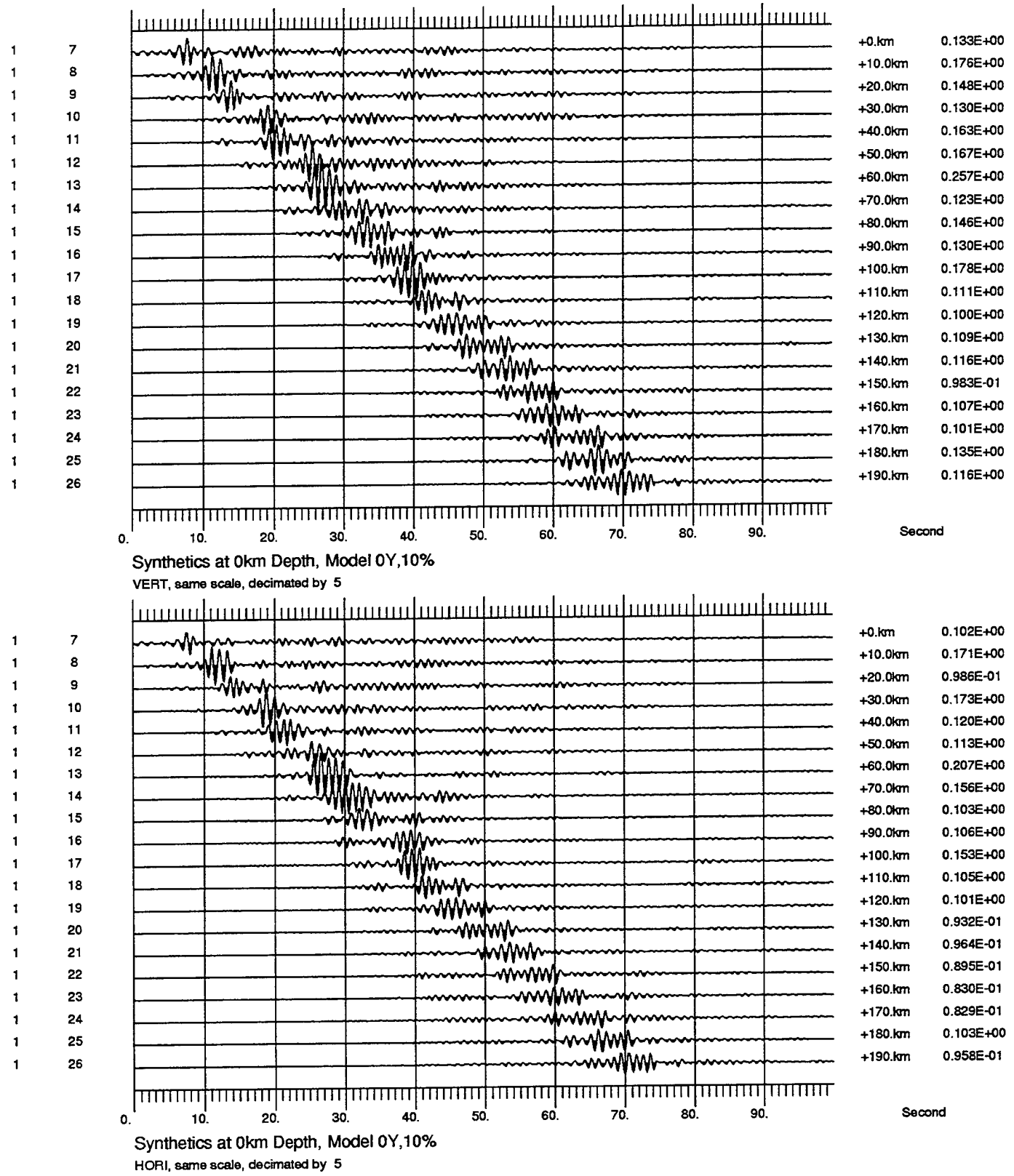

Figure 64. Seismic sections of the model 0Y,10%. This model has 10 percent velocity variation in an embedded heterogeneous volume which is 100 km long and 30 km thick.

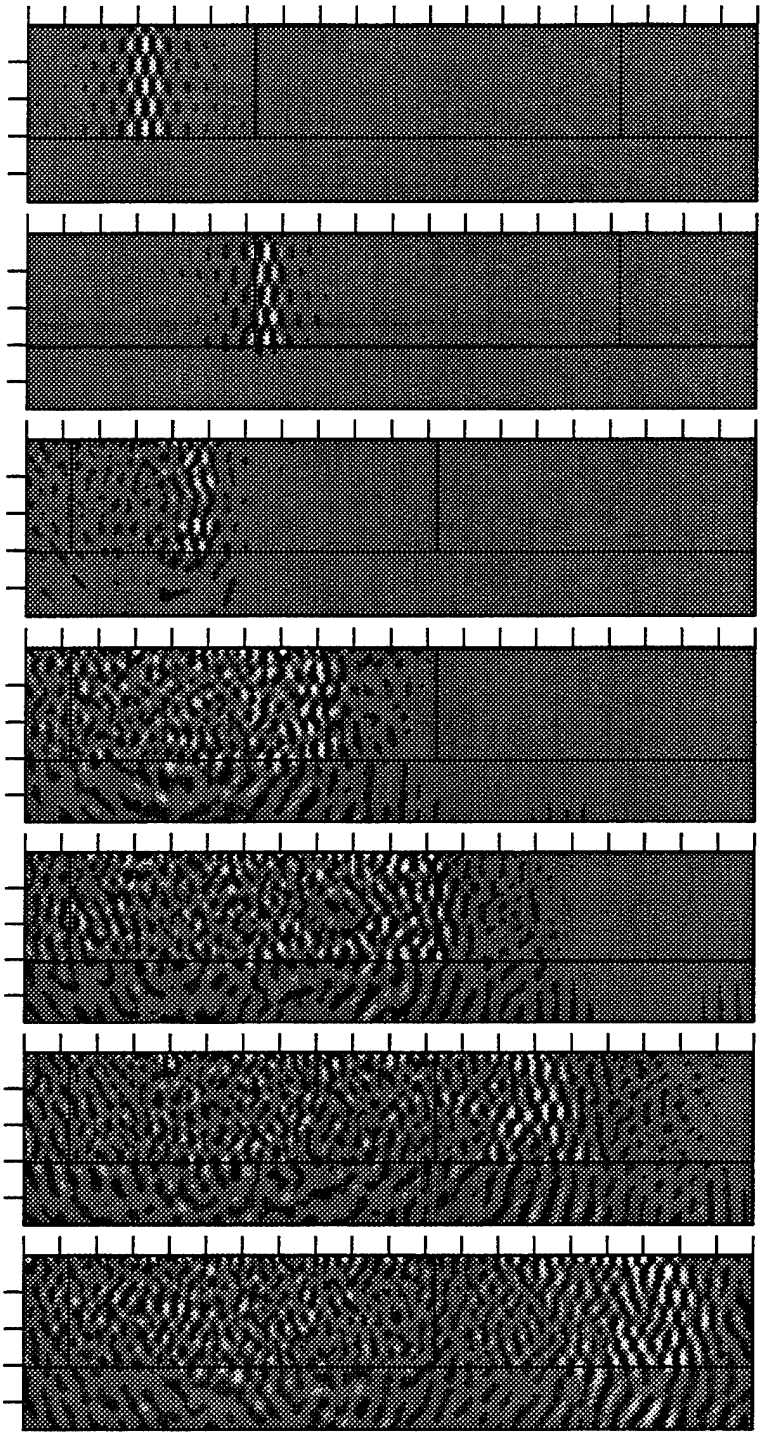

LFD Simulation of Lg Propagation: Model 0Y,20%

Figure 65. The vertical-component snapshots of L_g wave propagation in a single-layer model embedded with a heterogeneous portion 100 km long and 30 km thick in it. The self-similar random heterogeneity in this sandwiched portion has an RMS velocity fluctuation of 20% and a scale length of 1 km. The strong scattering generates a very complicated wavefield (as compared to Figure 63). Much of the scattered energy would contribute to coda waves.

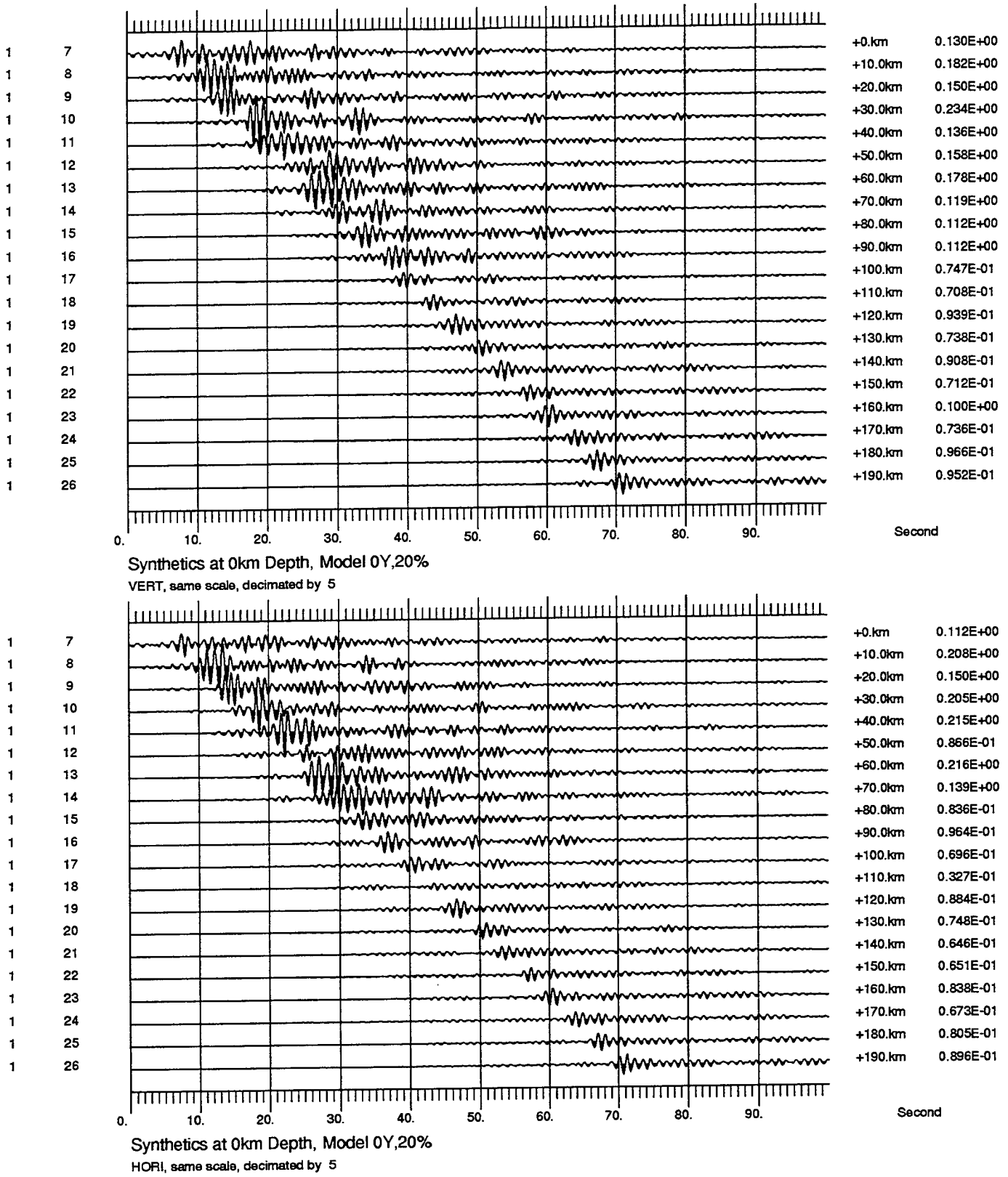

Figure 66. Seismic sections of the model 0Y,20%. This model has 20% velocity variation in an embedded heterogeneous volume which is 100 km long and 30 km thick. This model generates very long coda, as expected. Also note that the centroid of the L_g wave packet is delayed.

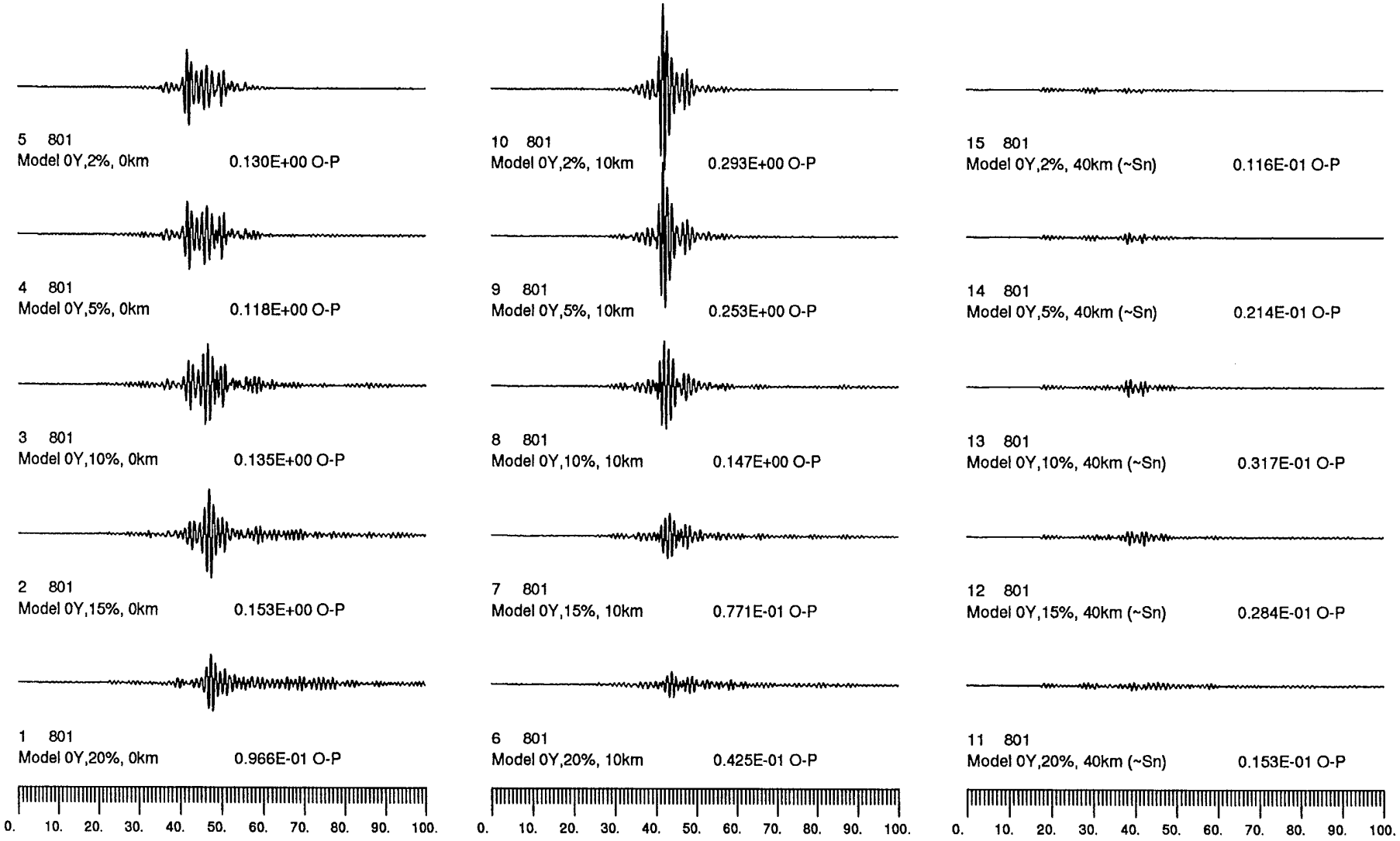

Synthetics (@ 3 Depths) of Various Crustal Models: 0Y,20%, 0Y,15%, 0Y,10%, 0Y,5%, 0Y,2%

Figure 67. Synthetics recorded at 3 depths (0km, 10km, and 40km) after crossing a heterogeneous zone 100 km wide and 30 km thick. As the velocity fluctuation increases from 2 percent (top) to 20 percent (bottom), the L_g amplitude decreases (as expected). The centroid of the L_g wavetrain also gets delayed somewhat. The L_g -to-S_n coupling decays once the RMS variation is greater than 13-15 percent, presumably because most of the energy has already been lost to scattering in all directions. A variation of 2 percent leads to very little scattering and hence the synthetics are very similar to those of the reference model (see Figure 61).

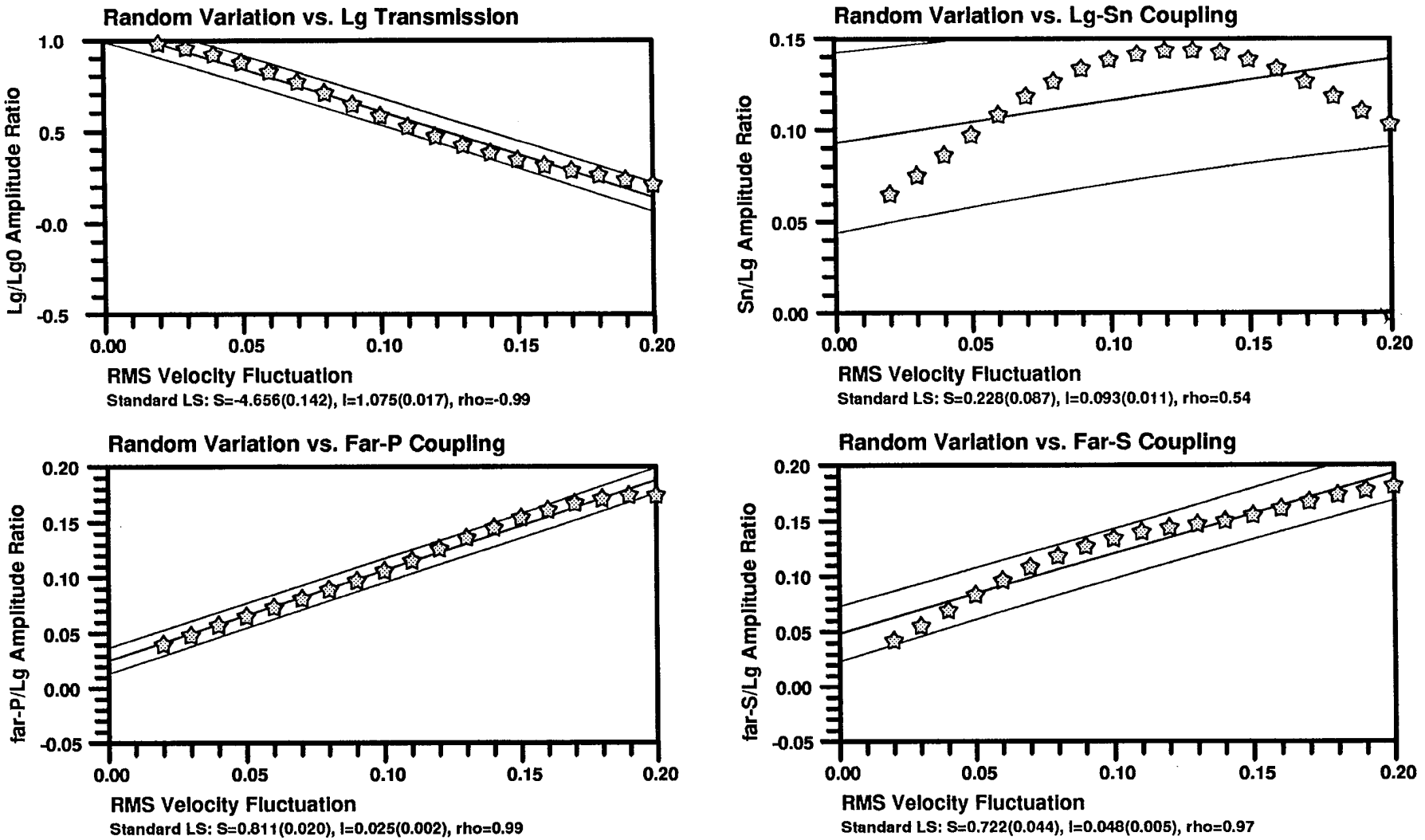

Figure 68. Regressing the L_g transmission coefficient (top left), S_n/L_g amplitude ratio (top right), far–P/L_g amplitude ratio (bottom left), and far–S/L_g amplitude ratio (bottom right). As the model becomes more heterogeneous (that is, has a larger RMS velocity variation), the L_g -to-S_n coupling as well as the coupling to teleseismic phases become more prominent.

6. REMARKS ON OBSERVATIONS OF L_g BLOCKAGE AND A MODEL-BASED CORRECTION PROCEDURE

Baumgardt (1991) conducted a thorough observational study of L_g blockage for Soviet explosions recorded at regional or far-regional distances. He documented several examples of partial and complete blockage and carefully related the possible cause of each case to geological and geophysical characteristics along the path. Baumgardt found that in every instance of partial or complete blockage, the great-circle path of L_g between the source and the receiver crosses contained sedimentary basins and adjacent topographic discontinuities. L_g blockage does not seem to relate to variations in total crustal thickness. Blockages result from basins where there are unusually thick sediments, usually in excess of 10 km, where the basin is fully contained and the sediments pinch out at the edges of the basin, and/or where there are topographic inhomogeneities at the edges of the basin. He observed less blockage for events occurring inside sedimentary basins themselves, where the basins are not particularly thick, or where the sediments thin very gradually with distance. Table 4 below summarizes observations of L_g blockage and weakening, along with the possible mechanism that has been proposed.

Table 5 Observed L_g Blockage/Weakening and Proposed Mechanism(s)

Mechanism Proposed	Author(s)	Region Studied
Dramatic thinning of waveguide	Ewing *et al.* (1957)	continent-ocean margin
Pure oceanic paths	Knopoff *et al.* (1979)	Atlantic & Pacific Oceans
Missing granitic layer	Piwinskii (1981)	Caspian Sea
Crustal thickening	Ruzaikin *et al.* (1977)	Himalayan Belt
Variations in crustal thickness (+Q?)	Gregersen (1984)	North Sea Graben
Variations in crustal thickness	Kennett *et al.* (1985)	North Sea Graben
Anelastic attenuation in sediments	Mitchell & Hwang (1987)	U.S.
Scattering by small-scale heterogeneity	Campillo *et al.* (1993)	SW Alpine Range
Scattering by small-scale heterogeneity	Chazalon *et al.* (1993)	Western Pyrenean Range
Scattering from tectonic boundaries	Kadinsky-Cade *et al.* (1981)	Turkish & Iranian Plateaus
Scattering from tectonic boundaries	Ni & Barazangi (1983)	Tibetan Plateau
Scattering from tectonic boundaries	Baumgardt (1985, 1990)	Ural Mountains
Contained thick sedimentary basin	Baumgardt (1991)	Barents Shelf
Contained thick sediments (+low Q?)	Baumgardt (1991)	North Caspian Depression

The importance of understanding crustal waveguide effects on L_g waves has motivated many modeling studies of blockage in recent years (Kennett, 1986a; Maupin, 1989; Regan and Harkrider, 1989; Chazalon *et al.*, 1993; Gibson and Campillo, 1994; and Cao and Muirhead, 1993). Some of these authors suggest that the observed blockage is not straightforward to simulate, and that the unmodeled small-scale random heterogeneity is required to account for the blockage, on top of the large-scale structural (that is, geometrical) variation of the waveguide. Although either low Q or large velocity variation can be invoked to explain the L_g blockage of many paths, we might be able to narrow down the possible mechanisms with some additional diagnostic information. For instance, if a pronounced L_g -to-S_n conversion is observed along with the L_g blockage, then it is likely that the blocking mechanism is not due to low Q.

One the major challenges in monitoring a Comprehensive Test Ban Treaty [CTBT] is discriminating small events at regional distances. Various forms of compressional/shear (P/S) ratios have been proposed and extensively tested as candidate discriminants. In tackling such problems, a better amplitude (or, equivalently, magnitude) scale of the regional phase of interest, with respective path effects carefully accounted for, is definitely useful or sometimes even necessary. Along this line of thought, Jih *et al.* (1995) (and also Jih and Lynnes, 1993) suggest a simple, convenient magnitude scale for L_g :

$$m_{L_g} = 4.0272 - \text{Bias} + \log A(\Delta) + \frac{1}{3}\log(\Delta(\text{km})) + \frac{1}{2}\log[\sin(\frac{\Delta(\text{km})}{111.1(\text{km/deg})})] + \frac{\gamma(\Delta - 10\text{km})}{\ln(10)}, \qquad [5]$$

$$\text{where } \gamma = \frac{\pi \cdot f}{Q \cdot U}, \quad Q(f) = Q_0 \cdot f^{\zeta},$$

Δ is the epicentral distance in km and $A(\Delta)$ is the observed raw L_g amplitude measured in the time domain in μm [microns] at the epicentral distance of Δ km. Or, equivalently,

$$\hat{A}_{L_g} = A(\Delta) \cdot 10^{4.0272 - \text{Bias}} \cdot (\Delta(\text{km}))^{\frac{1}{3}} \cdot [\sin(\frac{\Delta(\text{km})}{111.1(\text{km/deg})})]^{\frac{1}{2}} \cdot e^{\gamma(\Delta - 10\text{km})}. \qquad [5a]$$

The "Bias" term in Eqs. (5) and (5a) is meant to account for the different L_g excitation (relative to m_b). It is set to zero for the Eastern U.S. Thus a seismic source with 1-sec L_g amplitude of 110 μm at 10 km (extrapolated) epicentral distance would correspond to a m_{L_g} of 4.0272 + 2.0414 + 0.3333 - 1.4019 + 0.0000 = 5.000, which has been suggested to be appropriate for both Eastern North America and Semipalatinsk. That is to say, a seismic source in these two regions with m_b 5.0 would have a m_{L_g} approximately the same. Jih *et al.* (1995) suggest use of 0.34 and 0.26 m.u. for the "Bias", respectively, for Pahute Mesa and Novaya Zemlya explosions. For earthquakes in the Iranian Plateau, Nuttli (1980) suggested a bias value of 0.39 m.u., which includes both the bias due to regional tectonics as well the L_g –mb bias due to source type.

If the regionalized γ map is available (such as those in Singh and Herrmann, 1983; Jih and Lynnes, 1993; and many others) a path-specific γ for an arbitrary source-station pair can simply be computed as the weighted sum of the γ_k's of the subregions that the ray path traverses:

$$\gamma = \sum_{k=1}^{K} \gamma_k \cdot \frac{\Delta_k}{\Delta} \cdot \qquad [6]$$

However, it is clear from Eq. (2) that an erroneous path γ would yield a m_{L_g} bias that increases with the distance. Furthermore, this error is independent of the actual source size or the quality of the raw amplitude measured at the recording station. It is *the bias* solely due to inaccurate calibration of the propagation effect. Jih and Lynnes (1993) gave several examples showing how L_g amplitude measurements could be severely biased if a poor estimate of the path γ is used or if the path γ is not used at all. Baumgardt (1995) recently demonstrated that by incorporating a distance-correction term, which is essentially the $e^{\gamma \cdot \Delta}$ in Eq. (5a), into his P_g/L_g ratio computation, a much better discrimination result was obtained. In fact, this is exactly the same reason why Nuttli's (1986, 1988) absolute yield estimates of underground nuclear explosions using path-corrected m_{L_g} are good.

The seismic discrimination problem is actually intertwined with the source-size determination problem, despite the misperception that the estimation of source size in general (and the estimation of explosive yield in particular) may no longer be as important in the CTBT context. P/S-ratio-based discrimination is a procedure to discern differences in energy partitioning among phases and among frequency bands. Miscellaneous amplitude measurements needed to identify the event are actually reflecting different parts of the focal sphere and/or frequency contents of the seismic source itself. These parameters are often obscured by the path effects. Thus, a better path-calibration procedure would always benefit the discrimination, for just the same reason it would benefit the source-size determination.[2]

In a situation where some geometrical blockage occurs along the path, that is, there is a major structural variation along the path, it may be possible to further refine Eq. (5). As an example, the $\gamma \cdot (\Delta - 10\text{km})/\ln(10)$ term for the path from Novaya Zemlya to KEV can be broken down into $\gamma_1 \cdot (\Delta_1 - 10\text{km})/\ln(10) + \gamma_2 \cdot \Delta_2/\ln(10)$, where $\gamma_2 = 0.0052$ (that is, $Q_0 = 185$; see the model 0D in Table 2), Δ_2 is the lateral span of the Terrigenous Sediments (Baumgardt, 1991), and γ_1 is the average L_g attenuation along the great-circle path excluding the sedimentary segment. Obviously it is necessary to acquire relevant geological and geophysical information along the path before applying this model-based correction.

[2] See discussion in Dainty (1995) and Blandford *et al.* (1992).

7. DISCUSSION AND CONCLUSIONS

An accurate prediction of the regional phases in areas of high proliferation concern requires a decent understanding of the attenuation and scattering mechanisms along the propagation paths. Synthetic data have been of great benefit in gaining physical insight into discriminants, and may be the only means of evaluating evasion scenarios. Synthetic seismograms are particularly useful for regions where earthquake or explosion data are not available. There is no doubt that both geometrical blockage (due to large-scale lateral structural variation), intrinsic attenuation, and small-scale random heterogeneity in the crust affect L_g propagation. But it is often very difficult to separate these effects observationally. Again, numerical modeling could be the only means to quantitatively identify the respective roles played by these factors.

In this study, the two-dimensional LFD method has been used to model the propagation and scattering of L_g waves in a suite of crustal models, including rough interfaces, rugged free-surface topography, and embedded thick sedimentary layers. Two non-standard techniques have been specifically developed for this study: [1] a pure L_g wave packet (for triggering LFD calculations), and [2] a crude, causal attenuation operator. The pure L_g wave packet is injected into a stratified portion of the grid as the reference initial condition to trigger all LFD calculations. This is a natural extension of Jih's (1993b) work on R_g to L_g problems. In addition to those commonly recognized advantages of LFD method, another obvious advantage of this approach is that the effect due to different types of heterogeneity on the seismic phase of interest can be isolated and evaluated easily. The other tool tested in this study is a new attenuation operator suitable for time-domain numerical calculations. As a crude approximation, it applies to only a narrow band within which it gives a nearly frequency-independent γ, as expected. The most notable advantage is its simplicity to implement. Furthermore, it is a causal operator which, at least conceptually, is more realistic. Overall it appears to perform reasonably well. Major observations made with LFD calculations are summarized in the following:

Early L_g: The Moho uplift, which is common in models of the "A" and "F" series, breaks down the L_g waveguide and causes L_g-to-S_n coupling at the ascending interface. When the converted S_n waves encounter the descending Moho of these models, some energy penetrates the interface again, either as a leg of S_n or as converted L_g. The Moho uplift in "F"-series models is not as dramatic as in "A"-series models. Nevertheless, both the L_g-to-S_n and possibly S_n-to-L_g conversions are still apparent. The early L_g observed for paths from Novaya Zemlya to Scandinavia can be explained with this mechanism. The fact that L_g can be excited at continental margins from oceanic S_n conversion has long been observed and reported (for example, Isacks and Stephens, 1975).

Late L_g and longer coda waves: The sedimentary layer, which is present in all "C"-series models and some of "D" and "F" models, is the apparent cause of late L_g arrivals. For models 0Db, 0Fb and 0Fc, the uppermost soft layer causes strong reverberations as well as a very strong L_g-to-R_g conversion. By seismic reciprocity, there should be some structures that would cause strong R_g-to-L_g conversion. Part of this issue has been addressed in Jih (1995). Regarding the coda decay rate, intrinsic attenuation and scattering (particularly, that by random heterogeneity) appear to have different effects. Increased scattering attenuation causes more energy to be distributed into the coda from the direct phase with increasing time. On the other hand, increased intrinsic attenuation entails a greater loss of elastic energy with time from both the coda and the direct wave. This observation can be verified by comparing synthetic seismograms in Figures 61 and 67, and is in agreement with Frankel and Wennerberg (1987).

S_n excitation and S_n/L_g ratios: Except for models 00, 2, 2a, 3, 3a, 0C, 0Ca, and 0Cb, all other models excite significant S_n waves through the L_g-to-S_n conversion. A thick sedimentary layer by itself does not necessarily cause strong L_g-to-S_n conversion. Models of the "C"-series are such examples. However, if the thick sediment layer is contained, such as in models of "D" series, then some S_n waves can be generated at the pinched interface. Models with irregular Moho topography generate S_n with a different mechanism, as discussed above. Most models excite converted S_n waves in the forward direction. Hoever, models 0A and 0B also excite some S_n in the backward direction. The extremely large S_n/L_g ratio associated with models 0E, 0Ea, and 0Ec (all with a thickened crust) offers an excellent demonstration for the observation Ruzaikin *et al.* (1977) made.

Topographic relief: Models with a mild free-surface topography alone (for example, models 2 and 3) generate a relatively weak L_g-to-S_n conversion comparable to that of "C" models. Comparing the synthetics in Figures 55 and 58, it appears that the transmitted L_g wave trains of models with mild mountainous topography are very similar to those of the reference model 00. In fact, these mountainous models and models with weak random heterogeneity as well as anelastic models would stand out among all models in that the checkerboard-like interference pattern of the original L_g wave train is (somewhat) retained (see Figures 45, 49, 59, and 62). This is very different from the case of R_g for which the rugged free-surface topography is shown to be a strong scatterer (Jih, 1993b, 1995).

Lg to Pg conversion: All models of the "F" series exhibit significant L_g-to-P_g conversion. The peak horizontal amplitude on trace No. 25 ranges from 10 to 15 percent of that of the original L_g wave train. To a lesser extent, models of "C" and "D" series as well as models 0A and 0Ba also generate the same conversion.

Coupling to teleseismic phases: For mountainous models, L_g-to-S is twice as strong as L_g-to-P. For the "A" and "B" series of models, as well as the random media, these two mechanisms are

about equally strong. For anelastic models and "C"-type models, L_g -to-S is weaker than the L_g -to-P, whereas models of the "D", "E", and "F" series show the opposite trend (Table 2).

Lg blockage: Both abrupt changes in the Moho topography and a thick contained sedimentary layer can cause strong L_g -to-S_n conversions. The physical mechanisms underlying the conversion are different for these two structures, however. The early L_g observed for paths from Novaya Zemlya island to Scandinavia is illustrated with LFD calculations. Alluvial basin structures cause strong reverberations as well as very strong L_g -to-R_g conversions. Valley structures with large depth to width ratios and large velocity contrast with the substrate support very large amplitude lateral resonance modes. If we invoke the principle of seismic reciprocity, R_g -to-L_g conversion could be an important mechanism of L_g excitation for certain structures. Recent observational study by Patton and Taylor (1995) suggests that this is the case, at least for Yucca Flat explosions.

Other than major structural discontinuities in the crustal waveguide, both anelasticity and small-scale random heterogeneity can also contribute to the so-called "L_g blockage". For instance, an RMS velocity variation of 8 percent in the whole crust is equivalent to a $Q_0(L_g)$ of about 270, which would be sufficient to reduce the peak amplitude of 1Hz L_g waves by 30 percent for every 100 km they traverse. The classical example of an L_g -blocking path between Novaya Zemlya and northern Scandinavia has a $Q_0(L_g)$ about 252 and could be modeled with an RMS velocity variation of 8 percent alone.

Unlike R_g waves, L_g propagation is not affected by a moderate free-surface topography alone as much as other types of heterogeneity. Topographic relief has been shown to be a very strong scatterer for the R_g phase (Jih, 1993b, 1995). This is because R_g energy is confined in the uppermost layer. The energy of L_g is evenly distributed in the crust, and the surface topography variations are generally small relative to the crustal thickness. Thus it may be expected that the topographic variations alone should have relatively weaker influence on L_g propagation, as compared to R_g. This is illustrated with models 2 and 3 of this study. However, the topography may reflect the crustal thickness through isostasy. Zhang and Lay (1994) suggest that S_n/L_g ratios may be correlated to some roughness measures of the paths, based on a limited data set. LFD appears to be the ideal tool to test the existence of any correlation between some roughness measure and the propagation characteristics of regional phases, as demonstrated with the very few mountainous models tested in this study. Similar statistical analysis should also be conducted to examine the effects of water column, random Moho topography, and irregular intra-crustal interfaces, as well as the combination of all these factors.

REFERENCES

Bache, T. C., H. Swanger, and B. Shekoller (1981). *Synthesis of L_g in Eastern Uhited States crustal models with frequency independent Q,* Report SSS-R-81-4668. S-Cubed, La Jolla, CA.

Baumgardt, D. R. (1985), Comparative analysis of teleseismic P coda and L_g waves from underground nuclear explosions in Eurasia: *Bull. Seism. Soc. Am.,* **75,** 1413-1434.

Baumgardt, D. R. (1991). *High frequency array studies of long range L_g propagation and the causes of L_g blockage and attenuation in the Eurasian continental craton,* Report PL-TR-91-2059(II), Phillips Laboratory, Hanscom AFB, MA (ADA 236984).

Baumgardt, D. R. (1995). Cross region analysis, path corrections and the transportability of regional seismic discriminants, in *Proceedings of 17th PL/AFOSR Seismic Research Symposium* (12-15 Sept 1995, Scottsdale, AZ; J. Lewkowicz, J. McPhetres, and D. Reiter eds.), *Report PL-TR-95-2108,* Phillips Laboratory, Hanscom AFB, MA, pp. 27-35.

Blandford, R. R. (1981). Seismic discrimination problems at regional distances, in *Identification of Seismic Sources - Earthquake or Underground Explosion,* (E. S. Husebye and S. Mykkeltveit, eds.), D. Reidel Publishing Co., Dordrecht, The Netherlands, 695-740.

Blandford, R. R., A. Dainty, R. Lacoss, R. Maxion, A. Ryall, B. Stump, C. Thurber, and T. Wallace (1992). *Report on the DARPA Seismic Identification Workshop,* DARPA/NMRO Special Topical Report, 28 pp.

Boore, D. (1970). Love waves in nonuniform wave guides: finite-difference calculations, *J. Geophy. Res.,* **75,** 1512-1527,

Bouchon, M. (1982). The complete synthesis of seismic crustal phases at regional distances, *J. Geophys. Res.,* **87,** 1735-1741.

Campillo, M., B. Feignier, M. Bouchon, and N. Bethoux (1993). Attenuation of crustal waves across the Alpine range, *J. Geophys. Res.,* **98,** 1987-1996.

Campillo, M., M. Bouchon, and B. Massinon (1984). Theoretical study of the excitation, spectral characteristics, and geometrical attenuation of regional seismic phases, *Bull. Seism. Soc. Am.,* **74,** 79-90.

Cao, S. and K. J. Muirhead (1993). Finite difference modeling of L_g blockage, *Geophys. J. Int.,* **115,** 85-96.

Cerjan, C., D. Kosloff, R. Kosloff, and M. Reshef (1985). A nonreflecting boundary condition for discrete acoustic and elastic wave equations, *Geophysics,* **50,** 705-708.

Chazalon, A., M. Campillo, R. Gibson, and E. Garnero (1993). Crustal wave propagation anomaly across the Pyrenean Range - comparison between observations and numerical simulations, *Geophys. J. Int.,* **115,** 829-838.

Dainty, A. M. (1981). A scattering model to explain seismic Q observations in the Lithosphere between 1 and 30 Hz, *Geophys. Res. Let.,* **8-11,** 1126-1128.

Dainty, A. M. (1995). The influence of seismic scattering on monitoring, in *"Monitoring a Comprehensive Test Ban Treaty"* (E. S. Husebye and A. M. Dainty (eds), NATO ASI Series E: Applied Sciences, Vol. 303, pp.663-688, Kluwer Academic Press, Dordrecht, The Netherlands.

Day, S. M. and J. B. Minster (1984). Numerical simulation of wavefields using a Pade approximation method, *Geophys. J. R. Astr. Soc.*, **78,** 105-118.

Emmerich, H. and M. Korn (1987). Incorporation of attenuation into time-domain computation of seismic wave fields, *Geophysics,* **52,** 1252-1264.

Ewing, M., W. S. Jardetsky, and F. Press (1957). *Elastic Waves in Layered Media,* McGraw Hill, New York.

Frankel, A. and R. W. Clayton (1986). Finite-difference simulation of seismic scattering: implications for the propagation of short-period seismic waves in the crust and models of crustal heterogeneity, *J. Geophys. Res.*, **91,** 6465-6489.

Frankel, A. and L. Wennerberg (1987). Energy-flux model of seismic coda: separation of scattering and intrinsic attenuation, *Bull. Seism. Soc. Am.*, **77,** 1223-1251.

Fuyuki, M. and Y. Matsumoto (1980). Finite-difference analysis of Rayleigh wave scattering at a trench, *Bull. Seism. Soc. Am.*, **70**, 2051-2069.

Fuyuki, M. and M. Nakano (1984). Finite-difference analysis of Rayleigh wave transmission past an upward step change, *Bull. Seism. Soc. Am.*, **74,** 893-911.

Gibson, R. and M. Campillo (1994). Numerical simulation of high- and low-frequency L_g -wave propagation, *Geophys. J. Int.*, **118,** 47-56.

Gregersen, S. (1984). L_g -wave propagation and crustal structure differences near Denmark and the North Sea, *Geophys. J. R. Astr. Soc.*, **79,** 217-234.

Hansen, R. A., Ringdal, F. and P. G. Richards (1990). The stability of RMS Lg measurements and their potential for accurate estimation of yields of Soviet underground nuclear explosions, *Bull. Seism. Soc. Am.*, **80**, 2106-2126.

Herrmann, R. B. (1987). *Computer Programs in Seismology,* Volume IV, Saint Louis Univ., Saint Louis, MO.

Isacks, B. L. and C. Stephens (1975). Conversions of S_n to L_g at continental margin, *Bull. Seism. Soc. Am.*, **65,** 235-244.

Jacobson, R. S. (1987). An investigation into the fundamental relationship between attenuation, phase dispersion, and frequency using seismic refraction profiles over sedimentary structures, *Geophysics,* **52,** 72-87.

Jih, R.-S. (1993a). *User's manual of FD2: a software package for modeling seismological problems with 2-dimensional linear finite-difference method,* Report TGAL-93-06, Teledyne Geotech, Alexandria, VA.

Jih, R.-S. (1993b). *Statistical characterization of rugged propagation paths with application to R_g scattering study,* Report TGAL-93-07, Teledyne Geotech, Alexandria, VA.

Jih, R.-S. (1994). Numerical modeling of crustal phase propagation in irregular waveguides, in *Proceedings of 16th PL/AFOSR Seismic Research Symposium* (7-9 Sept 1994, Thornwood, NY; J. Cipar, J. Lewkowicz, and J. McPhetres, eds.), *Report PL-TR-94-2217,* Phillips Laboratory, Hanscom AFB, MA, pp. 173-181 (ADA284667).

Jih, R.-S. (1995). Numerical investigation of relative contributions of R_g scattering and attenuation to

L_g excitation, in *Proceedings of 17th PL/AFOSR Seismic Research Symposium* (12-15 Sept 1995, Scottsdale, AZ; J. Lewkowicz, J. McPhetres, and D. Reiter eds.), *Report PL-TR-95-2108,* Phillips Laboratory, Hanscom AFB, MA, pp. 401-410.

Jih, R.-S. (1996). *A simple, causal method to incorporate anelastic attenuation into finite-difference calculations,* Report PL-TR-96-2015, Phillips Laboratory, Hanscom AFB, MA.

Jih, R.-S. and C. S. Lynnes (1993). *Studies of regional phase propagation in Eurasia.* Report PL-TR-93-2003 (=TGAL-93-01), Phillips Laboratory, Hanscom AFB, MA (ADA 262801).

Jih, R.-S. and K. L. McLaughlin (1988). *Investigation of explosion generated SV L_g waves in 2-D heterogeneous crustal models by finite-difference method,* Report AFGL-TR-88-0025 (=TGAL-88-01), Air Force Geophysics Laboratory, Hanscom AFB, MA (ADA 213586).

Jih, R.-S., K. L. McLaughlin and Z. A. Der (1988). Free boundary conditions of arbitrary polygonal topography in a 2-D explicit elastic finite difference scheme, *Geophysics,* **53,** 1045-1055.

Jih, R.-S., R. R. Baumstark, and R. A. Wagner (1995). Simultaneous inversion of event m_{Lg} and path attenuation coefficient with application to a transportable L_g magnitude scaling, in *Proceedings of 17th PL/AFOSR Seismic Research Symposium* (12-15 Sept 1995, Scottsdale, AZ; J. Lewkowicz, J. McPhetres, and D. Reiter eds.), *Report PL-TR-95-2108,* Phillips Laboratory, Hanscom AFB, MA, pp. 411-419.

Kadinsky-Cade, K., M. Barazangi, J. Oliver, and B. L. Isacks (1981). Lateral variations of high-frequency seismic wave propagation at regional distances across the Turkish and Iranian Plateaus, JGR, **86,** 9377-9396.

Kennett, B. L. (1985). On regional *S*, *Bull. Seism. Soc. Am.,* **75,** 1077-1086.

Kennett, B. L. (1986a). L_g waves and structural boundaries, *Bull. Seism. Soc. Am.,* **76,** 1133-1141.

Kennett, B. L. (1986b). Wavenumber and wavetype coupling in laterally heterogeneous media, *Geophys. J. R. Astr. Soc.,* **87,** 313-331.

Kennett, B. L. (1989a). On the nature of regional seismic phases - I. Phase representations for P_n, P_g, S_n, L_g, *Geophys. J.,* **98,** 447-456.

Kennett, B. L. (1989b). L_g -wave propagation in heterogeneous media, *Bull. Seism. Soc. Am.,* **79,** 860-872.

Kennett, B. L. N., S. Gregersen, S. Mykkeltveit, and R. Newmark (1985). Mapping of crustal heterogeneity in the North Sea Basin via the propagation of L_g waves, *Geophys. J. R. Astr. Soc.,* **83,** 299-306.

Knopoff, L., F. Schwab, and E. Kausel (1973). Interpretation of L_g, *Geophys. J.,* **33,** 398-404.

Knopoff, L., R. G. Mitchel, E. G. Kausel, and F. Schwab (1979). A search for the oceanic L_g phase, *Geophys. J. Roy. Astr. Soc.,* **56,** 211-218.

Levander, A. (1985). Finite-difference calculations of dispersive Rayleigh wave propagation, *Tectonophysics,* **113,** 1-30.

Levshin, A. and K. A. Berteussen (1979). Anomalous propagation of surface waves in the Barents Sea as inferred from NORSAR recordings, *Geophys. J. R. Astr. Soc.,* **56,** 97-118.

Lynnes, C. S. and R. Baumstark (1991). *Phase and spectral ratio discrimination in North America,* Report PL-TR-91-2212(II) (=TGAL-91-06), Phillips Laboratory, Hanscom AFB, MA (ADA 246673).

Martel, L., M. Munasinghe, and G. W. Farnell (1977), Transmission and reflection of Rayleigh wave through a step, *Bull. Seism. Soc. Am.,* **67,** 1277-1290.

Maupin, V. (1989). Numerical modeling of L_g wave propagation across the North Sea central graben, *Geophys. J. Int.,* **99,** 273-283.

McLaughlin, K. L. and L. M. Anderson (1987). Stochastic dispersion of short-period P waves due to scattering and multipathing, *Geophys. J. R. Astr. Soc.,* **89-3,** 933-963.

McLaughlin, K. L. and R.-S. Jih (1986). *Finite-difference simulations of Rayleigh wave scattering by 2-D rough topography,* Report AFGL-TR-86-0269 (=TGAL-86-09), Air Force Geophysics Laboratory, Hanscom AFB, MA (ADA 179190).

McLaughlin, K. L. and R.-S. Jih (1987). *Finite-difference simulations of Rayleigh wave scattering by shallow heterogeneity,* Report AFGL-TR-87-0322 (=TGAL-87-02), Air Force Geophysics Laboratory, Hanscom AFB, MA (ADA 194961).

Mitchell, B. J. and H. J. Hwang (1987). Effect of low Q sediments and crustal Q on Lg attenuation in the United States, *Bull. Seism. Soc. Am.,* **77,** 1197-1210.

Munasinghe, M. and G. Farnell (1973). Finite-difference analysis of Rayleigh wave scattering at vertical discontinuities, *J. Geophys. Res.,* **78,** 2454-2466.

Ni, J., and M. Barazangi (1983). High-frequency seismic wave propagation beneath the Indian Shield, Himalayan Arc, Tibetan Plateau, and surrounding regions: high uppermost mantle velocities and efficient S_n propagation beneath Tibet, *Geophys. J. R. Astr. Soc.,* **72,** 665-689.

Nuttli, O. W. (1980). The excitation and attenuation of seismic crustal phases in Iran, *Bull. Seism. Soc. Am.,* **70,** 469-485.

Nuttli, O. W. (1986). Yield estimates of Nevada Test Site explosions obtained from seismic L_g waves, *J. Geophys. Res.,* **91,** 2137-2151.

Nuttli, O. W. (1988). L_g magnitudes and yield estimates for underground Novaya Zemlya nuclear explosions, *Bull. Seism. Soc. Am.,* **78,** 873-884.

Oliver, J. and M. Ewing (1957). Higher modes of continental Rayleigh waves, *Bull. Seism. Soc. Am.,* **47,** 187-204.

Patton, H. J. (1988). Application of Nuttli's method to estimate yield of Nevada Test Site explosions recorded on Lawrence Livermore National Laboratory's digital seismic system, *Bull. Seism. Soc. Am.,* **78,** 1759-1772.

Patton, H. J. and S. R. Taylor (1995). Analysis of L_g spectral ratios from NTS explosions: implications for the source mechanisms of spall and the generation of L_g waves, *Bull. Seism. Soc. Am.,* **85,** 220-236.

Piwinskii, A. J. (1981). *Deep structure of the earth's crust and upper mantle in the USSR according to geological, geophysical, and seismological data: Dneiper-Donetsk and PriCaspian depressions,* Report UCID-19203, Lawrence Livermore Laboratory, Livermore, CA.

Pomeroy, P. W., W. J. Best, and T. V. McEvilly (1982). Test ban treaty verification with regional data --

a review, *Bull. Seism. Soc. Am.*, **72,** S89-S129.

Press, F. and M. Ewing (1952). Two slow surface waves across North America, *Bull. Seism. Soc. Am.*, **42,** 219-228.

Regan, J. and D. G. Harkrider (1989). Numerical modeling of *SH* L_g waves in and near continental margins, *Geophys. J. Int.*, **98,** 107-130.

Ricker, N. H. (1977). *Transient Waves in Visco-elastic Media,* Elsevier Scientific Publishing Co., New York, NY.

Ruzaikin, A. I., I. L. Nersesov, V. I. Khalturin, and P. Molnar (1977). Propagation of L_g and lateral variation in crustal structure in Asia, *J. Geophys. Res.*, **82,** 307-316.

Savarrensky, E. and N. Valdner (1960). Observations of L_g and R_g waves from the Black Sea basin earthquakes, *Ann. Geofis.*, **13,** 129-134.

Singh, S. and R. B. Herrmann (1983). Regionalization of crustal coda Q in the continental United States, *J. Geophys. Res.*, **88,** 527-538.

Toksoz, M. N., A. M. Dainty, and E. E. Charrette (1986). *Development of ultrasonic modeling techniques for the study of seismic wave scattering due to crustal inhomogeneities,* Report AFGL-TR-86-0078, Air Force Geophysics Laboratory, Hanscom AFB, MA (ADA 170062).

Vidale, J. and D. V. Helmberger (1988). Elastic finite-difference modeling of the 1971 San Fernando, California, earthquake, *Bull. Seism. Soc. Am.*, **78,** 122-141.

Zhang, T. and T. Lay (1994). Analysis of short-period regional phase path effects associated with topography in Eurasia, *Bull. Seism. Soc. Am.*, **84,** 119-132.

DISTRIBUTION LIST

NON-GOVERNMENT RECIPIENTS

Prof. Thomas Ahrens
Prof. Donald V. Helmberger
Dr. Larry J. Burdick
Division of Geology & Planetary Sciences
California Institute of Technology
Pasadena, CA 91125 (3 copies)

Prof. Shelton Alexander
Prof. Charles A. Langston
Geosciences Department
403 Deike Building
The Pennsylvania State University
University Park, PA 16802 (2 copies)

Dr. Thomas C. Bache, Jr.
Dr. Thomas J. Sereno, Jr.
Dr. Jeffrey W. Given
Science Applications Int'l Corp.
10260 Campus Point Drive
San Diego, CA 92121 (3 copies)

Dr. Douglas R. Baumgardt, Dr. Zoltan A. Der
ENSCO, Inc.
5400 Port Royal Road
Springfield, VA 22151 (2 copies)

Dr. Eric P. Chael, Dr. Dale Breding
Dr. Larry S. Walker, Dr. Gary Mauth
Sandia National Laboratory
Division 9241
Albuquerque, NM 87185 (4 copies)

Dr. Theodore Cherry
Science Horizons, Inc.
710 Encinitas Blvd, Suite 200
Encinitas, CA 92024

Prof. Steven M. Day
Dept. of Geological Sciences
San Diego State University
San Diego, CA 92182

Dr. Mark D. Fisk
Mission Research Corporation
735 State Street
P.O. Drawer 719
Santa Barbara, CA 93102

Prof. Cliff Frolich, Dr. Lian-She Zhao
Institute of Geophysics
8701 North Mopac
Austin, TX 78759 (2 copies)

Ms. Lori Grant
Multimax, Inc.
311-C Forest Avenue, Suite 3
Pacific Grove, CA 93950

Prof. Henry L. Gray, Prof. Gary McCartor
Dept. of Physics
Southern Methodist University
Dallas, TX 75275 (2 copies)

Dr. Indra N. Gupta
Multimax, Inc.
1441 McCormick Drive
Landover, MD 20785

Dr. Richard A. Gustafson, Dr. Robert North
Dr. Jerry Carter
Center for Monitoring Research
1300 North 17th Street, Suite 1450
Arlington, VA 22209-2308 (4 copies)

Dr. Willard J. Hannon
Lawrence Livermore National Laboratory
P.O. Box 808
Livermore, CA 94550

Prof. David G. Harkrider
Boston College @ PL/GPE
29 Randolph Road
Hanscom AFB, MA 01731

Prof. Eugene T. Herrin, Jr.
Geophysical Laboratory
Southern Methodist University
Dallas, TX 75275

Prof. Robert B. Herrmann
Prof. Brian J. Mitchell
Dept. of Earth & Atmospheric Sciences
St. Louis University
St. Louis, MO 63156 (2 copies)

Prof. Bryan Isacks, Prof. Muawia Barazangi
Dept. of Geological Sciences
SNEE Hall
Cornell University
Ithaca, NY 14850 (2 copies)

Prof. Lane R. Johnson
Prof. Thomas V. McEvilly
Seismographic Station
University of California
Berkeley, CA 94720 (2 copies)

Prof. Thomas H. Jordan
Dept. of Earth, Atmospheric
and Planetary Sciences
Massachusetts Institute of Technology
Cambridge, MA 02139

Prof. Thorne Lay, Prof. Susan Schwartz
Institute of Tectonics
University of California, Santa Cruz
Santa Cruz, CA 95064 (2 copies)

Dr. Randolph Martin, III
New England Research , Inc.
76 Olcott Drive
White River Junction, VT 05001

Dr. Keith L. McLaughlin
Dr. Jeffrey L. Stevens
Dr. Terrance G. Barker
Maxwell Laboratories, S-Cubed Division
P.O. Box 1620
La Jolla, CA 92038 (3 copies)

Mr. John R. Murphy, Dr. Theron J. Bennett
Maxwell Laboratories, S-Cubed Division
11800 Sunrise Valley Drive, Suite 1212
Reston, VA 22091 (2 copies)

Dr. Dan N. Hagedorn, Dr. Ray Warner
Pacific Northwest Laboratories
Battelle Boulevard
Richland, WA 99352 (2 copies)

Prof. John A. Orcutt, Prof. Bernard Minster
Prof. Freeman Gilbert
IGPP, A-025
Scripps Institute of Oceanography
University of California, San Diego
La Jolla, CA 92093 (3 copies)

Dr. Jay J. Pulli
Radix Systems, Inc.
6 Taft Court
Rockville, MD 20850

Prof. Paul G. Richards, Prof. Lynn R. Sykes
Prof. William Menke, Prof. Arthur Lerner-Lam
Prof. David G. Simpson
Lamont-Doherty Earth Observatory
of Columbia University
Palisades, NY 10964 (6 copies)

Dr. Chandan K. Saikia, Dr. Bradley B. Woods
Woodward-Clyde Consultants
566 El Dorado Street
Pasadena, CA 91109-3245 (2 copies)

Prof. Charles G. Sammis, Prof. Keiichi Aki
Center for Earth Sciences
University of Southern California
University Park
Los Angeles, CA 90089 (2 copies)

Dr. Brian W. Stump, Dr. Steven R. Taylor,
Dr. Wendee Brunish, Dr. Mark Hodgson
Dr. Fredrick N. App, Dr. James R. Kamm
Los Almos National Laboratory
EES-3, MS C-335
Los Almos, NM 87545 (6 copies)

Prof. Clifford Thurber, Prof. Robert P. Meyer
University of Wisconsin-Madison
Dept. of Geology & Geophysics
1215 West Dayton Street
Madison, WS 53706 (2 copies)

Prof. M. Nafi Toksöz, Dr. William Rodi
Dr. Richard L. Gibson, Dr. Yingping Li
Earth Resources Laboratory
Mass. Institute of Technology
42 Carleton Street
Cambridge, MA 02142 (4 copies)

Verification Program
Attn: Dr. Jay Zucca
Lawrence Livermore National Laboratory
P.O. Box 808, L205
Livermore, CA 94550 (12 copies)

Prof. Terry C. Wallace, Prof. Susan L. Beck
Dept. of Geosciences/SASO
University of Arizona
Tucson, AZ 85721 (2 copies)

U.S. GOVERNMENT AGENCIES

DARPA/OASB/Librarian
3701 N. Fairfax Drive
Arlington, VA 22303-1714

Dr. Ralph W. Alewine, III
Dr. Steven R. Bratt
Nuclear Treaty Programs Office
Rosslyn Gateway
1901 N. Moore Street, Suite 609
Arlington, VA 22209 (2 copies)

Dr. Robert R. Blandford
AFTAC/TT, Center for Monitoring Research
1300 N. 17th Street, Suite 1450
Arlington, VA 22209

Defense Technical Information Center
8725 John J. Kingman Road
Fort Belvoir, VA 22060-6218 (2 copies)

Dr. Anton W. Dainty, Dr. John J. Cipar
Dr. Katharine Kadinsky-Cade, Mr. Rong-Song Jih
Earth Sciences Division (PL/GPE)
Phillips Lab./ Geophysics Directorate
Hanscom AFB, MA 01731 (4 copies)

Dr. Stanley K. Dickinson
AFOSR/NM
110 Duncan Avenue, Suite B115
Bolling AFB
Washington, DC 20331-6448

Dr. Dale Glover
U.S. DIA/DT-1B
Washington, DC 20301

HQ AFTAC/CA
(STINFO)
1030 South Highway A1A
Patrick AFB, FL 32925-6001

HQ AFTAC/TTR
1030 South Highway A1A
Patrick AFB, FL 32925-6001 (12 copies)

HQ AFTAC/TTD
1030 South Highway A1A
Patrick AFB, FL 32925-6001 (3 copies)

Dr. Max Koontz, Dr. Joan B. Rohlfing
Dr. Leslie A. Casey, Dr. Stan Rudnick
U.S. Dept. of Energy/NN-20
Forrestal Building
1000 Independence Avenue
Washington, DC 20585 (4 copies)

Dr. Leonard E. Johnson
National Science Foundation
Division of Earth Sciences
4201 Wilson Boulevard, Suite 785
Arlington, VA 22230

Dr. William S. Leith
Mr. John Rodney Matzko
U.S. Geological Survey
920 National Center
Reston, VA 22092 (2 copies)

Mr. James F. Lewkowicz
Dr. Delaine T. Reiter, Mrs. Jeanne M. McPhetres
Earth Sciences Division (PL/GPE)
Phillips Lab/Geophysics Directorate
Hanscom AFB, MA 0l73l (5 copies)

Dr. Don A. Linger, Dr. Michael Shore
U.S. DNA
6801 Telegraph Road
Alexandria, VA 22310 (2 copies)

Dr. Robert P. Massé
Denver Federal Center
Box 25046, Mail Stop 967
Denver, CO 80225

Office of the Secretary of Defense
DDR&E
Washington, DC 20330

Dr. Frank F. Pilotte
HQ AFTAC/TT
1030 South Highway A1A
Patrick AFB, FL 32925-6001

Phillips Laboratory / TL
5 Wright Street
Hanscom AFB, MA 01731

Phillips Laboratory
PL/SUL
3550 Aberdeen Avenue, SE
Kirtland AFB, NM 87117 (2 copies)

Phillips Laboratory
PL/XPG
Hanscom AFB, MA 01731

Dr. Robert E. Reinke
Field Command, DNA
FCDNA/FCTTS
1680 Texas Street, S.E.
Kirtland AFB, NM 87117-6008

Secretary of the Air Force
(SAFRD)
Washington, DC 20330

Dr. Owen J. Sheaks
Dr. William Roggenthen
Mr. Alfred Lieberman
Mr. Richard J. Morrow
Ms. Mona Dreicer
U.S. ACDA
320 21st Street NW
Washington, DC 20451 (5 copies)

Dr. Lawrence S. Tumbull, Jr.
Dr. John R. Filson
Katie Poley
Sean H. Doran
U.S. ACIS
Washington, DC 20505 (4 copies)

Center for Verification Research
Technical Library
P.O. Box 1148
8500 Cinder Bed Road
Newington, VA 22122-9998

OTHER RECIPIENTS

Dr. Don Albert
Lt. Col. Dick Jardine
U.S. ACRREL
72 Lyme Road
Hanover, NH 03755 (2 copies)

Dr. David M. Boore
Dr. Leif G. Wennerberg
Dr. Bernard A. Chouet
U.S. Geological Survey
345 Middlefield Road, MS 977
Menlo Park, CA 94025 (3 copies)

Dr. Arthur Frankel
U.S. Geological Survey
Denver Federal Center
Denver, CO 80225

Dr. Richard Lewis
Earthquake Engineering & Geophysics
U.S. Army Corps of Engineers
P.O. Box 631
Vicksburg, MS 39180

Dr. Ed McDonald
Naval Research Laboratory
4555 Overlook Avenue, SW
Washington, DC 20375

Mr. James Anderson, Mr. Rick Perez
Teledyne Brown Engineering
2111 Wilson Boulevard, Suite 900
Arlington, VA 22201-3058 (2 copies)

Prof. Charles B. Archambeau
Prof. Danny J. Harvey, Dr. Anatoli L. Levshin
University of Colorado, JSPC
Campus Box 583
Boulder, CO 80309 (3 copies)

Dr. Ralph J. Archuleta
Dept. of Geological Sciences
University of California at Santa Barbara
Santa Barbara, CA 93102

Dr. Jonathan Berger, Dr. Frank Vernon
Dr. Holly K. Given, Dr. Peter Davis
IGPP, A-025
Scripps Institute of Oceanography
University of California, San Diego
La Jolla, CA 92093 (4 copies)

Dr. G. A. Bollinger
Dept. of Geological Sciences
Virginia Polytechnic Institute
21044 Derring Hall
Blacksburg, VA 24061

Prof. Bruce A. Bolt
Prof. Barbara Romanowicz
Seismographic Station
475 McCone Hall
University of California
Berkeley, CA 94720 (2 copies)

Prof. Jon F. Claerbout
Dept. of Geophysics
Stanford University
Stanford, CA 94305

Prof. Robert W. Clayton
Seismological Laboratory
Division of Geological & Planetary Sciences
California Institute of Technology
Pasadena, CA 91125

Prof. Vernon F. Cormier
Dept. of Geology & Geophysics
University of Connecticut
Storrs, CT 06269-2045

Prof. Paul M. Davis, Prof. John Vidale
Dept. Earth & Space Sciences
University of California (UCLA)
Los Angeles, CA 90024 (2 copies)

Prof. Adam Dziewonski
Prof. Göran Ekström
Prof. James R. Rice
Hoffman Laboratory
Harvard Uninversity
20 Oxford Street
Cambridge, MA 02138 (3 copies)

Ronald W. Ewing
Ewing Associates
11535 Clara Barton Drive
Fairfax Station, VA 22039

Prof. John Ferguson
Prof. George McMechan
Center for Lithospheric Studies
University of Texas at Dallas
P.O. Box 688
Richardson, TX 75083-0688 (2 copies)

Prof. Stanley Flatté
Applied Sciences Building
University of California
Santa Cruz, CA 95064

Dr. Alexander Florence, Dr. Stephen Miller
SRI International
333 Ravenswood Avenue
Menlo Park, CA 94025-3493 (2 copies)

Dr. Bengt Fornberg
Exxon Engineering & Research Company
Clinton Township, Route 22 East
Annandale, NJ 08801

Prof. Donald Forsyth
Dept. of Geological Sciences
Brown University
Providence, RI 02912

Dr. Roger Fritzel
Pacific Sierra Research
1401 Wilson Blvd., Suite 1100
Arlington, VA 22209

Dr. Ivan Henson
Multimax, Inc.
1290 Highway A1A, Suite 206
Satellite Beach, FL 32937

Dr. Kevin Hutchenson
ENSCO, Inc.
445 Pineda Court
Melbourne, FL 32940

Prof. Alan Kafka, Prof. John Ebel
Dept. of Geology & Geophysics
Boston College
Chestnut Hill, MA 02167 (2 copies)

Dr. Cyrus P. Knowles
JAYCOR
1608 Spring Hill Road
Vienna, VA 22182

Prof. Leon Knopoff
University of California
Institute of Geophysics & Planetary Physics
Los Angeles, CA 90024

Dr. Richard LaCoss
MIT-Lincoln Laboratory
M-200B
P.O. Box 73
Lexington, MA 02173-0073

Prof. Fred K. Lamb
University of Illinois
Dept. of Physics
1110 West Green Street
Urbana, IL 61801

Dr. James Lawson
Oklahoma Geological Survey
P.O. Box 8
Leonard, OK 74043

Prof. Alan R. Levander
Dept. of Geology & Geophysics
Rice University, MS 126
Houston, TX 77005

Dr. J. Michael McKisic
Tracor Applied Sciences, Inc.
1601 Research Boulevard
Rockville, MD 20850

Dr. George Mellman
Sierra Geophysics
11255 Kirkland Way
Kirkland, WA 98033

Prof. James Ni, Prof. Thomas Hearn
Dept. of Physics
New Mexico State University
Las Cruces, NM 88003 (2 copies)

Prof. Jeffrey Park
Dr. Jonathan Lees
Dept. of Geology & Geophysics
Yale University
P.O. Box 208109
New Haven, CT 06520 (2 copies)

Prof. Robert Phinney
Geological & Geophysical Sciences
Princeton University
Princeton, NJ 08544-0636

Dr. Paul Pomeroy
Rondout Associates
P.O. Box 224
Stone Ridge, NY 12484

Dr. Richard Sailor
TASC, Inc.
55 Walkers Brook Drive
Reading, MA 01867

Prof. G. T. Schuster
Dept. of Geology & Geophysics
University of Utah
Salt Lake City, UT 84112

Prof. R. H. Shumway
Division of Statistics
University of California
Davis, CA 95616

Dr. Gregory E. van der Vink
IRIS, Inc.
1616 North Fort Myer Drive, Suite 1050
Arlington, VA 22209 (2 copies)

Prof. Stewart W. Smith
Prof. Stephen D. Malone
Geophysics AK-50
University of Washington
Seattle, WA 98195 (2 copies)

Prof. Jeremiah Sullivan
University of Illinois at Urbana-Champaign
Dept. of Physics
1110 West Green Street
Urbana, IL 61801

Prof. Pradeep Talwani
Dept. of Geological Sciences
University of South Carolina
Columbia, SC 29208

Prof. Leo T. Teng
University of Southern California
University Park
Los Angeles, CA 90089

Dr. Karl F. Veith
EG&G
2341 Jefferson Davis Highway, Suite 801
Arlington, VA 22202

Dr. William Wortman
Mission Research Corporation
8560 Cinderbed Road, Suite 700
Newington, VA 22122

Prof. Francis T. Wu
Dept. of Geological Sciences
State University of New York, Binghamton
Vestal, NY 13901

FOREIGN RECIPIENTS

Dr. V. V. Adushkin
Dr. I. O. Kitov
Inst. for Dynamics of Geospheres
Russian Academy of Science
Moscow, Russia (2 copies)

Dr. Peter Basham
Earth Physics Branch
Geological Survey of Canada
1 Observatory Crescent
Ottawa, Ontario,CANADA K1A OY3

Prof. Ari Ben-Menahem
Dept. of Applied Mathematics
Weizman Institute of Science
Rehovot, ISRAEL 951729

Dr. Michel Bouchon
I.R.I.G.M.-B.P. 68
38402 St. Martin D'Heres
Cedex, FRANCE

Dr. Michel Campillo
Observatorie de Grenoble
I.R.I.G.M.-B.P. 53
38041 Grenoble, FRANCE

Dr. Lawrence A. Drake
Observatorio San Calixto
Casilla 12656, La Paz, BOLIVIA

European-Mediterranean Seismological Centre
CSEM
c/o LPG
BP 12, 91680 Bruyeres-le-Chatel
FRANCE

Dr. Peter Firbas
Institute of Physics of the Earth
Masaryk University Brno
Jecna 29a
612 46 Brno, CZECH REPUBLIC

Prof. Hans-Peter Harjes
Institute for Geophysik
Ruhr University/Bochum
P.O. Box 102148
463 Bochum 1, GERMANY

Dr. Manfred Henger
Fed. Inst. for Geosci. & Nat'l Res.
Postfach 510153
D-3000 Hanover 51, GERMANY

Dr. Eystein Husebye
Inst. for Solid Earth Physics
University of Bergen
Allegation 40
N-5007 Bergen, NORWAY

David Jepsen
Nuclear Monitoring Section
Geology & Geophysics
Bureau of Mineral Resources
G.P.O. Box 378
Canberra, AUSTRALIA

Ms. Eva Jöhannisson
Senior Research Officer
National Defense Research Institute
P.O. Box 27322
S-102 54 Stockholm, SWEDEN

Prof. Brian L.N. Kennett
Research School of Earth Sciences
Institute of Advanced Studies
G.P.O. Box 4
Canberra 2601, AUSTRALIA

Dr. Peter Marshall
Dr. Alan Douglas
Ministry of Defense/Procurement Executive
Blacknest, Brimpton
Reading FG7-4RS
ENGLAND (2 copies)

Dr. Bernard Massinon
Dr. Pierre Mecheler
Societe Radiomana
27 rue Claude Bernard
75005 Paris, FRANCE (2 copies)

Prof. Keith Priestley
Dept. of Earth Sciences
Madingley Rise, Madingley Road
University of Cambridge
Cambridge CB3 0EZ, ENGLAND

Dr. Frode Ringdal
Dr. Svein Mykkeltveit
NTNF/NORSAR
P.O. Box 5I
N-2007 Kjeller, NORWAY (2 copies)

Dr. Jorg Schlittenhardt
Federal Inst. for Geosciences &
Natural Resources
Stilleweg 2, D-3000 Hannover 51
GERMANY

Dr. A. Shapira
Seismology Division
Inst. for Petroleum Research & Geophysics
Holon, ISRAEL

Dr. C. Srinivasan
Seismology Section
National Inst. of Rock Mechanics
New Delhi, INDIA

Dr. Tuncay Taymaz
Istanbul Technical University
Dept. of Geophysical Engineering
Maslak-80626, Istanbul, TURKEY